Studies of the Structure and Activity History of Quasars Probed by Luminosity Variation

Shumpei Nagoshi

A thesis presented for the degree of Doctor of Science

Department of Astronomy,

Kyoto University, Japan

December 2022

Dissertation Advisor: Fumihide Iwamuro Shumpei Nagoshi

Studies of the Structure and Activity History of Quasars Probed by Luminosity Variation

Abstract

This thesis focuses on the luminosity variations of quasars to investigate the characteristics of their luminosity variations and central core structure. Recently, the accumulation of observational data has made it possible to observe quasar luminosity changes over long timescales of several tens of years. As a result, a number of quasars have been discovered that show 1-2 magnitude variations in optical luminosity over several years. These quasars are called Changing-State Quasars (CSQs) or Changing-Look Quasars. One characteristic of CSQs is their drastic variation in the shape of their broad emission lines. The author focused on the variation process of CSQs as the best way to study the central structure, including the broad line region (BLR). This paper presents three research results focusing on CSQs: the first is a search for new CSQs, the second is a statistical investigation of luminosity variations, and the third is a reverberation mapping of CSQs.

In the first study (Chapter 2), we report the discovery of a quasar, SDSS J125809.31+351943.0 (J1258), which brightened in optical for 4 mag from 1983 to 2015, which is one of the largest quasar brightening events so far. The history of optical photometry data of this quasar from the Catalina Real-time Transient Survey and All Sky Automated Survey for Super Novae (ASAS-SN), mid-infrared photometry data from the WISE satellite, and the broad emission line (BEL) flux obtained by spectroscopy of Sloan Digital Sky Survey shows their significant increases between 2003 and 2015. Investigating its CFHT photometric observations in 1983 and the USNO-B catalog, which contains data in 1975 and 1969, we found that the source was 4 mag fainter before than the peak of the recent ASAS-SN photometry. From the history of these data, we identified J1258 as a new CSQ. We also performed follow-up spectroscopic observations in December 2018 and May 2019, using the 2-meter telescope in Nishi-Harima Astronomical Observatory. The results show that the continuum flux and the BEL flux decreased to about 50 % of its peak. This indicates that J1258 is causing two changing-states for the BEL flux and continuum flux. We argue that J1258's variability, in particular its brightening event, can be explained by the propagation of the heating front and the accretion disk state transitions based on the timescale and Eddington ratio variations. The

estimated mass of the black hole of J1258 is about an order of magnitude larger than the CSQs found so far. Since both the changing timescale and the size of the accretion disk depend on the black hole mass, the J1258 brightening event can be interpreted as a scaled version of the variability in other CSQs. This suggests that samples of distant quasars with larger black hole masses may contain objects with longer and more severer variations.

In the second study (Chapter 3), we found a relationship between quasar luminosity variations and spectral features. It is known that quasar's FeII/Hβ flux ratio and equivalent width of [OIII]5007 are negatively correlated, called Eigenvector 1. We visualized the relationship between the position on this Eigenvector 1 (EV1) plane and how they had changed their brightness after ~ 10 years. We conducted three analyses using different quasar samples each. The first analysis showed the relation between their distributions on the EV1 plane and how much they had changed brightness, using 13,438 Sloan Digital Sky Survey quasars. This result shows how brightness changes later are clearly related to the position on the EV1 plane. In the second analysis, we plotted the sources reported as CSQs on the EV1 plane. This result shows that the position on the EV1 plane corresponds activity level of each source, the bright or dim state of them are distributed on the opposite sides divided by the typical quasar distribution. In the third analysis, we examined the transition vectors on the EV1 plane using sources with multiple-epoch spectra. This result shows that the brightening and dimming sources move on the similar path and they turn into the position corresponding to the opposite activity level. We also found this trend is opposite to the empirical rule that $R_{\rm FeII}$ positively correlated with the Eddington ratio, which has been proposed based on the trends of a large number of quasars. From all these analyses, it is indicated that quasars tend to oscillate between both sides of the distribution ridge on the EV1 plane, each of them corresponding to a dim state and a bright state. This trend in optical variation suggests that significant brightness changes, such as Changing-Look quasars, are expected to repeat.

In the third study (Chapter 4), we performed reverberation mapping to J1258 with optical spectroscopy to investigate the structure of the broad line region and to measure the black hole mass. We also measured the time-lag between the WISE light curve and the optical light curve to estimate the size of the dust torus. In addition, we compared optical to X-ray spectral indices ($\alpha_{\rm ox}$) before and after the state transition to investigate the structure difference of the accretion disk. The results of the reverberation mapping show that the Eddington ratio crossed the value of 0.01 before and after state transition for the black hole mass of $10^{9.46^{+0.15}_{-0.19}}{\rm M}_{\odot}$. The variations in $\alpha_{\rm ox}$ and the Eddington ratio were consistent with those predicted

from the instability of the accretion disk caused by hydrogen ionization. From the viewpoint of the broad line region, we confirmed the existence of two distinct rotating/inflowing components located near the dust torus. After we discuss the origin of these line-emitting regions, we suggest that these components originate from rotating/inflowing gases located near the dust torus generated by different processes.

Acknowledgments

First of all, I would like to begin by expressing my sincere gratitude to my supervisor, Dr. Fumihide Iwamuro. He has provided me with valuable insights into my research since I was an undergraduate. I would also like to thank Prof. Shin Mineshige and Dr. Yoshihiro Ueda for their support, including helpful discussions about my research, which made my time as a doctoral student very meaningful. I am grateful for the numerous learning opportunities they have provided me. It is an honor to express my deep appreciation to them.

During my time in the Department of Astrophysics, I have had the opportunity to spend quality time with many people outside of research. Dr. Tomoyasu Hayakawa, Dr. Atsushi Tanimoto, Dr. Kyuseok Oh, Dr. Fumiya Maeda, Dr. Satoshi Yamada, and other senior members have taught me many things, from research discussions to problem-solving in my personal life. Mr. Ryosuke Uematsu, Mr. Naoya Atsumi, Ms. Haruhi Shirato, and Mr. Kaname Taniyasu, who are my roommates, have made my daily life more fulfilling. My colleagues in the same grade, Mr. Shoji Ogawa, Mr. Kosuke Kihara, Mr. Yuji Kotani, Mr. Kenta Taguchi, Mr. Ryo Tsukui, Mr. Yuh Tsuneto, Mr. Qiliang Fang, Mr. Tomoki Matsuoka, and Mr. Daiki Yamasaki, have stimulated me as a researcher and we have also had a good time as friends.

Prof. Jian-Min Wang and Dr. Pu Du taught me a great deal about reverberation mapping, which contributed significantly to the results at the core of my doctoral thesis. I have also had many enlightening discussions with members of their research group, who have had a very strong and positive influence on my research approach.

I was fortunate to receive funding from the Japan Society for the Promotion of Science fellowship JP22J13428 and a research assistantship from the Space Unit at Kyoto University. I am grateful for this support, which allowed me to focus on my research without worrying about finances.

Finally, I would like to take this opportunity to express my sincere gratitude to my family and friends for their emotional support during my doctoral studies.

Contents

Chapter 1

Introduction

1.1 General understanding of the structure of quasars

Supermassive black holes (SMBH) are known to be universally distributed among the center of the galaxies, whose masses are greater than $10^6 M_\odot$. One of the major questions in astronomy is how SMBHs were formed in the context of the history of the universe.

Some SMBHs have accretion disks as an engine to convert gravitational energy into radiation, which is observed as objects called active galactic nuclei (AGN). In particular, the relatively bright AGNs are called quasars. Quasars are commonly classified into two types, Type 1 and Type 2, based on their optical spectra: Type 1 quasars have broad emission lines with velocities of $\sim$ 1000 km/s, while Type 2 quasars only have narrow emission lines with velocities of $\sim$ 100 km/s. This difference in the optical spectra is widely interpreted using the picture of the AGN unified model (Figure 1.1: Antonucci (1993); Urry & Padovani (1995)). According to the unified model, an accretion disk is formed around the SMBH ($<\sim$ 1000 R_g). The broad line region, the emitter of the broad emission line, is distributed around it ($\sim$ 0.1 pc). The accretion disk is surrounded by a torus-like shield ($>\sim$ 1 pc). Considering such a picture, the difference in quasar spectra can be represented by only one parameter, the viewing angle. The unified model is widely accepted as a general picture.

While the unified model is generally accepted, there are many unresolved issues regarding the detailed structure and velocity information. For example, where the

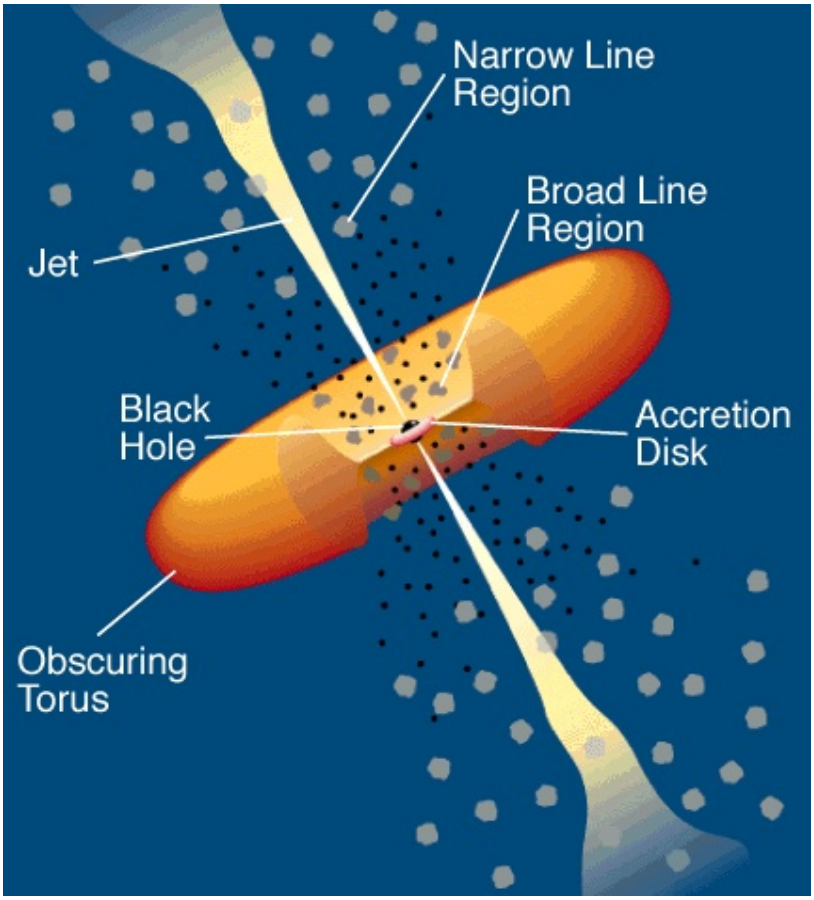

Figure 1.1: The unified model of AGN (Antonucci 1993; Urry & Padovani 1995).

gas in the BLR came from, how the dust torus and accretion disk are connected, and so on. To answer such questions, there is a growing need to update the unified model.

Understanding the AGN structure including broad line region (BLR) will help solve several significant problems in astronomy. First, knowing the mechanism of gaining mass will lead to understanding the formation process of supermassive black holes and the co-evolution with the host galaxy (Magorrian et al. 1998). The information on the structure and kinematics of the BLR is essential to investigate the black hole evolution because the black hole mass is estimated from the kinematics of the BLR. Secondly, the precise picture of quasars is also valuable for measuring the distances from our galaxy. A controversial issue in observational cosmology is the Hubble tension problem (see Perivolaropoulos & Skara 2022, as a recent review) , where the measured Hubble constant (H_0) with cosmic microwave background (Planck Collaboration et al. 2020) and with the distance ladder (e.g., Riess et al.

2022) differ by more than 5σ. In this context, distance measurements using the BLR of quasars (e.g., Wang et al. 2020) are expected to be a clue to solving the problem, as they can estimate H_0 independently of conventional methods. Thus, the main purpose of this study is to investigate the structure and kinematics of BLR.

1.2 Reverberation Mapping

Broad lines are major characteristics of Type 1 quasars. The detailed structures, however, are still under discussion as well as the motion and origin of the BLR. (see Gaskell 2009, as a review)

Reverberation mapping (RM) is one of the most promising methods for studying the quasar structure (see Cackett et al. 2021, and references therein). Quasars randomly change luminosity at all wavelengths in various scales. Using that feature, RM is a method to estimate the size of the BLR by measuring the response time between the variation in the continuum emitted from the accretion disk and the variation in the broad emission line emitted from the BLR. The black hole mass can be calculated by the measured size of the BLR and its velocity, which is thought to be the most precise method for measuring black hole mass of distant quasar. An important results of the RM is the discovery of a strong correlation between luminosity and the BLR radius (L-R relation), which has been widely used to estimate black hole mass from a single spectrum. RM can provide more detailed information by increasing the velocity resolution and observation frequency. As usual, emission lines are often divided into several velocity components to estimate the qualitative structure and kinematic information of the BLR (velocity-resolved RM). By using the information derived from each component, it will be possible to elucidate the structure and kinematics of the BLR. If the red wing of the broad line lags behind the blue on, for example, we can infer that outflow motion is dominant in the BLR (Figure 1.2). Thus, in this study, we adopted RM to investigate the properties of the BLR.

Understanding the properties of the BLR is essential to accurately estimate the black hole mass, which is a fundamental physical quantity of quasar. The biggest reason for the necessity is that the measurement of black hole masses by RM is subject to the uncertainty of the structure, mainly the viewing angle, of the BLR. In RM, the black hole mass is calculated with the following equation;

$$M_{\rm BH} = f\frac{c\tau\Delta V^2}{G}, \tag{1.1}$$

where c is the speed of light and G is the gravitational constant. The f is a factor

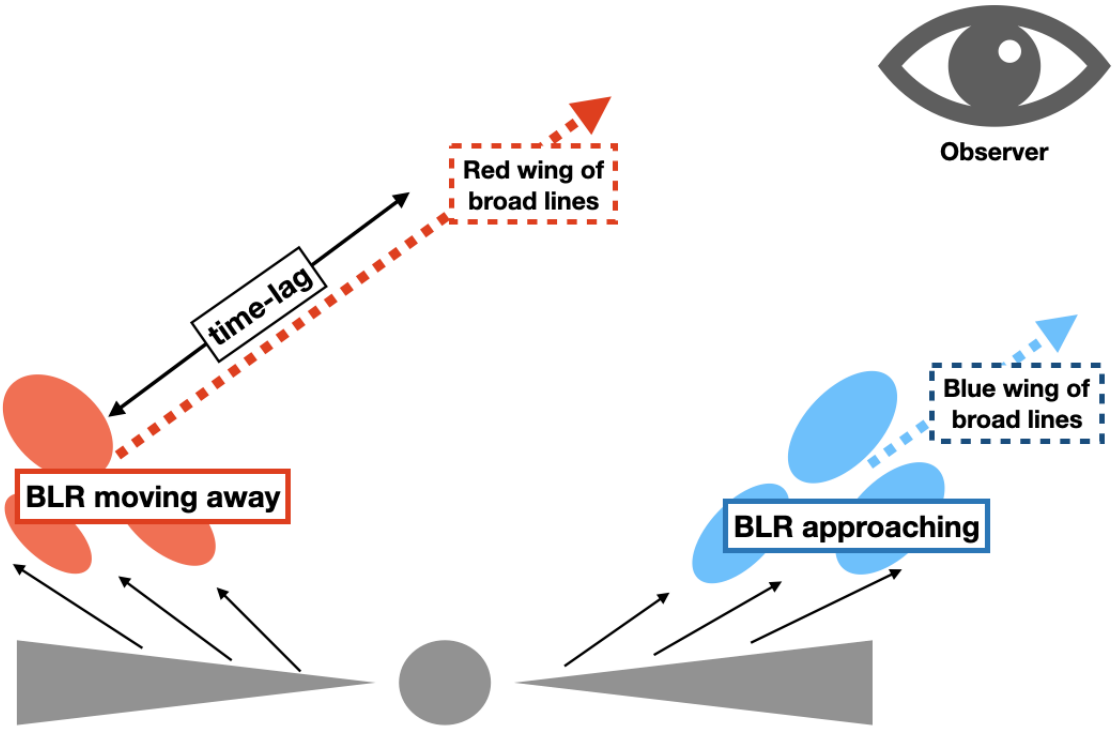

Figure 1.2: A conceptual picture of an example of how radial motion is detected by velocity-resolved reverberation mapping. If BLR has a significant radial motion outward, it is expected that the variation of the red wings of the broad lines will follow the variation of the blue wings.

that reflect the structure, kinematics, and inclination of the BLR. The problem is that the f factor is supposed to take different values for each object, because at least inclination is different from object to object, but is currently fixed to a constant value. Furthermore, in many cases, the radius of the BLR is estimated from a single spectroscopic observation by assuming the L-R relation. However, it is considered that the assumption of an L-R relation is still incomplete because some observations suggest that the L-R relation does not hold for populations with high Eddington ratios (Du et al. 2018b; Li et al. 2021). To solve these problems, it is necessary to create models that are closer to reality and check them against observations, but there are many observational uncertainties. Therefore, gaining insight into the structure of the BLR is important in astronomy.

1.3 Changing-State Quasar

The author believes that Changing-State Quasars (CSQs; or Changing-Look Quasars[1]) are important for understanding the BLR. CSQs are quasars that show large variations in optical to mid-infrared brightness and broad line fluxes (Fig 1.3; see Ricci & Trakhtenbrot (2022) as a review and references therein). Because the broad lines show extreme variability, it can be expected that the observation of the broad line emergence process will help us gain insight into the origin of the BLR.

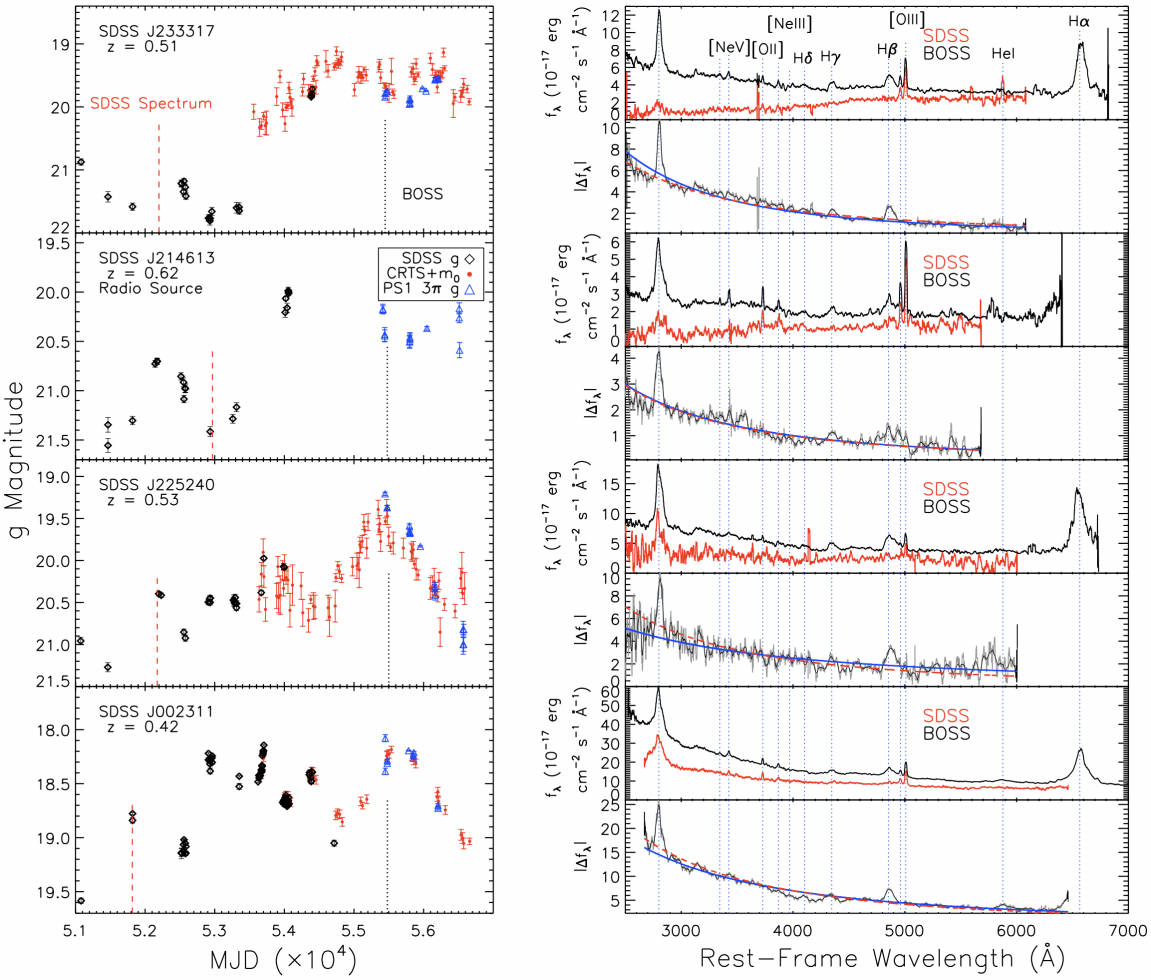

Figure 1.3: Example of g-band light curves (left panel) and optical spectra (right panel) of CSQs in MacLeod et al. (2016).

[1]Strictly speaking, the definitions of Changing-Look Quasar and Changing-State Quasar are different, but are treated context in this paper similarly.

1.4 Problem Setting and Strategy

The large-scale variability of BLR in CSQ is one of the best experimental environments to understand the origin of BLR. To understand the nature of BLR, RM is the most effective research method. Therefore, the purpose of this study was set as to obtain new insight into the origin of BLR by applying RM to CSQ.

A few years ago when the author started the research, however, several challenges remained as follows.

- The number of reported CSQs is not large, making it difficult to find optimal sources to monitor.
- Previously reported Changing-State Quasars (CSQs) have generally been difficult to follow up with spectroscopic observations because they were mostly serendipitously observed at multiple epochs through spectroscopy, making them tend to be too dim.
- Since it is unclear whether the brightness variations of CSQs are expected to repeat or not, it is not certain that we can observe the Changing-Look process even by the spectroscopic monitoring of the known CSQ sources.

The author first addressed these issues and then conducted the RM of the CSQs. In the first study (Chapter 2), the author identified the best source for observation: an object that has shown more extreme variations than any previously reported CSQs, which is expected to have higher signal-to-noise ratios of the variable component than other objects. Then, in the second study (Chapter 3), the author examined whether CSQs are a repeating phenomenon in general by analyzing the spectra of several thousand objects. The results suggest that CSQs are likely to repeat like oscillations. Finally, in the third study (Chapter 4), we conducted spectroscopic monitoring of the target found in the first study."

This thesis presents the research that the author conducted during the doctoral program. Chapters 2, 3, and 4 consist of research that has been (or is expected to be) published as independent peer-reviewed papers. In Chapter 5, the summary of the results of each research and future prospects are described.

Chapter 2

Discovery of a new extreme changing-state quasar with 4 mag variation, SDSS J125809.31+351943.0

This thesis chapter originally appeared in the literature as
Shumpei Nagoshi, Fumihide Iwamuro, Kazuma Wada, and Tomoki Saito, *Publications of the Astronomical Society of Japan, Volume 73, Issue 1, pp.122-131*

2.1 Introduction to Chapter 2

The luminosity of quasars in various wavelengths varies at various timescales. The typical scale of the variation in optical was thought a factor of 0.1 mag on a timescale of a few days to months (e.g., MacLeod et al. (2010)). The variation of the luminosity is usually interpreted as a result of local changes in the accretion disk, as phenomenologically explained in models, *e.g.*, the damped random walk (MacLeod et al. (2010)). However, actual observations frequently show results that are inconsistent with popular theories or empirical rules. For example, the standard disk model predicts much longer viscous timescales than actually observed ones of variation. More puzzlingly, several recent large-scale optical surveys have shown that about half of the quasars exhibit more than 1 mag of optical variability that cannot be explained by conventional models (Rumbaugh et al. (2018)). The recent Sloan

Digital Sky Survey (SDSS) provides a massive data set of multiple spectroscopic observations for millions of sources spanning $\sim$ 10 years. An interesting outcome from the survey is that some distant quasars show a so-called optical "changing-look" phenomenon (LaMassa et al. (2015), MacLeod et al. (2016), MacLeod et al. (2019), Ruan et al. (2016), Gezari et al. (2017), Wang et al. (2018), Stern et al. (2018), Trakhtenbrot et al. (2019), Sheng et al. (2020), Guo et al. (2020)) whereby broad emission lines (BELs) appear or disappear, which had been previously observed only in the Seyfert galaxies (Tohline & Osterbrock (1976), Cohen et al. (1986), Clavel et al. (1989), Storchi-Bergmann et al. (1995)). Most of the quasars that show a "changing-look" phenomenon, or Changing-Look Quasars (CLQ), show a common characteristic: large optical luminosity variations exceeding 1 mag. In recent years, such large luminosity changes have been found in many other objects besides CLQs, such as Hyper Variable Quasars (Rumbaugh et al. (2018)) and Changing-State Quasars (CSQs; Graham et al. (2020)). The classification of the CLQ is based on the change of BELs, that of the HVQ is on the change of optical brightness, and that of the CSQ is on the change of BELs, optical continuum flux density, and mid-infrared luminosities. In this paper, we will refer to them collectively as CSQs. Objects that satisfy the CSQ classification criteria likely to satisfy the other two classification criteria as well.

Two classes of the origin are widely accepted as candidates to explain this type of variability: temporary shielding of the central region by optically thick material (Elitzur (2012)) and rapid changes in the mass accretion rate of the central engine (eg. Dexter et al. (2019), Ruan et al. (2016)). Other factors such as micro-lensing (Bruce et al. (2017)) and tidal disruption events (Merloni et al. (2015)) have also been proposed. In many cases in reality, change in mass accretion rate is believed to be the dominant cause on the basis of observation in X-ray (Husemann et al. (2016)) and in optical polarization (Hutsemékers et al. (2017)). A main question is the origin and mechanism of such a significant change in the mass accretion rate and extreme change in the broad-line intensity that often accompanies the former.

Reverberation mapping is an effective way to investigate what is happening in the central region of the CSQ because it can estimate the structure (Pancoast et al. (2014)) of the broad line region (BLR) and determine the accurate black hole mass (Peterson et al. (2004)). Reverberation mapping usually requires frequent spectroscopic observations in every $\sim$10 days for a few years. Therefore, we explored a highly variable (more than 1 mag in optical) and relatively bright (less than 17 mag in optical) CSQ that would be feasible for reverberation mapping.

This paper describes the discovery of SDSS J125809.31+351943.0 (J1258) and discusses its large amplitude of variability. The method we used to find J1258

is described in Section 2.2. From Section 2.3, we focus on J1258. The data and observations that we used are explained in Section 2.3. Section 2.4 describes the analysis with which we find the object to show a variation in the optical and mid-infrared flux and identify it as a CSQ. Section 2.5 discusses the causes and timescales of the variation for 4 mag. The cosmological parameters are assumed to be $H_0 = 70$ kms^{-1}Mpc^{-1}, $\Omega_{\rm M} = 0.3$ and $\Omega_{\Delta} = 0.7$ based on the ΛCDM cosmology throughout this paper.

2.2 Sample selection

We performed a search for highly variable quasars, using the Catalina Real-time Transient Survey (CRTS) light curves in V band and Sloan Digital Sky Survey (SDSS) quasar catalogue data release 7 (SDSS DR7Q; Schneider et al. (2010)). The catalogue contains 105,783 quasars, and 19,547 of them are located in redshift of less than 0.8. We obtained CRTS light curves for 16,890 quasars among them to analyze their variation amplitudes and timescles.

2.2.1 CRTS light curve

The archival data for the CRTS (Drake et al. (2009)) consists of long-term ∼10 years) photometric observations obtained with three telescopes: the 0.7-m Cataline Sky Survey Schmidt (CSS) telescope, the 1.5-m Mount Lemmon Survey (MLS) telescope in Arizona, and the 0.5-m Siding Springs Survey (SSS) telescope in Australia. The survey observes an area of 2.5×10^3 deg^2 per night, with four 10-minute exposures per field of view. In addition, 21 observations were made for each lunar period on average. The observations were unfiltered and the measured flux values were converted into the Johnson V-band mag, with data for approximately 400 million objects at magnitude V $\sim$ 20 and above and Dec > -30 deg for the period 2003 to 2016 (CSS and MLS). In addition, the SSS provides data for the southern sky from 2005 to 2013 for about 100 million objects at magnitude V $\sim$ 19 and above.

2.2.2 Light curve analysis

Most quasars have random variations on short timescales, but CSQs tend to have monotonic variations on long timescales of a few years (e.g, Graham et al. (2020)). In order to find such monotonically variable objects, a linear function was used to

fit the light curves using the least squares method. We used only the values in the MJD range from 54101 to 57506, because photometry before MJD 54101 can lead to incorrect values due to inappropriate aperture size (Drake et al. (2019)). Values outside the 3σ (σ is the standard deviation of the fitting) were excluded as outliers and re-fitted (3σ clipping). This process was repeated until no outliers were found. An example of the fitting is shown in figure 2.1. Such fittings were performed for all the light curves and narrowed down to 3,792 objects that included a duration of more than 1000 days and had an average CRTS's V-band magnitude brighter than 18. To find bright and variable objects for the following spectroscopic observation, we focused on those with slope of less than -0.1 mag/year of the fitted line and small σ of the fitting. The distribution of the slope and σ obtained by the fitting is shown in figure 2.2. The distribution of the slope and the optical magnitude differences between the first and last measurements (Δ) is shown in figure 2.3. In these diagrams, it can be seen that the variation of J1258 (the redshift is 0.31) is extremely larger than that of the other quasars.

This method is similar to that used by Graham et al. (2020) (the primary difference is that they used Bayesian blocks to analyze light curves), but J1258 was not on their list. A comparison of our selection approach with that used in Graham et al. (2020) is discussed in section 2.5.6. From next section, we focus on J1258.

2.3 Data and Observation

2.3.1 Photometric data

ASAS-SN

To investigate J1258's recent variability, we used the photometric data from the All Sky Automated Survey for Super Novae (ASAS-SN; Kochanek et al. (2017)), a project to automatically perform an all-sky survey, using 24 telescopes every observable day. The limiting magnitude of the ASAS-SN is about 17 mag. In the ASAS-SN, two filters, g-band and V-band, were used. We used the data of either filter for our analysis partly because the CRTS observations were made with no filters and majorly because a small difference between the data with the two filters is negligible compared with the variation of the target objects. There is a systematic discrepancy between the CRTS and ASAS-SN photometric systems. We corrected the filterless CRTS flux, using the ASAS-SN photometric data from the period when both observations were made, in the following procedure. First, for each CRTS

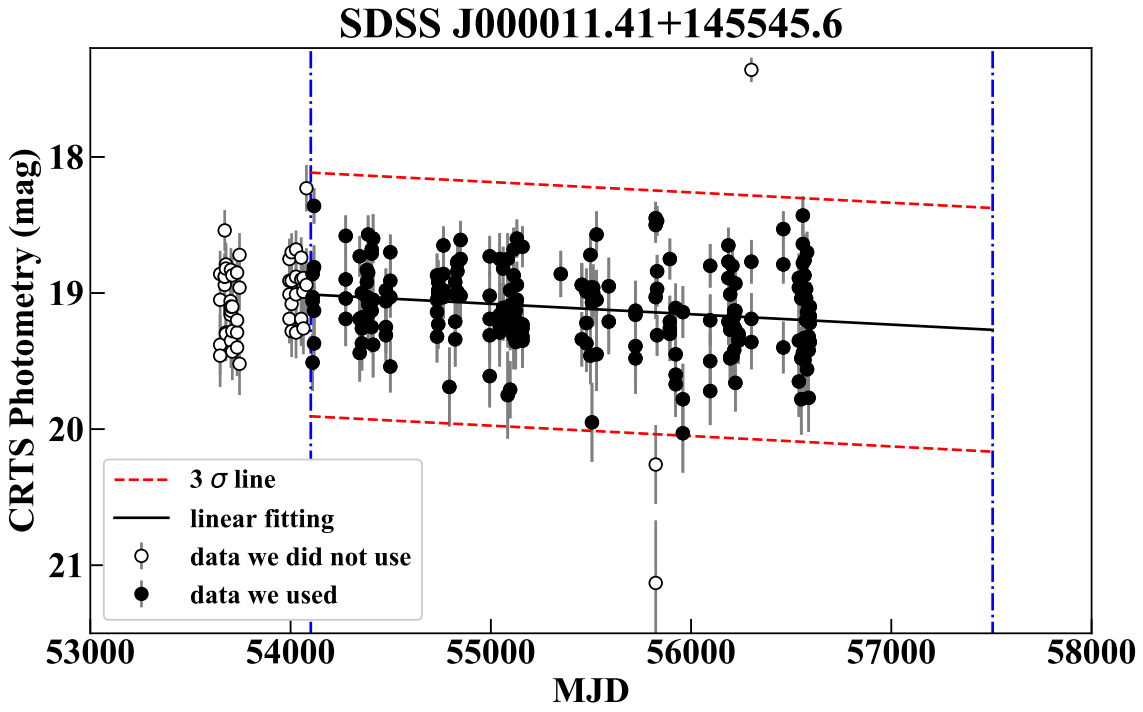

Figure 2.1: An example of fitting a CRTS light curve. The black and white points represent the original catalog data. The blue dashed line represents the MJD 54101 and MJD 57506, and only the data between these line are
used. The solid black line is a fitting straight line and the dashed red line represents 3 σ.

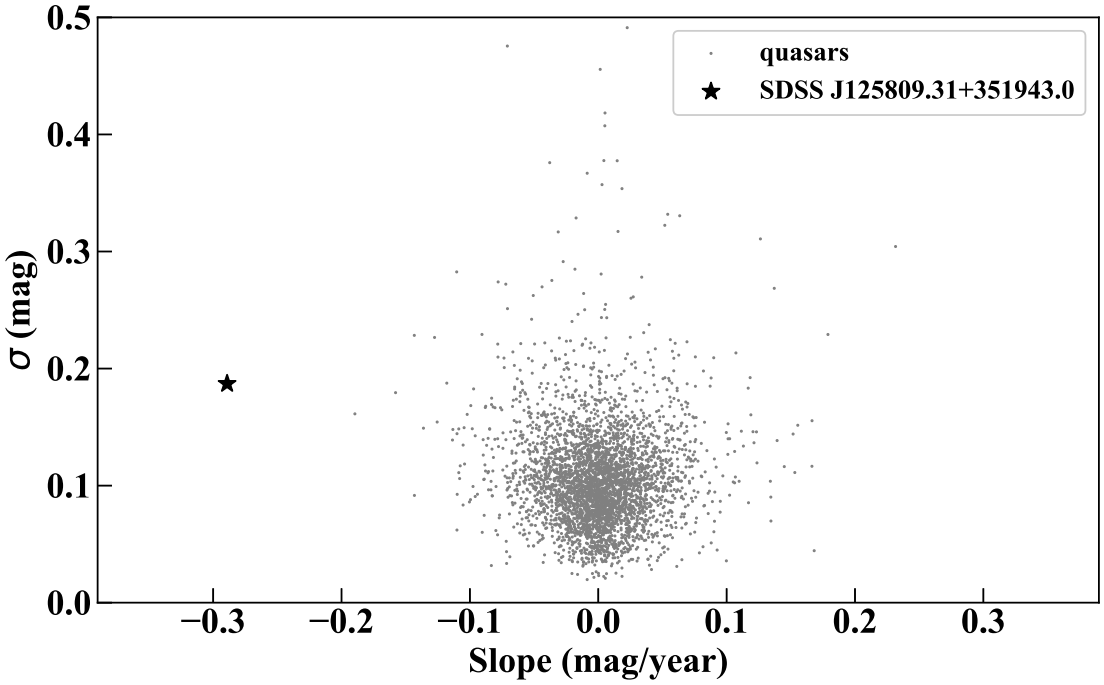

Figure 2.2: A diagram summarizing the slope and σ obtained from the fitting. The gray points represent the results of each fitting, and the star-shaped point represents SDSS 125809.31+351943.0.

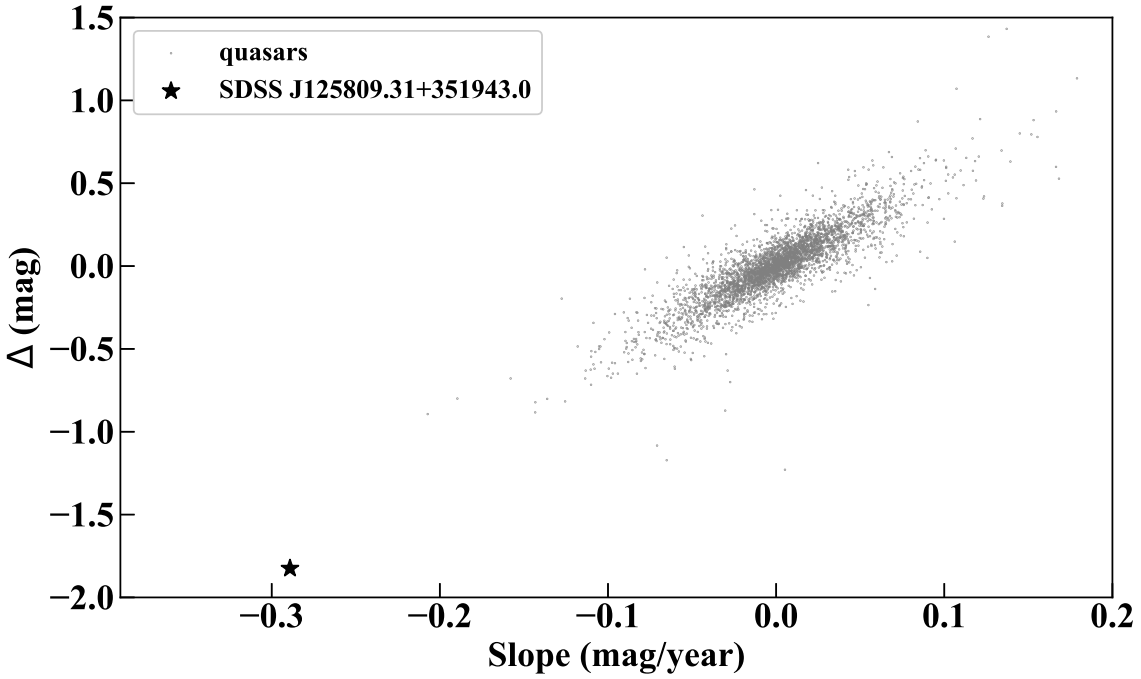

Figure 2.3: A diagram summarizing the slope and Δ obtained from the fitting. The y-axis represents the amount of increment in the CRTS light curve from the first magnitude (the average of values measured within 100 days of the beginning of the light curve) to the last magnitude (the average of values measured within 100 days of the end of the light curve)). The gray points represent the result of each fitting, and the star-shaped point corresponds to SDSS 125809.31+351943.0.

photometric value, we calculated the average ASAS-SN photometric value within 20 days of the epoch when the CRTS data was taken. Next, we calculated the ratio of the CRTS photometric value to the average ASAS-SN value. Finally, we determined the offset by averaging the calculated ratios; the ASAS-SN flux is 0.87 times as bright as the CRTS flux (figure 2.4).

Then, outliers were removed from the ASAS-SN data, using linear fitting with a 3σ clipping iteration, applied to the year-by-year data separately. Figure 2.6 shows the light-curves of the cataloged data before and after the correction.

WISE

The Wide-field Infrared Survey Explorer (WISE; Wright et al. (2010)), which is a mid-infrared satellite launched in December 2009 and observed the entire sky in four bands (3.4, 4.6, 12, and 22 μm), also observed J1258. WISE operations were temporarily terminated in February 2011, but observations resumed in December 2013 as the NEOWISE project(Mainzer et al. (2014)). NEOWISE has two bands of 3.4 and 4.6 μm and observed the entire sky, visiting each area in the sky about ten times every six months.

As the information of J1258, we referred to the single-exposure profile-fit magnitude within 3" from RA = 12:58:09.31 and DEC = +35:19:43.03. From these values, we selected those with no contamination and confusion flag ("cc_flags" = 0000). In the present analysis, we used the combined data with each bin accumulated for six months period, sufficient for the variation timescale of our interest.

Before CRTS: USNO and CFHT

We also investigated photometric observations of SDSS J125809.31+351943 before the era of the CRTS. We obtained archival data of photometric observations by the Canada-France-Hawaii Telescope (CFHT) in 1983 and by the United States Naval Observatory (USNO) in 1975 and 1969. No errors for the data are listed in the catalogs; however, given that their photometric observations were carried out with photographic plates, the errors are expected to be considerable. We estimated the systematic and measurement errors of the CFHT and USNO data, comparing their data of 189 AGNs reported in Weedman (1985), which is a reference for the photometry in CFHT, with those of the g-band data in the SDSS DR12 Photometry Catalog (Alam et al. (2015)). Here, the comparison was made only with the quasars included in the SDSS DR12 quasar catalog to avoid mismatches with nearby stars.

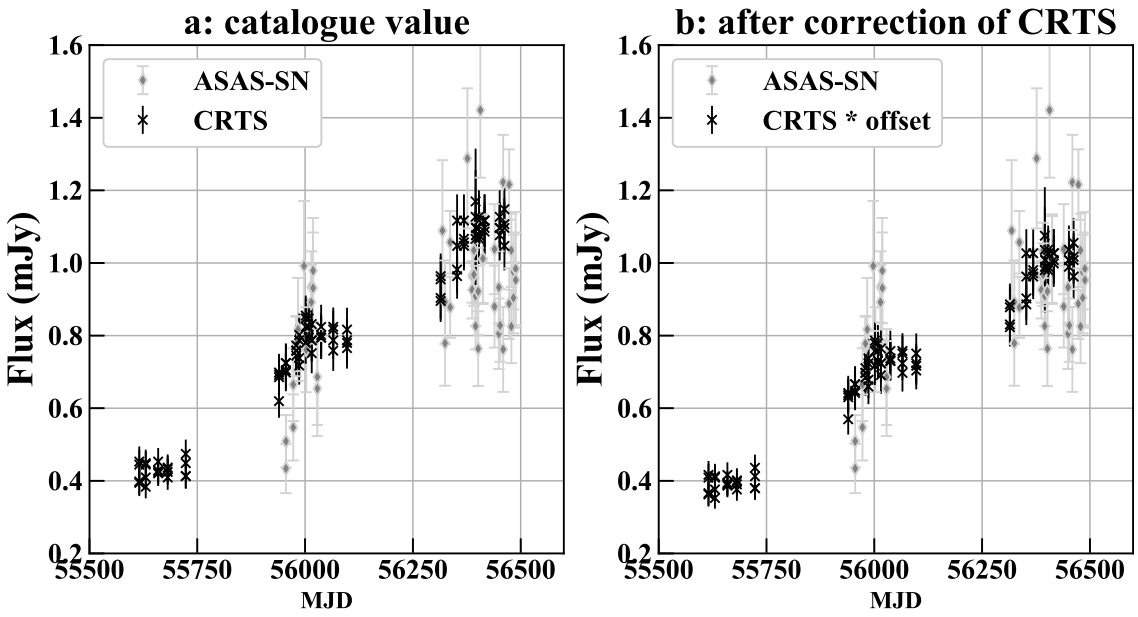

Figure 2.4: (Left panel: a) cataloged (crosses) CRTS and (diamonds) ASAS-SN fluxes (mJy) for regions encompassing J1258 where both the observations were available. (Right panel: b) Same as panel b but with the CRTS fluxes replaced with the corrected ones.

Figure 2.5 compares the photometric values of the SDSS g-band with those of the CFHT, using 65 matched sources. We found a systematic offset of minus 0.686 mag with a typical error of 0.776 mag in the CFHT photometric observations. The same analysis was performed with regard to the USNO-B catalog values (figure 2.5), where the B-band of USNO is equivalent to the g-band of the SDSS.

Figure 2.6 summarizes all the photometric data of J1258 accompanied with the estimated errors, where the offsets are corrected. The result indicates that the luminosity of the object varied by 4 mag during 1983 to 2016. We should note that this object is radio quiet and hence that the jet contribution to this variability should be insignificant.

2.3.2 Spectroscopic data and observation

J1258 has been spectroscopically observed by the SDSS twice so far, in April 2006 (referred to as the first) and April 2016 (second). The SDSS (York et al. (2000)) is based on a photometric survey using a 2.5-m wide-field telescope (Gunn et al. (2006)) and 30 2k × 2k CCDs and is followed by spectroscopic observations. Between the two observations, the spectroscopic instrument was upgraded, the wavelength range was extended, and the thickness of the fiber on the SDSS plate was changed from $3''$ to $2''$.

We performed two new spectroscopic follow-up observations in December 2018 and May 2019 with the slit spectrograph called "MALLS" installed on the 2-meter telescope in Nishi Harima Astronomical Observatory in Japan. The grating was 150 /mm, giving a spectral resolution of ~ 600, with the $1''.2$ slit width and GG475 order cut filter. We executed five 1200-second exposures for two nights. The observed data were reduced with the standard processing of slit spectroscopy with IRAF (dark subtraction, flat correction, matching sky subtraction, wavelength correction, and flux correction using the spectrophotometric standard).

2.4 Analysis and Identification

The definition of the CSQ by Graham et al. (2020) with regard to its physical properties is summarized as follows. 1. it is not a blazer; 2. its optical luminosity varies greatly on a longer timescale than a typical quasar (A change of more than 1 mag satisfies the conditions, although the exact criteria is different. See the original paper for detailed conditions.); 3. it has more than 0.2 mag of variation in

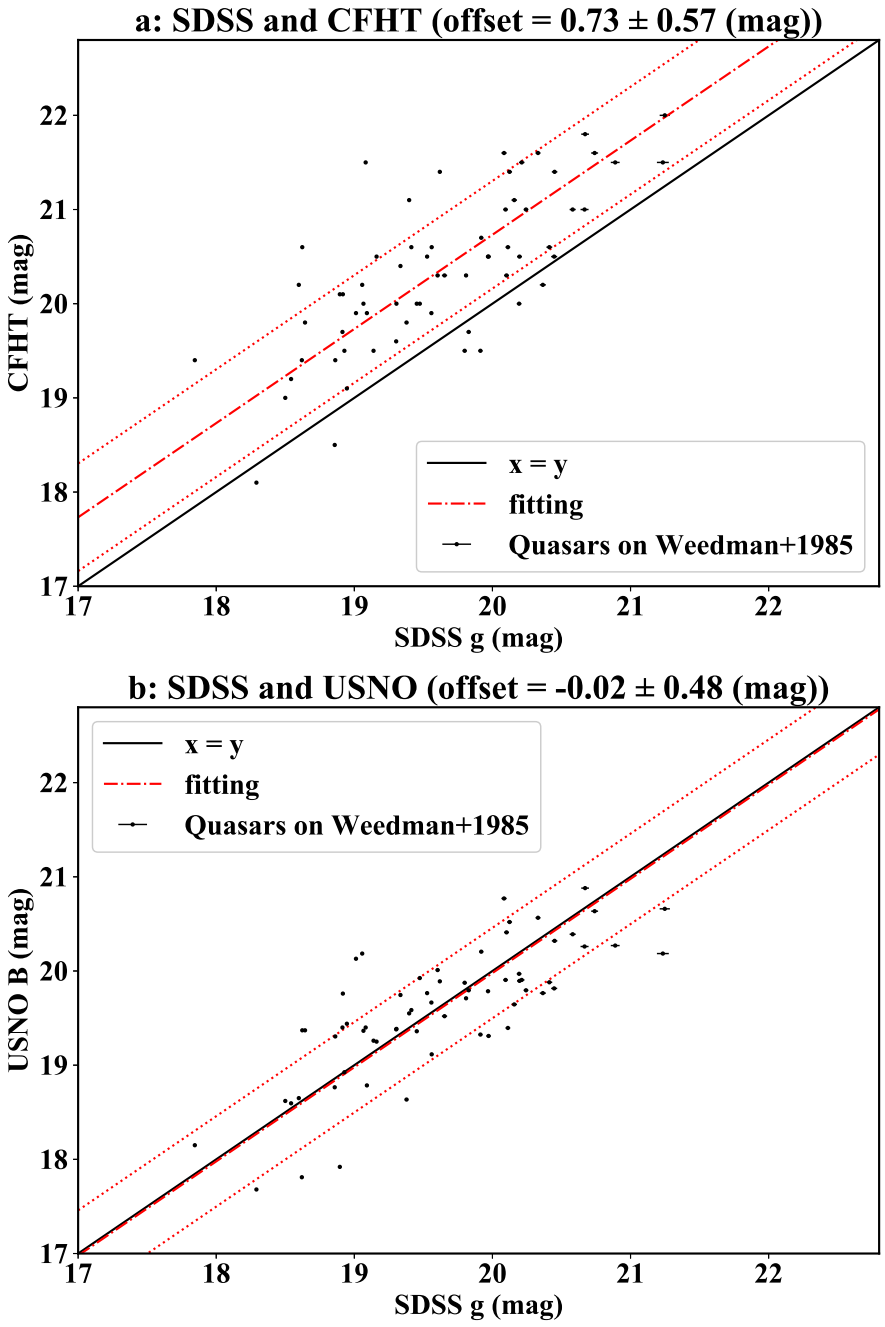

Figure 2.5: (Top panel: a) Scatter plot of the photometric values of the SDSS g-band and CFHT of quasars listed in Weedman (1985), and (bottom: b) those of the SDSS g-band and USNO-B catalog. The data points are taken from Weedman (1985), the SDSS quasar catalog, and the USNO-B catalog. Black solid lines show $y = x$, and red dashed and dotted lines show the best-fit result with a linear function ($y = x$+const) and 1-σ errors.

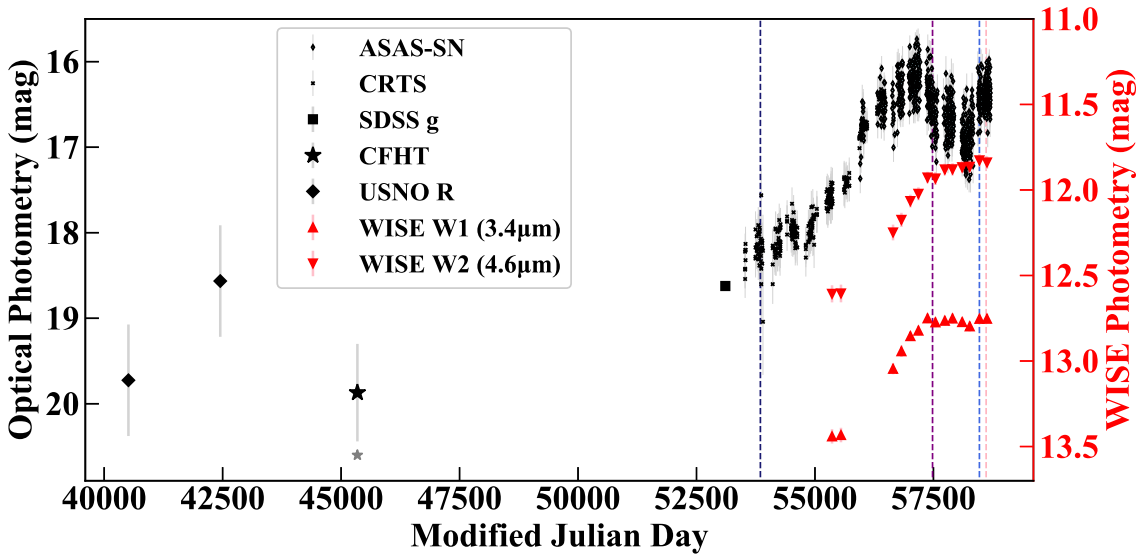

Figure 2.6: Time-series of the photometric data of J1258 in optical and mid-infrared. Red triangles denote the photometric values of WISE in the scale indicated on the right vertical axis. The other marks (black) denote the optical broad-band flux density in the scale indicated on the left vertical axis. The plotted USNO and CFHT values are already corrected as in figure 2.5. The gray star-shaped point at around MJD=45000 indicates an uncorrected value for reference. The four vertical dashed lines indicate the epochs when the spectra of the source were taken with spectroscopic observations in the colors corresponding to those in figure 2.7.

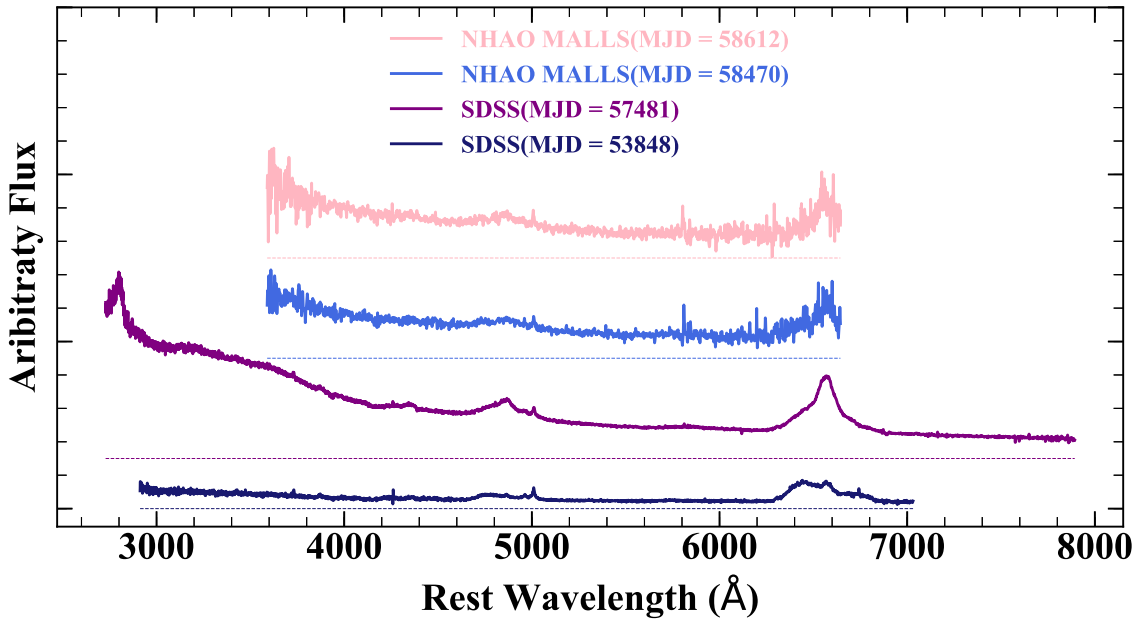

Figure 2.7: Spectra of J1258. From the bottom, the first SDSS spectrum (in dark-blue, MJD=53848), the second SDSS spectrum (purple, MJD=57481), the first MALLS spectrum (blue, MJD=58470), and the second MALLS spectrum (pink, MJD=58612). Each spectrum is normalized by the flux of [OIII]5007, and a constant is added to the flux density (y-axis) to make it easier to see. The zero point of each spectrum is drawn with a dotted line in the corresponding color.

mid-infrared flux; 4. it has been spectroscopically observed twice or more, and the time-variation of the Hβ/[OIII] ratio in its spectrum is more than 30%.

First, J1258 is not a known blazer. Also, according to the VLA/FIRST survey catalogue[1] (Becker et al. (1995)), no radio sources at 1365 or 1435 MHz were found within 30" around the coordinates of J1258 (The detection limit of the survey is about 1 mJy). Here, We estimate the upper limit of the radio (about 1.4 GHz) to optical (about 550 THz) flux ratio ($R_{\rm r-o} \equiv f_\nu({\rm radio})/f_\nu({\rm optical})$) as an indicator of its radio loudness (Kellermann et al. (1989)). J1258 at its faintest time during the VLA/FIRST observation period (1993 to 2014) was about 19 mag (about 0.1 mJy) in V-band. Then, the upper limit of $R_{\rm r-o}$ is estimated as $R_{\rm r-o} < 10$. Kellermann et al. (1989) classified samples which have R larger than 10 as radio-loud quasar. Therefor, J1258 is unlikely to be a radio-loud quasar.

Besides, the amount of the change of its optical luminosity is at least 2 mag in the last 15 years and 4 mag in a longer period. Furthermore, the W1 and W2 fluxes changed by more than 1 mag in WISE. Therefore, J1258 satisfies at least three out of the four criteria to be identified as a CSQ. The final piece of information to consolidate the identification is the ratio of Hβ/[OIII]. We measured the change in the flux of Hβ in the following procedure.

The spectrum of this object is characterized by a wide, asymmetric Hβ, which is blended with [OIII]. To estimate the Hβ flux we model-fitted the spectrum, where three Gaussians were used to approximate the broad asymmetric Hβ component, using the software "PyQSOfit" (Guo et al. (2018)). "PyQSOfit" fits the continuum component with a power-law functions and the emission lines with multiple Gaussian functions and estimates the errors of the model parameters with Markov Chain Monte Carlo simulations. Here, the galaxy components and iron lines are not taken into account because their contributions are small. In summary, the model components for the emission lines are three broad emission lines for Hβ, one narrow line for Hβ, two narrow lines for [OIII]4959/5007 (figure **??**). The parameters of the broad line component (center wavelength offset, line width, and scale factor) are allowed to vary with some fixed upper limits, whereas the center wavelength offset and line width of the narrow line component are fixed. The flux ratio between [OIII]5007 and narrow Hβ is determined from the fitting result of the SDSS spectrum with the best S/N ratio (MJD = 53848), the value of which is then assumed in the fitting of the other spectra ([OIII]5007 : Hβnarrow = 3 : 0.61). For each spectrum, the flux is normalized by the average flux of [OIII]5007.

[1] http://sundog.stsci.edu/cgi-bin/searchfirst

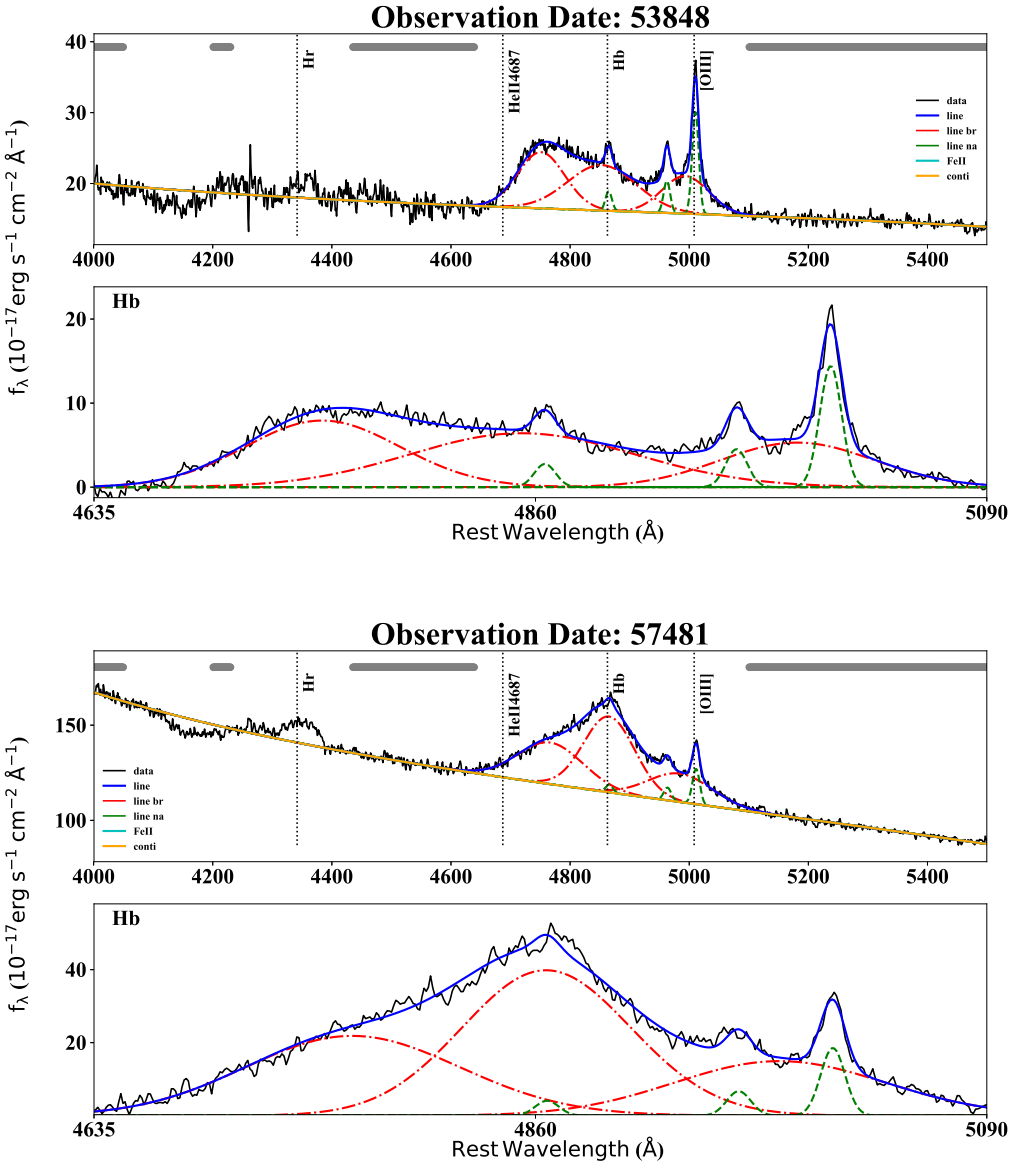

Figure 2.8: Result of the SDSS spectral fitting of the Hβ complex of SDSS J125809.31+351943.0. The upper sub-panel of each panel shows the observed spectrum with the best-fit model, including the continuum whereas the lower sub-panel shows the Hβ and [OIII] lines after the best-fit continuum component is subtracted. Gaussians with dashed and dash-dotted lines represent narrow and broad line components, respectively.

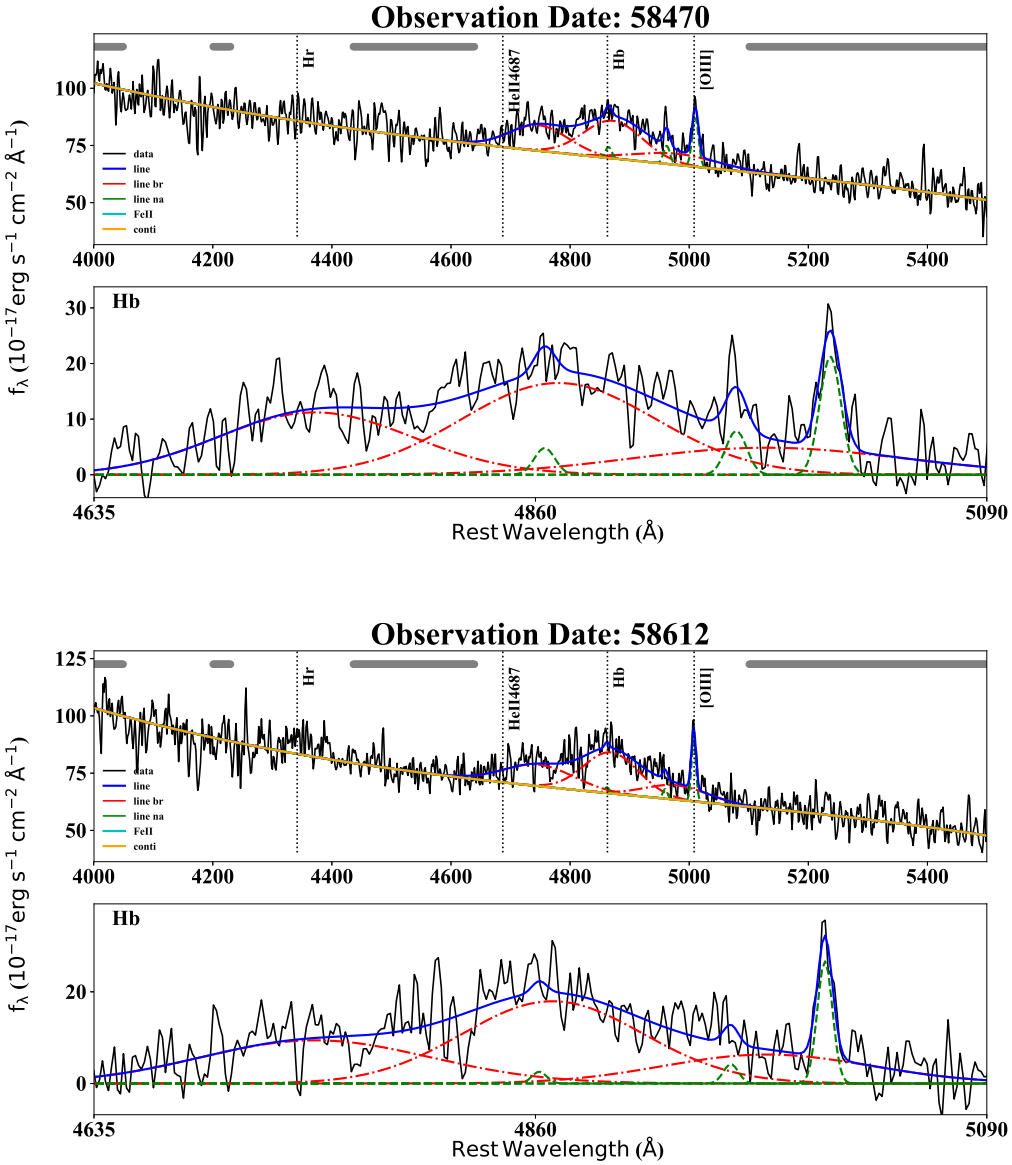

Figure 2.9: Result of the MALLS spectral fitting of the Hβ complex of SDSS J125809.31+351943.0. The upper sub-panel of each panel shows the observed spectrum with the best-fit model, including the continuum whereas the lower sub-panel shows the Hβ and [OIII] lines after the best-fit continuum component is subtracted. Gaussians with dashed and dash-dotted lines represent narrow and broad line components, respectively.

Figure 2.10 shows the time-series of the total Hβ and continuum fluxes of this source. The ratio of Hβ/[OIII] was found to have changed by 100% during the observation period. Consequently, we identify J1258 as a new CSQ. Furthermore, the time-series shows that the source experienced two changing-states for the flux of Hβ and continuum flux density. We will discuss the variance of Hβ shape in a forthcoming paper on the basis of the on-going reverberation mapping of this object.

2.5 Discussion

J1258 shows a monotonic increase of luminosity for as much as 4 mag over about 30 years. This event is one of the largest amplitude of monotonic variations with the longest timescale of any reported quasar's variability so far. Since the mid-infrared luminosity varied corresponding to the optical luminosity, the variation of J1258 should be due to an intrinsic change of the mass accretion rate rather than absorption variation. It is also not likely to be a discrete event such as tidal disruption event or microlensing, as it is currently undergoing significant variations. We discuss here the 4 mag brightening event, which is the most significant feature of J1258.

In this chapter, we estimate the physical quantities of J1258 and discuss the mechanism of this event from three aspects: the emission line shape, the timescale, and the change in the Eddington ratio.

2.5.1 The BEL shape

One of the characteristic features of J1258 is its unique shape of BELs. In some reported CSQs, such unusual shapes of BELs exist (MacLeod et al. (2019)). Such a broad line profile is an interesting feature, suggesting a disk-shaped rotating BLR gas or a binary black hole. It is essential to discuss this shape's origin because we use the line width to later derive the black hole mass.

According to the disk-wind model of Elitzur et al. (2014), the BLR is formed by the outflow from the accretion disk, and the shape of BEL is proposed to change in a sequence of steps depending on the parameter $L_{\rm BOL}/M^{2/3}$, where $L_{\rm BOL}$ is the bolometric luminosity, and M is the black hole mass. When the luminosity is lower than a certain value, no gas is supplied to form the broad-line region; AGNs in this phase become "true" type-2 AGNs. When the luminosity rises, the weak outflow from the accretion disk forms a BLR near the surface of the accretion disk, creating double-peaked BELs. When the luminosity rises more, the BEL distributes

a wide region, including far from the accretion disk and changes to a single-peaked BELs (type-1 AGN). Comparing the shape of the Hβ from the two SDSS spectra (Fig. 2.7), the transition of this object's Hβ shape is consistent with this model qualitatively, showing a single-peaked shape in its brighter phase and double-peaked shape in its fainter phase.

In the case of binary black holes, the emission lines can form various shapes depending on their masses and distances. One of the predicted features is that each component's velocity offset varies with the black holes' orbital motion (Liu et al. (2014)).

Volocity-resolved reverberation Mapping is an effective way to verify these scenarios. By measuring the time lag for each velocity component of the emission line, it is possible to detect outflow features (the time lag of the fast component should be smaller than the lag of the slow component). It is also possible to verify whether the velocity offset varies periodically based on the emission line shape's variation.

The emission line of J1258 has three peaks, and their velocity offsets are almost symmetric. In order to reproduce this kind of emission line shape in a binary system, we have to take into account a complex system. Here, we assume the disk-wind model of Elitzur et al. (2014), in which the spectra at the brightest period are closest to the type 1 AGN. In the next subsection, we estimate the physical quantities from the spectrum obtained when J1258 is closest to its brightest peak.

2.5.2 Physical values of J1258

Here, we estimate the bolometric luminosity, black hole mass, and Eddington ratio. For our calculations, we use the second SDSS spectrum (MJD=57481), which is the brightest one we have. First, we calculate the bolometric luminosity. To estimate from the optical spectrum, we adopt the formula for the bolometric correction in Netzer (2019).

$$L_{\mathrm{BOL}} = 40 \times \left(\frac{L(5100)}{10^{42}} \right)^{-0.2} \times L(5100) \tag{2.1}$$

Here, L_{BOL} is the bolometric luminosity (erg/s), $L(5100)$ is the observed luminosity (erg/s) at 5100 Å in the rest frame determined by power-law fitting of the spectrum. Substituting the $L(5100)$ obtained from the spectrum ($L(5100) = 10^{45.2}$ erg/s) into this equation, we derived $L_{BOL} = 10^{46.2}$ erg/s.

Next, we estimate the black hole masses. A black hole's virial mass can be estimated from from a single spectroscopic observation by assuming the formula

empirically determined by the Reverberation mapping of nearby AGN. Here, we use the results of Vestergaard & Peterson (2006) to calculate it. The formula is as follows.

$$\begin{aligned} \log_{10}\left(\frac{M_{\rm BH}}{M_\odot}\right) &= 0.91 + 0.5 \times \log_{10}\left(\frac{L(5100)}{10^{44}}\right) \\ &+ 2 \times \log_{10}({\rm FWHM(H}\beta)) \end{aligned} \tag{2.2}$$

Here, $M_{\rm BH}$ is the black hole mass, and the FWHM(Hβ) is the full width at half maximum (km/s) of the broad Hβ line. FWHM(Hβ) is calculated from the spectra after subtracting the power-law continuum and the [OIII] component; FWHM(Hβ) = 1.03×10^4 km/s. As a result, the black hole mass was estimated to be $10^{9.55}$ $M_\odot$. According to Vestergaard & Peterson (2006), the typical error of black hole masses derived from Eq. 2.2 is about 0.5 dex. The Eddington limiting luminosity of this black hole mass is $L_{\rm EDD} = 10^{47.6}$ erg/s, giving the Eddington ratio of 0.04 in this epoch. Although there is no spectrum at the faintest time, we can infer that the Eddington ratio changed from about 0.001 to 0.04, given that the amplitude of the brightening event in optical is about factor 40.

2.5.3 Timescale

We compare the duration of J1258's brightening event with the timescales of accretion disk variations. We consider four timescales; orbital timescale, thermal timescale, front propagation timescale, and viscous timescale (e.g., Stern et al. (2018), Noda & Done (2018)). The orbital timescale ($t_{\rm orb}$) is the timescale on which the disk orbits. The thermal timescale ($t_{\rm th}$) is expressed as $t_{\rm th} = t_{\rm orb}/\alpha$ with the viscosity of α. The cooling/heating front timescale ($t_{\rm front}$) is the radial propagation of the heating or cooling boundary across the disk. $t_{\rm front}$ is expressed as $t_{\rm front} = (H/R)^{-1} t_{\rm th}$, where H is the thickness of the disk and R is the radius of the disk. The viscous timescale ($t_{\rm v}$) is the timescale that characterizes the mass flow, denoted by $t_{\rm v} = (H/R)^{-2} t_{\rm th}$. Stern et al. (2018) estimated each of these timescales as follows.

$$
\begin{aligned}
t_{\rm orb} &\sim 10\ {\rm days} \left(\frac{M_{\rm BH}}{10^8 M_\odot}\right) \left(\frac{R}{150 R_{\rm g}}\right)^{3/2} \\
t_{\rm th} &\sim 1\ {\rm yr} \left(\frac{\alpha}{0.03}\right)^{-1} \left(\frac{M_{\rm BH}}{10^8 M_\odot}\right) \left(\frac{R}{150 R_{\rm g}}\right)^{3/2} \\
t_{\rm front} &\sim 20\ {\rm yr} \left(\frac{H/R}{0.05}\right)^{-1} \left(\frac{\alpha}{0.03}\right)^{-1} \left(\frac{M_{\rm BH}}{10^8 M_\odot}\right) \left(\frac{R}{150 R_{\rm g}}\right)^{3/2} \\
t_{\rm v} &\sim 400\ {\rm yr} \left(\frac{H/R}{0.05}\right)^{-2} \left(\frac{\alpha}{0.03}\right)^{-1} \left(\frac{M_{\rm BH}}{10^8 M_\odot}\right) \left(\frac{R}{150 R_{\rm g}}\right)^{3/2}
\end{aligned}
$$

$R_{\rm g}$ is the gravity radius defined as $GM_{\rm BH}/c^2$. We calculated the above four timescales for J1258, assuming that radiation in optical (typical temperature is 10^{3-4} K) is dominant at about $150R_{\rm g}$ in the standard disk model. Then, each timescale is calculated as follows: $t_{\rm orb} \sim 300$ days, $t_{\rm th} \sim 30$ years, $t_{\rm front} \sim 600$ years, $t_{\rm v} \sim 12,000$ years. The results indicate that 30 years is the closest to the thermal timescale.

On the other hand, Stern et al. (2018) points out that substituting other plausible values for α and H/R can significantly change these values. The disk is likely to heat up and inflate to $H/R \sim 0.1$ without the assumption in the standard thin disk model (Shakura & Sunyaev (1973)) of no torque at the inner edge of the accretion disk (e.g., Agol & Krolik (2000)). Also, King et al. (2007) argues that the viscosity α is likely to be ~ 0.3 from observations. In that case, the timescale is rewritten as follows: $t_{\rm orb} \sim 300$ days, $t_{\rm th} \sim 3$ years, $t_{\rm front} \sim 30$ years, $t_{\rm v} \sim 300$ years.

Thus, this phenomenon can be explained by thermal process or heating front propagation in terms of timescales (Ross et al. (2018)). A situation in which a thermal process induces a brightening phenomenon is that the entire disk is heated by high energy radiation from a small central region (Shappee et al. (2014), Dexter et al. (2019)). However, we consider this situation is unlikely to occur because the Hβ variation lags behind the continuum variation (see Fig. 2.10), suggesting that the BLR is ionized by the accretion disk rather than the high energy radiation from the central region.

2.5.4 Eddington ratio

Noda & Done (2018) explained extremely variable AGNs with a disk state transition (switch between low/hard state to high/soft state) and thermal front propagation. They divided extremely variable AGNs into three categories:

1. One showing a state change due to disc evaporation/condensation associated with a factor 2–4 decrease/increase in luminosity
2. One with mass accretion rate change due to the thermal front propagation
3. One showing both

(1) and (3) accompany a changing-look phenomenon, a significant change of BEL, but (2) does not. In other words, the brightening phenomenon of J1258, which shows a 40-fold brightening and a significant change in Hβ intensity, is classified as (3). Here, Noda & Done (2018) predicted that the Eddington ratio crosses the border about ~ 0.01 when a state transition like (1) or (3) happens. This prediction is confirmed in J1258 (the Eddington ratio changed from 0.001 to 0.04).

2.5.5 Comparison to other variable quasars

Most of the CSQs reported so far have had timescales of less than ten years and amplitudes of optical variability with less than factor 10 (e.g., Ichikawa et al. (2019)). The amount of variability is roughly proportional to the accretion disk area with the cooling/heating front propagates (MacLeod et al. (2019)). The size of the accretion disk, $t_{\rm th}$, and $t_{\rm front}$ are values that correlate the black hole mass. The black hole mass of J1258 is more than ten times larger than that of the previously reported CSQ black hole masses, which are typically about 10^{7-8} solar masses (e.g., MacLeod et al. (2016)). This suggests that the previously reported brightening phenomena of CSQ and J1258 can be interpreted as the same in terms of timescales and amplitudes. We expect that quasars with larger amplitudes of variability will be discovered in samples with larger black hole mass.

2.5.6 Comparison with Graham et al. (2020)

The quasar catalog used in this study, SDSS DR7Q, is included in the Million Quasar Catalog [2] v5.2 used in Graham et al. (2020). In both studies, CSQ samples were selected using the CRTS light curve. The main difference in the selection method is the analysis method of the light curve.

In our method, the full ranges of the light curves are fitted with linear functions. In Graham et al. (2020), they use Bayesian Blocks to estimate the amount of

[2]http://quasars.org/milliquas.htm

variability. The advantage of The advantage of the linear fitting is that it is sensitive to monotonic variations with timescales, which is longer than the light curve's full range. However, the disadvantage is that it misses the variations in various timescales between the light curves. The Bayesian Block, on the other hand, is capable of detecting any timescale variations that occur within the light curves. In figure 2.11, we plot how the CSQs listed in Graham et al. (2020) are distributed in the "slope-sigma plan" of our linear fitting. In fact, the results show that CSQs are distributed unevenly where the sigma is larger than 0.1 because they are recognized as scatters when they change on a timescale shorter than the interval of the light curve.

In the case of J1258, it was detectable by fitting with a linear function because of its monotonic brightening during all range of the light curve. However, such an object should also be detected by using the Bayesian Block. A possible reason is the indeterminacy of the emission line flux measurement on the unusual shape of the BELs; in Graham et al. (2020), Hβ is fitted with two Gaussians to obtain the flux. Therefore, in the case of Hβ with an unusual shape, the flux measurement may be significantly affected.

2.6 Conclusions

We discovered an extremely variable quasar, SDSS J125809.31+351943.0, brightened for 4 mag from 1983 to 2015. We identified this object as a new CSQ on the basis of the significant changes in the mid-infrared luminosity and in the intensity of the broad emission line. The weakness of the radio emission indicates that the variability is not caused by the jet. Furthermore, the flux in mid-infrared changed following the optical, which suggests that the accretion disk itself changed, rather than the variation of absorption. The object is characterized by an unusual shape of Hβ, and variability of 4 mag. The shape of Hβ is consistent with the disk-wind model by Elitzur et al. (2014). The variability of 4 mag is consistent with other variable quasars in terms of timescales and amplitude, except for the black hole mass of $\sim$ 10 times larger than other reported CSQs. This object is one of the most drastically variable objects so far, which will give us a new insight into accretion physics. To investigate further, a project of reverberation mapping of this object using 3.8-m Seimei Telescope in Japan is currently underway.

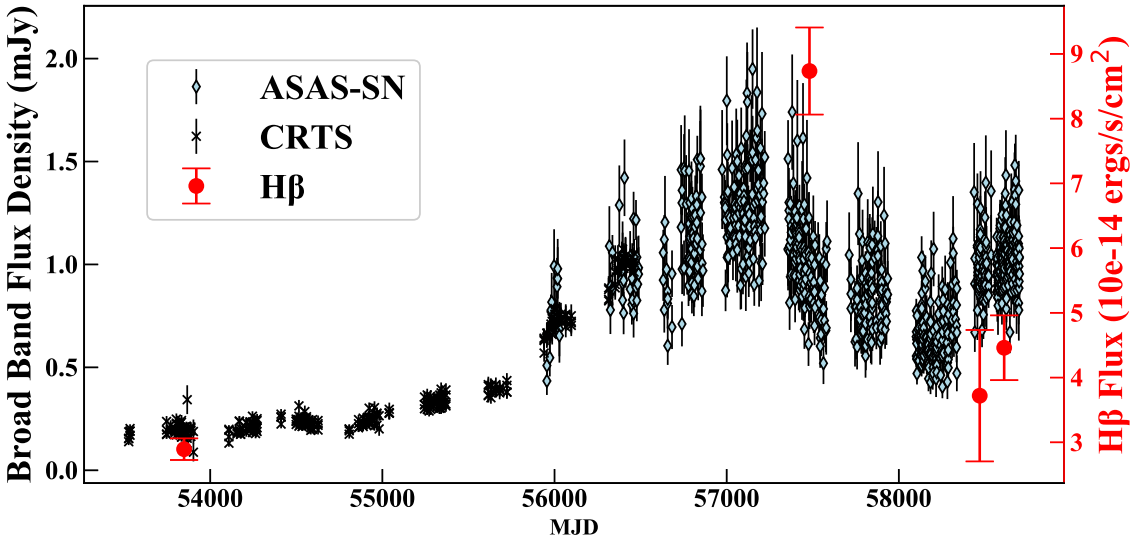

Figure 2.10: Time-series of broad-band flux density and the Hβ flux of J1258. Crosses and diamonds denote the CRTS and ASAS-SN, respectively, in the scale indicated on the left vertical axis. Red circles denote the Hβ flux in the scale indicated on the right vertical axis.

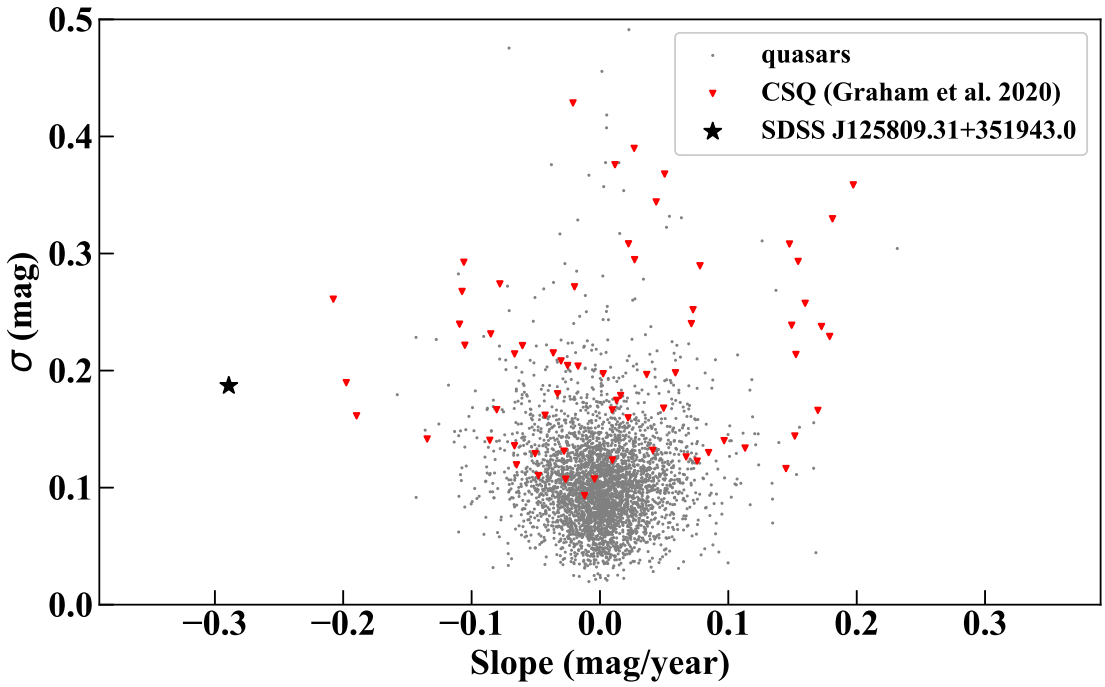

Figure 2.11: Same as Figure 2.2, but the CSQ sample of Graham et al. (2020) included in SDSS DR7Q is shown as red triangle.

Chapter 3

The relation between quasars' optical spectra and variability

This thesis chapter originally appeared in the literature as
Shumpei Nagoshi and Fumihide Iwamuro, *Publications of the Astronomical Society of Japan, Volume 74, Issue 5, pp.1198-1208*

3.1 Introduction to Chapter 3

One of the significant characteristics of quasars is their brightness variability, which we can observe at all wavelengths (e.g., Matthews & Sandage (1963); Peterson (1997)). Their amplitudes and timescales are diverse. In particular, the recent accumulation of survey data has led to studies of the long-term variability at various wavelengths. For example, (optical) Changing-Look/State Quasars (Although the exact definitions are different from Changing-Look Quasars and Changing-State Quasars, we unify the terminology to CLQ hereafter because we refer them in a same context), which show significant flux variations ($> 30\%$) in their broad emission lines, have been discovered in recent years (LaMassa et al. 2015; MacLeod et al. 2016, 2019; Ruan et al. 2016; Gezari et al. 2017; Wang et al. 2018; Noda & Done 2018; Ross et al. 2020; Graham et al. 2020; Nagoshi et al. 2021; Wada et al. 2021). In X-ray, quasars that the hydrogen column density of the same source changes drastically are known and called with the same name, (X-ray) Changing-look Quasar (e.g., Risaliti et al. (2009)). In addition, in the radio band, transit from the radio-quiet quasar to the radio-loud quasar has been reported (Nyland et al. 2020). The mechanisms of these phenomena are still under debate, but many papers infer

that they are expected to relate to the change in the mass accretion rate. In case of significant variation, such as CLQs, the result of X-ray observation (Husemann et al. 2016) and optical polarization observations (Hutsemékers et al. 2017) implies that they also undergo rapid changes in intrinsic accretion power. In this study, to conduct a statistical investigation of the status of quasars' accretion disk, we focused on the optical variation because a large amount of data linked to the accretion disk is available.

While quasars' light curves typically look random, the relation between luminosity and other physical quantities has been studied to understand their diverse variation pattern. Some studies have found that the smaller the Eddington ratio are, the more significant variable they are (e.g., Wilhite et al. (2008); MacLeod et al. (2010)). One interpretation of this correlation is that the inefficient mass accretion invokes intermittent avalanche-like accretion, resulting in the more significant variability (Takeuchi et al. 1995; Kawaguchi et al. 1998; Tachibana et al. 2020). However, in the case of this avalanche-induced variability, brightening and dimming have the same probability of occurrence if the observing period of the light curve is longer than a few years (Kawaguchi et al. 1998). On the other hand, studies of the structure-function of Sloan Digital Sky Survey (SDSS) light curves have shown that the probability of dimming is higher for long-term variability (de Vries et al. 2005), which cannot be explained by avalanche picture alone. In other words, we still poorly understand the relation between physical quantities and variability.

This study aims to find relations between random variability (in particular, variability with large amplitude and timescale) and the properties of quasars. One of the properties that characterize quasars' spectra is called Eigenvector 1 (EV1), which is a correlation that oxygen and iron emission line intensities are anti-correlated, found by principal component analysis of spectra (Boroson & Green 1992). Since EV1 is one of the few regularities that characterize the diverse quasars' spectra, we investigate the relation between locations on the EV1 plane and how they vary later; the EV1 plane here refers to the values of equivalent width (ratio) of $EW(\mathrm{FeII})/EW(\mathrm{H}\beta)$ ($\equiv R_{\mathrm{Fe_{II}}}$) and $\log_{10}\mathrm{EW}([\mathrm{OIII}]5007)$.

Through this investigation of the light curves, we can also expect to gain new insights into the nature of EV1. The physical interpretation of EV1 is limited because it was found as an empirical rule by statistical methods. Some studies suggested that the Eddington ratio is one of the origins of this anti-correlation because the emission lines are mainly photoionized by the UV continuum, which depends on the state of the accretion disk represented by the Eddington ratio (Boroson & Green 1992; Sulentic et al. 2000; Shen & Ho 2014). However, the correlation between the Eddington ratio and EV1 has not been confirmed in individual object. To examine

the contribution of the Eddington ratio to the EV1 based on the variability, we investigated the transition vectors (vectors showing where it moved from and to on the EV1 plane) on the EV1 plane associated with the changing luminosity of each object.

This paper consists of three sections of analyses, and the structure of this paper is as follows. Section 2 describes the methods and results for each of the three analyses. Section 3 discusses the results of them, as well as observational predictions and limitations of this study. The cosmological parameters used in this study are consistently $H_0 = 70$ km/s/Mpc, $\Omega_m = 0.3$ (These values are same as the Shen et al. (2011) catalog we used).

3.2 Method and Result

3.2.1 Sample

We visualize how positions on the EV1 plane and brightness variation relate from three aspects. In the first analysis, we show general trends of the relation between the position on the EV1 plane and how they change brightness later. Second, we show the correspondence relation between the position on the EV1 plane and the accretion state of the quasars. Finally, we show how each quasar moves on the EV1 plane due to its brightness variation. Each of the three analyses uses a different sample. First of all, we summarize the three samples here.

Sample 1 : We started from the quasars included in the Shen et al. (2011) catalog (hereafter referred to as S11). To obtain values of FeII, Hβ, and [OIII]5007, we picked up whose redshift is less than 0.8 (19,480 objects). Then, we excluded quasars with any equivalent width value of used emission lines below its error (remaining 15,446 objects). To estimate their brightness when the samples have these catalog values, we narrowed it down to whose spectroscopic observation period was less than two years from the observation period of the SDSS DR7 photometry (remaining 13,438 objects). As a result, 105,783 quasars in S11 were reduced to 13,438 quasars as Sample 1.

Sample 2 : This sample consists of CLQs, which are known to be a highly variable quasar population, to investigate the relationship between their position on the EV1 plane and the activity state. Among the sources in S11, 76 quasars that were later reported in MacLeod et al. (2019, 2016); Graham et al. (2020); Yang et al. (2018); Stern et al. (2018) as CLQs were listed as sample 2 (Table 1).

Sample 3 : To investigate how each quasar moves on the EV1 plane associated with its optical variation, we collected quasars with multiple spectra as Sample 3. From the 750,414 quasars in the Sloan Digital Sky Survey Data Release 16th Quasar catalog (Ahumada et al. (2020); SDSS DR16Q), we narrowed down the list to those with redshifts below 0.8 and multiple spectra available (8142 objects). We fitted their spectra to obtain the position on the EV1 plane. Finally, 2,839 sources remained as Sample 3, in which all emission lines of multiple spectra were fitted with errors less than 10% of their intensities.

3.2.2 Analysis 1: the distribution on the EV1 plane and the subsequent variation

We visualized the general relationship between the position on the EV1 plane and the brightness variations in ∼10 years from the data of Sample 1 in Figure 3.1. Each position of dot on the Figure 3.1 correspond to the values of S11 (we defined $R_{\rm Fe}$ as equivalent width of FeII in the range from 4434 Å to 4684 Å divided with the value of equivalent width of Hβ). The subsequent optical variations were obtained from the differences of the g-band magnitudes between SDSS DR7 (Abazajian et al. 2009) and Pan-STARRS DR1 (Chambers et al. 2016) catalogs. The SDSS photometric and spectroscopic observations of the target objects were made between 1999 and 2005 (the median year is 2002), while the Pan-STARRS observations were made between 2009 and 2014 (the median year is 2012); intervals of them are about ten years. Since the photometric system of Pan-STARRS is almost the same as that of SDSS with the systematic differences of less than 0.02 mag (Tonry et al. 2012), so we interpret the g-band photometric differences to represent how much brightness in the g-band magnitudes has changed in about ten years after the spectra were obtained.

Figure 3.1 shows the distribution on the EV1 plane with the amount of the magnitude variation for each group of brightening and dimming sources ("a brightening/dimming source" means the quasar that was brightening/dimming when their spectra were acquired). We plot brightening and dimming sources in different groups because their numbers are about three times different. There are 2,244 objects with magnitude increases of more than 0.15 mag, 6,136 with decreases of more than 0.15 mag, and 5,042 with variations less than 0.15 mag. The color of the symbols are smoothed using the surrounding points (the color represents the averaged magnitude variation of the points within the box of $\Delta R_{\rm FeII} = 0.1$ and $\Delta \log_{10} EW([\mathrm{OIII}]5007) = 0.1$ around each point).

From the color pattern on Figure 3.1, we can see that some relation exists

between the position on the EV1 plane and how their brightness change later. In the left panel of Figure 3.1, we can see that quasars located on the lower left side of the EV1 plane tend to dim more significantly. In the right panel of Figure 3.1, there looks to be a weak trend that quasars on the left side of the EV1 plane tend to brighten more significantly, but the sample size is smaller than dimming sources. When we compare the left panel and the right panel of Figure 3.1, we can see that dimming sources distribute a little lower than brightening sources on the EV1 plane. Overall, it is expected that there is a correspondence between the position on the EV1 plane and the activity change of the quasars.

3.2.3 Analysis 2: Distribution of CLQs on the EV1 plane

In this analysis, to confirm the correspondence relation between the position on the EV1 plane and the activity level of the quasars, we investigated the distribution of the CLQs whose activity states are known (Figure 3.2). We used 76 CLQs in Table 3.1 referred to the papers listed in it. In Figure 3.2, we plot CLQs in different markers corresponding to their activity states; red circles represent the bright state, and blue triangles represent the dim state. From Figure 3.2, we can see that the bright state and the dim state of CLQs are separated by the ridge of the distribution (the region of high distribution density contributing to the negative correlation) of other S11 quasars. In other words, the lower position on the EV1 plane corresponds to a bright (active) state, and the upper position corresponds to a dim (quiet) state for each quasar.

Table 3.1:: List of Changing-Look/State Quasars reported by 2020 and included in S11, ordered by RA (MacLeod et al. 2019, 2016; Graham et al. 2020; Yang et al. 2018; Stern et al. 2018). The SDSS Name, Redshift, $R_{\rm FeII}$, and log(EW) are referred to as the values from the S11. The amount of variation in g-band magnitudes from SDSS to Pan-STARRS is shown in Δg mag.

SDSS Name	State	Reference	Redshift	$R_{\rm FeII}$	$\log_{10}EW$([OIII])	Δg mag
000904.54−103428.7	Bright state	MacLeod et al. 2018	0.241	0.000 ± 0.014	1.670 ± 0.012	+1.37
002311.06+003517.5	Dim State	MacLeod et al. 2016	0.422	0.249 ± 0.111	1.376 ± 0.036	−0.88
011919.27−093721.7	Bright state	Graham et al. 2019	0.383	0.120 ± 0.088	1.336 ± 0.109	+0.05
015957.64+003310.4	Bright state	MacLeod et al. 2016	0.312	0.000 ± 0.035	1.082 ± 0.062	+0.08
022014.57−072859.2	Dim State	Graham et al. 2019	0.213	0.150 ± 0.055	1.325 ± 0.046	−1.42
022556.07+003026.7	Bright state	MacLeod et al. 2016	0.504	0.654 ± 0.369	0.913 ± 0.190	+0.86
022652.24−003916.5	Bright state	MacLeod et al. 2016	0.625	0.407 ± 0.323	0.937 ± 0.280	+1.30
025505.68+002522.9	Bright state	Graham et al. 2019	0.353	0.266 ± 0.068	1.070 ± 0.057	+2.44
074511.98+380911.3	Bright state	MacLeod et al. 2018	0.237	0.485 ± 0.127	0.943 ± 0.043	+1.09
075440.32+324105.2	Dim State	Graham et al. 2019	0.411	0.344 ± 0.065	1.880 ± 0.018	−0.34
081425.89+294115.6	Bright state	Graham et al. 2019	0.374	0.000 ± 0.012	1.570 ± 0.037	+1.41
081632.12+404804.8	Bright state	Graham et al. 2019	0.701	0.104 ± 0.112	1.214 ± 0.105	+1.23
082033.30+382419.7	Bright state	Graham et al. 2019	0.648	0.142 ± 0.126	1.355 ± 0.070	+0.41
082930.59+272822.7	Bright state	Graham et al. 2019	0.321	0.000 ± 0.014	1.653 ± 0.030	+0.22
083225.34+370736.2	Dim State	Graham et al. 2019	0.092	0.000 ± 0.011	1.617 ± 0.027	−0.15
083236.28+044505.9	Dim State	Graham et al. 2019	0.292	0.000 ± 0.012	1.777 ± 0.030	−1.27
084716.03+373218.0	Dim State	Graham et al. 2019	0.454	0.261 ± 0.046	2.185 ± 0.016	−0.33
084957.78+274729.0	Bright state	Yang et al. 2018	0.299	0.271 ± 0.130	1.140 ± 0.033	+0.53

SDSS Name	State	Reference	Redshift	$R_{\rm FeII}$	$\log_{10} EW$([OIII])	Δg mag
091357.26+052230.7	Bright state	Graham et al. 2019	0.346	0.111 ± 0.044	1.110 ± 0.052	+1.15
092441.08+284730.3	Bright state	Graham et al. 2019	0.464	0.109 ± 0.078	1.772 ± 0.031	−0.07
092736.79+153823.1	Bright state	Graham et al. 2019	0.555	0.099 ± 0.268	1.946 ± 0.115	+0.15
092836.78+474245.8	Bright state	Graham et al. 2019	0.830	0.318 ± 0.200	1.916 ± 0.185	+0.86
093017.70+470721.0	Dim State	Graham et al. 2019	0.160	0.000 ± 0.008	1.669 ± 0.017	−0.79
094620.86+334746.9	Dim State	Graham et al. 2019	0.239	0.616 ± 0.044	1.326 ± 0.053	−1.08
095750.03+530104.7	Dim State	Graham et al. 2019	0.437	0.208 ± 0.130	1.960 ± 0.036	−1.39
100220.17+450927.3	Bright state	MacLeod et al. 2016	0.400	0.454 ± 0.108	0.616 ± 0.163	+1.14
100256.21+475027.7	Dim State	Graham et al. 2019	0.391	0.000 ± 0.014	2.021 ± 0.015	−0.59
100343.23+512610.8	Dim State	Graham et al. 2019	0.431	0.469 ± 0.174	1.407 ± 0.098	−0.65
101152.98+544206.4	Bright state	Runnoe et al. 2016	0.246	0.837 ± 0.103	0.812 ± 0.175	+1.40
102152.34+464515.6	Bright state	MacLeod et al. 2016	0.204	0.230 ± 0.041	1.161 ± 0.029	+1.25
102613.90+523751.2	Dim State	Graham et al. 2019	0.259	0.029 ± 0.040	1.700 ± 0.023	+0.13
102817.67+211507.4	Dim State	Graham et al. 2019	0.365	0.123 ± 0.054	2.012 ± 0.030	−0.55
104254.79+253713.6	Dim State	Graham et al. 2019	0.603	0.000 ± 0.010	2.138 ± 0.024	−0.64
105203.55+151929.5	Bright state	Stern et al. 2018	0.303	0.000 ± 0.017	1.284 ± 0.041	+0.82
105553.51+563434.4	Dim State	MacLeod et al. 2018	0.322	0.325 ± 0.215	1.590 ± 0.037	−1.03
110455.17+011856.6	Bright state	Yang et al. 2018	0.575	0.933 ± 0.259	1.091 ± 0.330	+2.10
111329.68+531338.7	Bright state	MacLeod et al. 2018	0.239	0.148 ± 0.079	1.088 ± 0.055	+1.25
111617.80+251035.7	Bright state	Graham et al. 2019	0.534	0.000 ± 0.011	1.348 ± 0.032	−0.25
113111.14+373709.1	Bright state	Graham et al. 2019	0.448	0.000 ± 0.011	1.543 ± 0.029	+1.55
113706.84+013947.9	Bright state	Graham et al. 2019	0.193	0.043 ± 0.023	1.045 ± 0.029	+0.30
114408.90+424357.5	Bright state	Graham et al. 2019	0.272	0.000 ± 0.013	1.443 ± 0.019	+0.48
115039.32+363258.4	Bright state	Yang et al. 2018	0.340	0.260 ± 0.115	1.431 ± 0.047	+1.24
115227.48+320959.4	Bright state	Yang et al. 2018	0.374	0.075 ± 0.075	1.658 ± 0.027	+1.30
120130.63+494048.9	Dim State	Graham et al. 2019	0.392	0.240 ± 0.115	1.451 ± 0.045	−0.79
120442.10+275411.7	Dim State	Graham et al. 2019	0.165	0.254 ± 0.031	2.122 ± 0.020	−0.04
123215.16+132032.7	Bright state	Graham et al. 2019	0.286	0.094 ± 0.038	1.296 ± 0.032	−0.02
123819.62+412420.5	Bright state	Graham et al. 2019	0.499	0.000 ± 0.011	1.592 ± 0.069	+1.01
125757.23+322929.2	Dim State	Graham et al. 2019	0.806	0.000 ± 0.027	1.032 ± 0.272	+0.06
132457.29+480241.2	Bright state	MacLeod et al. 2016	0.272	0.304 ± 0.107	1.184 ± 0.044	+1.11
134822.31+245650.1	Bright state	Graham et al. 2019	0.293	0.583 ± 0.064	0.943 ± 0.063	+0.48
143455.31+572345.0	Bright state	MacLeod et al. 2018	0.175	0.094 ± 0.032	1.086 ± 0.089	+1.65
144202.82+433708.7	Bright state	Graham et al. 2019	0.231	0.000 ± 0.011	1.201 ± 0.020	+0.57
144702.87+273746.7	Bright state	Graham et al. 2019	0.224	0.000 ± 0.015	1.694 ± 0.015	+1.39
145022.73+102555.4	Dim State	Graham et al. 2019	0.790	0.116 ± 0.055	1.264 ± 0.140	−0.65
145755.38+435035.4	Dim State	Graham et al. 2019	0.528	0.243 ± 0.096	1.325 ± 0.101	−0.17
151604.24+355024.8	Bright state	Graham et al. 2019	0.592	0.172 ± 0.199	1.299 ± 0.076	+1.00
153354.59+345504.1	Bright state	Graham et al. 2019	0.753	0.000 ± 0.011	1.456 ± 0.172	+0.15
153612.80+034245.7	Bright state	MacLeod et al. 2018	0.365	0.072 ± 0.047	0.913 ± 0.063	+0.40
153734.06+461358.9	Bright state	MacLeod et al. 2018	0.378	0.540 ± 0.166	0.823 ± 0.203	+1.09
155651.38+321008.1	Bright state	Graham et al. 2019	0.350	0.460 ± 0.063	1.059 ± 0.074	+0.33
160111.26+474509.6	Bright state	MacLeod et al. 2018	0.297	0.157 ± 0.071	0.982 ± 0.067	+1.48
160742.94+432816.4	Bright state	Graham et al. 2019	0.596	0.102 ± 0.027	1.723 ± 0.033	+1.08
161400.30−011006.0	Bright state	Graham et al. 2019	0.253	0.219 ± 0.055	1.175 ± 0.062	+0.71
161711.42+063833.4	Bright state	MacLeod et al. 2018	0.229	0.000 ± 0.008	1.876 ± 0.009	+2.22
162415.02+455130.0	Bright state	MacLeod et al. 2018	0.481	0.517 ± 0.128	1.268 ± 0.057	+1.14
210200.42+000501.8	Bright state	MacLeod et al. 2018	0.329	0.108 ± 0.082	0.440 ± 0.180	+0.89
214613.31+000930.8	Dim State	MacLeod et al. 2016	0.621	0.000 ± 0.012	1.757 ± 0.054	−0.22
220537.71−071114.5	Bright state	MacLeod et al. 2018	0.295	0.451 ± 0.156	1.081 ± 0.044	+1.15
224829.47+144418.0	Bright state	Graham et al. 2019	0.424	0.319 ± 0.096	0.754 ± 0.082	+1.44
225240.37+010958.7	Dim State	MacLeod et al. 2016	0.534	0.181 ± 0.244	1.352 ± 0.074	−0.75
231207.61+140213.3	Dim State	Graham et al. 2019	0.357	0.074 ± 0.025	1.459 ± 0.062	−0.91
233136.83−105638.3	Dim State	Graham et al. 2019	0.373	0.245 ± 0.078	1.117 ± 0.050	−0.90
233317.38−002303.4	Dim State	MacLeod et al. 2016	0.513	0.316 ± 0.308	1.524 ± 0.064	−1.36
234307.38+003854.7	Bright state	Yang et al. 2019	0.667	1.503 ± 1.069	0.930 ± 0.347	+1.01
235107.43−091318.0	Bright state	MacLeod et al. 2018	0.355	0.051 ± 0.057	0.942 ± 0.066	+1.25
235439.14+005751.9	Dim State	Graham et al. 2019	0.390	0.082 ± 0.083	1.729 ± 0.042	+0.53

3.2.4 Analysis 3: transition vectors on the EV1 plane of each object

To understand how each quasar moves on the EV1 plane accompany with optical variation, we visualized transition vectors on the EV1 plane using Sample 3

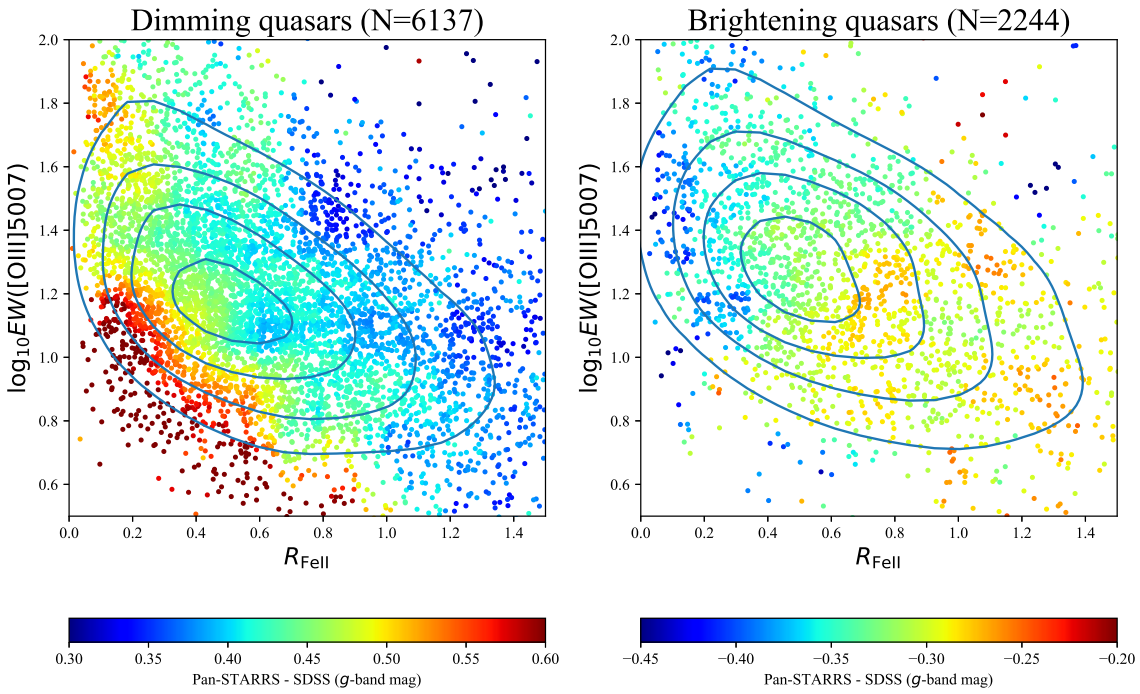

Figure 3.1: Distribution of dimming/brightening quasars on the EV1 plane. The location of each point is based on the S11 catalog with the subsequent brightness variation indicated by the symbol color. The contour lines show the distribution density of each quasar, estimated using Gaussian kernel density estimation. From the outside, they represent the 90, 70, 50, and 30 percent probability of existence. The color bar is the magnitude difference between Pan-STARRS and SDSS in the g-band, which is approximately the amount of brightness variation 10 years after the spectra were acquired. The color of each point is averaged for the points within ± 0.1 in the x and y-axis direction.

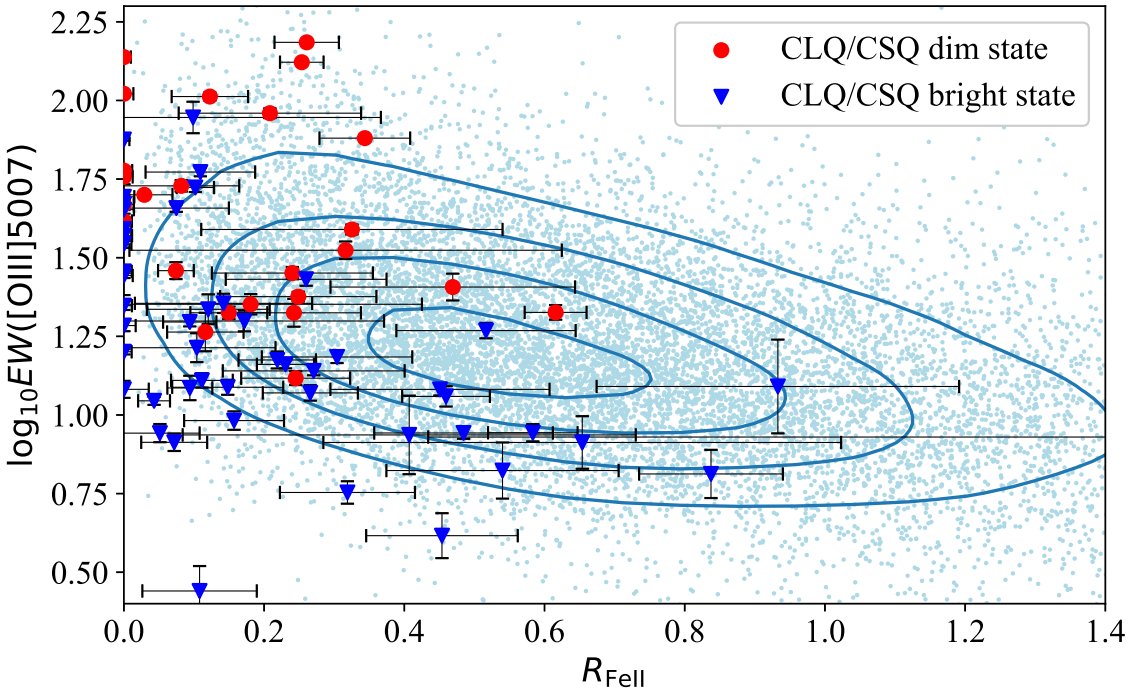

Figure 3.2: Location of CLQs listed in Table 3.1 on the EV1 plane. The red circles represent CLQs in the dim state, and the blue triangles represent CLQs in the bright state. The light blue dots represent other quasars in S11 with redshifts below 0.8. The distribution densities are shown as contours using Gaussian kernel density estimation. From the outside, each contour represents the 90th, 70th, 50th, and 30th percentiles.

(Figure 3.3). We fitted the spectra in this sample (8,142 sources) with PyQSOfit (Guo et al. 2018) to determine their equivalent widths of emission lines. The wavelength range that we used for fitting is 4434-5535 Å at the rest frame. The components applied in the fitting were power-law continuum, iron emission line templates (Boroson & Green 1992), and two Gaussian components imposed for each Hβ, [OIII]5007, and [OIII]4959. The velocity offsets and the line width for the narrow emission lines ([OIII]5007, [OIII]4959) were set to be equal. Each measurement error was estimated using the Monte Carlo method, which perturbs the flux based on the input error and the fitting was repeated 20 times. The equivalent widths were calculated from the fitting results. The wavelength range of FeII emission lines is 4435-4685 Å at rest frame in this calculation. We narrowed down the list to 2,839 sources for which all the measured emission lines in the multiple spectra were obtained with an error of less than 10%. Figure 3.3 shows a graph of the transition vectors of each source on the EV1 plane, connected by straight gray arrows. From the fitting results, we classified the variability of the sources on the basis of the assumption that the [OIII]5007 luminosity is constant. Among these sources, those with $\Delta\log_{10}EW$([OIII]5007) greater than 0.15 are grouped as "dimming sources" (325 sources), and those with $\Delta\log_{10}EW$([OIII]5007) less than -0.15 are grouped as "brightening sources" (156 sources). The difference in the periods of observations of the spectra being compared is typically about eight years in the rest frame (the median value is 3,024 days, and 80% is longer than 1,500 days). Based on the initial (the first observation in multiple spectra) $R_{\rm FeII}$ values, the sources are divided into seven groups, whose averaged transition vectors are represented by red thick arrows.

As a result, we can see that both the brightening and dimming sources follow a similar path and swap positions on the EV1 plane. They go back and forth between the lower left and upper right on the EV1 plane, each position is expected to correspond to a bright state and a dim state from Analysis 2. To compare the transition vectors of brightening and dimming, we illustrate a histogram of the inclination of the transition vectors (Figure 3.4). In order to quantitatively verify the two distributions in Figure 3.4, we performed a two-component Kolmogorov-Smirnov test. The p-value is 0.83, indicating that the Null hypothesis that these two distributions are the same is not rejected. This result confirms that quasars move in almost the same direction when they brighten or dim, and they transit to the opposite state.

We also note here that when each quasar brightens, $R_{\rm FeII}$ decreases and vice versa. This means that $R_{\rm FeII}$ is anti-correlated with the Eddington-ratio if we focus on each quasar. This anti-correlation is opposite to the general trend derived from the statistical analysis of single epoch spectra of quasars (Boroson & Green 1992;

Sulentic et al. 2000; Shen & Ho 2014).

3.3 Discussion

This study explored the relationship between optical variability and spectra through three analyses. The first analysis used the catalog values of S11 to visualize the distribution on the EV1 plane with the subsequent variability. Second, we used a sample of CLQs to show the distribution on the EV1 plane depending on their bright or dim status. Third, we visualized the transition of the positional transition of multi-epoch spectra on the EV1 plane. We summarize the main results of these analyses below.

- Tendency of subsequent brightness variation is related to the position on the EV1 plane. Sources that dim later distribute on the lower side of EV1, and sources that brighten later distribute upper side (Analysis 1; Figure 3.1).
- In general, significantly variable quasars distribute on the left side of the distribution ridge on the EV1 plane. (Analysis 1; Figure 3.1)
- In the case of CLQs, bright/dim state objects are located at the lower-left/upper-right side of the distribution ridge on the EV1 plane, respectively (Analysis 2; Figure 3.2).
- On the EV1 plane, the brightening and dimming sources cross the ridge of the general distribution and follow similar transition vectors, moving back and forth between the lower left and upper right. (Analysis 3; Figure 3.3)
- When we focus on an individual object with multi-epoch spectra, $R_{\rm FeII}$ is anti-correlated to the Eddington ratio. (Analysis 3; Figure 3.3 and Figure 3.4)

These are new results that confirm link quasars' random variation with spectral features. Based on them, we will discuss from four viewpoints in the following subsections; distribution on the EV1 plane, transition vectors on the EV1 plane, limitations of the present method, and observational predictions.

3.3.1 Distribution on the EV1 plane

Since EV1 is a relation found phenomenologically using principal component analysis (Boroson & Green 1992), it is still poorly understood physically. Therefore, this

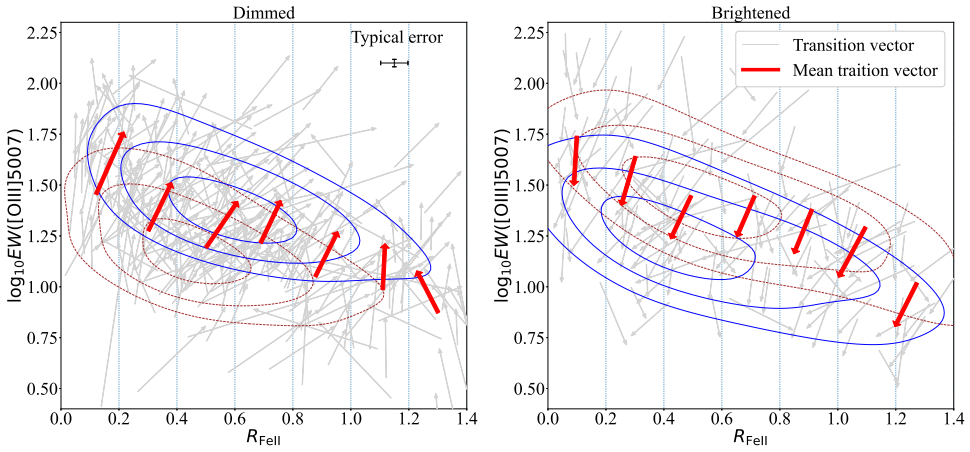

Figure 3.3: Transition vectors of quasars with multi-spectra on the EV1 plane. The left panel plots the dimmed sources, and the right panel plots the brightened sources. The positions on the EV1 plane of the newest and oldest spectra of the same source are calculated, and the same source is connected by a gray line. Only the spectra with the error less than 10% of each emission line are used, and the mean value of the errors is indicated by a cross mark in the upper center of the left panel. The vertical dotted line divides the $R_{\rm FeII}$ into sections of 0.2 each. The red thick arrows show the average of the transition vectors of the objects whose starting points are in each of the seven regions separated by the dotted lines. Contours in blue solid brown dotted lines represent distribution after/before the variation using Gaussian kernel density estimation, respectively.

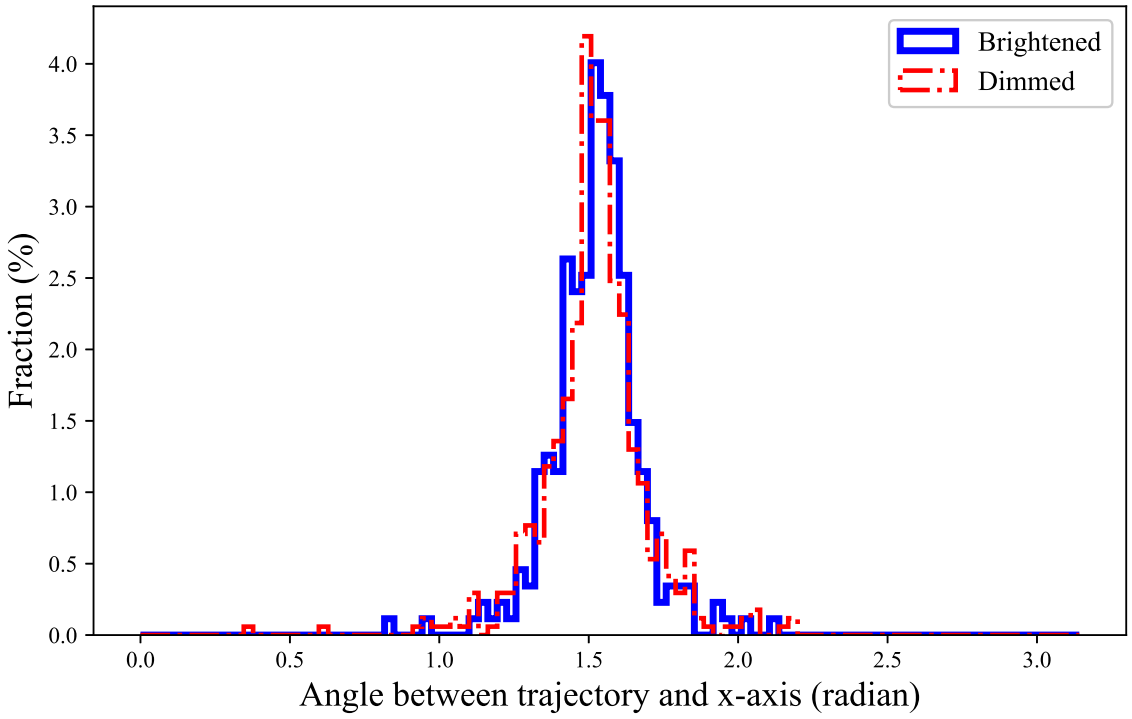

Figure 3.4: Probability distribution of the angle between the transition vectors and the x-axis expressed in radians. The blue line represents the brightened sources, and the red dashed-dotted line represents the dimming sources.

section discusses the meaning of each of the values of EW([OIII]5007) and $R_{\rm FeII}$ that constitutes EV1.

[OIII]5007 is a narrow emission line commonly observed in quasars. Narrow lines are usually powered by ionization photons from the accretion disk, and thus are affected by the energy distribution of the disk. However, the timescale for the change in [OIII]5007 brightness is considered to be sufficiently more prolonged than the observation timescale, because the [OIII]5007 emission region is substantially extended ($\sim$100 pc from the center). In other words, this region reflects the history of changes in quasar activity over the past $\sim$100 years. Since we are interested in the amount of EW([OIII]5007) changes over the past $\sim$10 years, we interpret that the change in EW([OIII]5007) is dominated by the continuum variation.

$R_{\rm FeII}$ has been considered to be a positively correlated indicator of mass accretion rate based on the trends of many objects (Boroson & Green 1992; Sulentic et al. 2000; Shen & Ho 2014). The result of Analysis 3, however, shows that a negative correlation exists in the variation of individual quasar, with $R_{\rm FeII}$ decreasing as brightening. Some reverberation mapping studies have confirmed that the FeII emission region is more extended than the Hβ region (Barth et al. 2013; Zhang et al. 2019; Hu et al. 2020; Lu et al. 2021; Gaskell et al. 2022). This may cause slower and smoother variation of FeII emission lines compared to that of Hβ, which makes $R_{\rm FeII}$ temporarily smaller/larger during brightening/dimming, respectively.

How much extend FeII emission region is under debate, but it is likely comparable to the dust sublimation radius (e.g., He et al. (2021); Mishra et al. (2021); Gaskell et al. (2022)). The typical sublimation radius is $\sim$ 100 light days (Namekata & Umemura 2016), but the typical difference in observation epoch in Analysis 3 is $\sim 1,000$ days. Thus, In the case of Analysis 3, only the difference in the distributed radius of Hβ and FeII is not the dominant explanation for the negative correlation, because the light crossing time of the FeII emission region is significantly shorter than the observation timescale.

Although it is commonly accepted that $R_{\rm FeII}$ has a correlation with the Eddington ratio, the Pearson correlation coefficient between log(Edd) and log($R_{\rm FeII}$) is as low as 0.25 for the Sample 1. The scatter in the distribution may have been increased by the differences in the distribution of Hβ and FeII, the selection method of Analysis 3, or other factors related to the origin of EV1 may have increased. Further research is needed to clarify how much they are correlated as well as the effect of the temporal variation of $R_{\rm FeII}$ on it. High precision reverberation mapping will identify the location of the FeII emission region, one of the clues to the actual physical meaning of $R_{\rm FeII}$.

On the other hand, the overall EV1 of S11, EW([OIII]5007) and $R_{\rm FeII}$ are weakly correlated (Pearson's correlation coefficient is -0.35). The major factors that determine this correlation of emission line ratio are elemental composition, electron density, electron temperature, and energy distribution of ionizing photons. In timescale of some years, the key factor that contributes to the variation is the energy distribution of ionizing photons, i.e., the accretion state characterized by the Eddington ratio. When we interpret that the whole EV1 correlation is produced by a certain systematic variation of the SED of each source according to the Eddington-ratio change (modifying the structure of the accretion flow) as suggested in Shen & Ho (2014), the vertical scatter along the ridge of the distribution on the EV1 plane reflects the current level of mass accretion activity normalized by the averaged past activity over $\sim$ 100 years (the timescale of [OIII]5007 variation).

We also mention intrinsic scatter contribution around the ridge on the EV1 plane. The intrinsic scatter (including a variation on timescales sufficiently longer than observations, opening angle of the UV continuum radiation, the profile of UV continuum, metallicity, and the possible contribution of Lyα pumping (Sarkar et al. (2021), and references therein)) and the short-term variation are expected to contribute to the spread of the distribution on the EV1 plane. The vertical scatter of $\log_{10}EW$([OIII]5007) on the EV1 plane of Sample 1 quasars has a standard deviation of 0.28. Assuming that the luminosity of [OIII]5007 does not change during observations, a 0.28 change in $\log_{10}EW$([OIII]5007) means that the continuum changes by about 0.71 mag. On the other hand, the structure function of 20 years light curves indicates that the standard deviation of the magnitude difference between the data with 10 years separation is about 0.3 mag (Stone et al. 2022). This comparison indicates that the scatter of the distribution on the EV1 plane is more extensive than would be explained by the typical continuous light variation over ten years.

In summary, though intrinsic scatter exists, we interpret that the location on the EV1 plane is significantly affected by each quasar's activity level normalized by the average of $\sim$ 100 years. The more out of the peak of the distribution on the EV1 plane, the more deviate the activity state is, compared to the typical state for the object. In other words, quasars at the lower on the EV1 plane are in temporarily bright state, while those at the higher on the EV1 plane are in temporarily dim state.

3.3.2 Transition vectors on the EV1 plane

Figure 3.1 shows a clear difference in subsequent brightness variation depending on the locations on the EV1 plane. From Figure 3.2 and Figure 3.3, we can see that the lower left side of the EV1 plane corresponds to the quiescent phase for the source, while the upper right side corresponds to the active phase. Figure 3.3 shows the averaged transition vectors located across the ridge of the distribution, from the quiescent (lower-left) region to the active (upper-right) region, and vice versa. Furthermore, the transitions on the EV1 plane follow the same path as the results of Figure 3.3 and Figure 3.4. From these results, interpreting the distribution on the EV1 plane as the current activity level normalized by the activity level over the past several hundred years (the timescale of [OIII]5007 changes), it is suggested that the activity level transits between the quiescent and active phases across the equilibrium state for each object.

The periodic accretion disk fluctuations are similar to the limit cycle caused by the viscous and thermal instability of the accretion disk. Based on the standard disk models consistent with the SEDs of many AGNs, thermal instability is known to occur in situations where the radiation pressure of the accretion disk is more dominant than the gas pressure (e.g., Lin & Shields (1986)). In thermally unstable conditions, the radius of the 50-150R_g (R_g is the gravitational radius) of the accretion disk is known to transit between a state composed of ionized hydrogen and a state composed of neutral hydrogen, which has been confirmed in dwarf novae and X-ray binary stars. It has also been shown that state transitions can occur in the accretion disks of AGN, making it one of the major causes of CLQs (e.g., Noda & Done (2018)). The disk instability model predicts the existence of a limit cycle, which has also been proposed for AGNs (Lin & Shields 1986). Moreover, the transition timescale of CLQs ($\sim$ several years) is comparable with that of the disk instability ($\sim$ 10 years).

Here, we propose one possibility that the evolutionary process of AGN is able to be inferred from their distribution on the EV1 plane. Since there is a time lag of $\sim$ 100 years between the [OIII]5007 luminosity and the central activity, we can infer the history of quasars' activity using [OIII]5007. For example, when a quasar ends its activity in $\sim$ 100 years, the [OIII]5007 luminosity is expected to be large compared to the central core (Ichikawa et al. 2019). If we assume quasars generally fade to their end of activity (Caplar et al. (2020) observationally confirmed that most quasars are fading), the central luminosity is expected to generally decrease in the long-term ($\sim$ 100 years) in addition to short-term (months to years) temporal variation. Under this assumption, quasars' central luminosity

compared to [OIII]5007 will also be decreased because there is ~ 100 years of time lag between them. That is to say, if a quasar is close to the end of its activity, the EW([OIII]5007) is expected to be larger (the upward on the EV1 plane). Now, it has been known that objects with small black hole masses and large Eddington ratios, such as Narrow Line Seyfert 1, are characterized by large $R_{\rm FeII}$, while objects with large black hole masses and small Eddington ratios are characterized by small $R_{\rm FeII}$ (Marziani et al. 2018). When we interpret this fact as that the quasars with larger $R_{\rm FeII}$ are in the early stage of an actively growing AGN, and the smaller $R_{\rm FeII}$ means the late stage of the growth, which can explain the negative correlation of the EV1 plane. Also, such an interpretation can explain that the significantly variable sources are mostly distributed on the left side of the EV1 plane (Fig 3.1). Objects on the upper left (larger EW([OIII]5007)) are less efficient at mass accretion and more prone to intermittent mass accretion like an avalanche (Takeuchi et al. 1995; Kawaguchi et al. 1998; Tachibana et al. 2020) because they are in a quiescent phase compared to past AGN activity. In summary, our hypothesis is that the sources distributed in the lower right on the EV1 plane are in the active growth phase of AGN, while those in the upper left are in the terminal phase of AGN activity.

To summarize what we found from the quasars' trajectories on the EV1 plane, if the ridge of the distribution on the EV1 plane corresponds to averaged activity level (as mentioned in Section 3.3.1), the status variation across the ridge are expected to oscillate around the ridge. In fact, quasars with large brightness variation generally transit across the ridge along the similar path during both brightening and dimming. Based on these pieces of circumstantial evidence, it seems that quasars' large variations, such as CLQs, are generally repeating phenomena.

3.3.3 observational predictions

If quasars' significant variation is due to disk instability of the accretion disk occurring repetitively, three things are expected to be observationally confirmed.

- Since the timescale inferred from the disk instability model is shorter for brightening and longer for dimming as confirmed in dwarf novae (Osaki 1996), it is expected that the CLQs discovered in the future will be more likely to be dimming sources regardless of the selection bias.

- The known CLQs are more likely to transit activity state later than typical quasars. We suggest that known CLQs are good targets to follow up to investigate the state transition process observationally.

- The distribution of the dimming/brightening CLQs in the EV1 plane (i.e., Figure 3.2) will be further enhanced by newly discovered CLQs in the future. This difference in distribution can be applied to the sample selection when searching for new CLQs. This suggests that the subsequent variability of quasars can be predicted from their spectra.

The above observational predictions can be verified in the future with the development of survey observations such as The Large Synoptic Survey Telescope (LSST Science Collaboration et al. 2009). On the contrary, the results obtained in this study should be treated with a certain degree of caution, because they were obtained from a sample with a non-uniform observation period. In the next section, we discuss the limitations of this study.

3.3.4 Limit of this method and Future work

In this paper, we showed the relation between optical variation and spectra. Our analysis tried to use as large samples as possible to reduce selection bias of the sample. However, we understand that the method in this paper has two shortcomings, which we should keep in mind.

The first is that the timing of the spectroscopic and photometric observations is determined by chance, making the intervals between observations not uniform. Although the Pan-STARRS value is used as the magnitude of the object about 10 years later than the SDSS, the interval between the two is actually uncertain for several years. It should be noted that the results of this paper only claim to reveal an overall qualitative trend by using a large sample.

Second, we still have a limited understanding of EV1. Although the correlation was discovered by a phenomenological approach among various physical quantities, the mechanism seems not simple as shown in this study. Further investigation is required for this issue.

It is expected that the above two problems will be improved by future research. The first problem is expected to be solved by revalidating the data on the basis of homogenized data accumulated in the future. The second problem is expected to be solved by clarifying the elemental (FeII, in particular) distribution by reverberation mapping and interpreting the trend on EV1 from the physical model.

3.4 Conclusion

In this study, we visualized the relationship between optical variation and location on the EV1 plane. We summarize what we found and what can be inferred from the results below.

- There is a correlation between quasars' optical variability and their distribution on the EV1 plane, in which the significantly dimming objects tend to transit across the distribution ridge from lower-left to upper-right, and vice versa for the brightening objects.
- R_{FeII} is anti correlated to the Eddington-ratio when we focus on indivisual quasar.
- Reported CLQs are expected to repeat state transition.

Chapter 4

Probing the origin of broad line region by reverberation mapping and multi-wavelength observations of an extremely variable quasar

This chapter is to be submitted

4.1 Introduction to Chapter 4

To understand the structure and kinematics of the BLR in detail, consideration of its origin is important. There are two major hypothesis for the origin of the BLR gas. One is the disk-wind from accretion disks (e.g., Czerny & Hryniewicz 2011) and the other is the inflow (including tidally disrupted cramps) from the dust torus (e.g., Gaskell 2009). If the gas is supplied by the disk wind from the accretion disk, it is expected that the amount of disk wind changes with the mass accretion rate of the accretion disk, resulting in a variation in the broad line intensity (Elitzur et al. 2014). Some studies have suggested that tidally disrupted dust torus gas is responsible for the asymmetric component of the broad line (Wang et al. 2017). As the observational results are different from object to object, the origin of the BLR is still under debate. For example, the velocity resolved RM results showed that some objects exhibited outflow features (e.g., Lu et al. 2019, 2021) while some exhibited inflow features (e.g., Gaskell 1988; Koratkar & Gaskell 1989; Denney et al. 2010;

Grier et al. 2013b; Du et al. 2016; Zhang et al. 2019; Lu et al. 2021; Bao et al. 2022), or both (e.g., Du et al. 2018a; Brotherton et al. 2020; Lu et al. 2021). A possible scenario is that multiple origins may be mixed. The key is, we believe, to sort out what could exist as an origin and to what extent it is dominant.

We suggested in Nagoshi & Iwamuro (2022) that an ideal target for investigating the origin of the BLR is Changing-State (Look) Quasars. We focus on the variability of broad line and continuum luminosity., which show significant variations ($> 30\%$) in the broad lines and in mid-infrared luminosity (LaMassa et al. 2015; MacLeod et al. 2016, 2019; Ruan et al. 2016; Gezari et al. 2017; Wang et al. 2018; Noda & Done 2018; Ross et al. 2020; Graham et al. 2020; Nagoshi et al. 2021; Wada et al. 2021; Green et al. 2022). This significant variation represents the structural transformation process, which is an ideal feature for investigating each component of the unified model of AGN. In particular, if we can observe the emergence process of the BLR, we can place restrictions on the origin of the BLR gas. The variation process of accretion disks also provides essential information since quasars have long timescales of variation and have been poorly studied observationally. Therefore, the purpose of this study is to apply RM to one of the CSQs (Dexter et al. 2019; Li et al. 2022) together with X-ray observations to gain insight into the physical origin of the BLR and the physical process of drastic variation in the accretion disk.

In our previous work, Nagoshi et al. 2021, SDSS J125809.31+351943.0 (hereafter J1258; $z = 0.30939$) was discovered as an ideal target for RM study. It is the object that experienced the most significant state transition in history (optical brightness variation of about 4 magnitudes in about 30 years). The significant brightness variation is expected to have a large signal-to-noise ratio of the varied component in the spectrum, making it a suitable target for RM. The selection procedure for this object is described in detail in Nagoshi et al. (2021).

Each section is organized as follows. Section 4.2 describes our observations and the archival data we used. Section 4.3 describes the results of the RM analysis and the comparison of SED before and after the extreme variation. Section 4.4 discusses the cause of the variation and quasar structure based on the above results. The cosmological parameters are assumed to be $H_0 = 70$ kms^{-1}Mpc^{-1}, $\Omega_M = 0.3$ and $\Omega_\Delta = 0.7$ based on the ΛCDM cosmology throughout this paper. All errors that appear in this paper represent 1σ errors.

4.2 Data

This section explains the data we used. Firstly, we describe the optical/mid-infrared photometry data, which mainly correspond to the continuum emission from accretion disk / dust torus, respectively. Secondly, the spectroscopic data mainly used to derive the light curve of Hβ are explained. Finally, we describe the X-ray observations used to investigate the accretion state of the inner part of accretion disk.

4.2.1 Optical Photometry

We included archival data of photometric observations, because the cadence of spectral observations in this study is insufficient to measure time-lag. The catalog data used were the Catalina Real-time Transient Survey (CRTS; Drake et al. (2009)) and the All Sky Survey Automated Survey for Super-Nova (ASAS-SN; Kochanek et al. (2017)). CRTS is unfiltered photometric data, while ASAS-SN observations mainly use g-band and V-band filters. Observations between different filters show consistent patterns of light curves, but a certain amount of offset exists. Therefore, an offset was applied to match the mean values in the overlapping period of the two light curves. Detailed analysis is described in Nagoshi et al. (2021). The essential information to measure the time-lag is the patterns of brightness variation. Therefore, we treat the combined light curve as a continuum light curve of J1258 in this analysis, though it contains values of different filters.

4.2.2 Mid Infrared (WISE) photometry

The Wide-field Infrared Survey Explorer (WISE; Wright et al. (2010)), which is a mid-infrared satellite launched in December 2009 and observed the entire sky in four bands (3.4, 4.6, 12, and 22 μm), also observed J1258. WISE operations were temporarily terminated in February 2011, but observations resumed in December 2013 as the NEOWISE project (Mainzer et al. 2014). NEOWISE has two bands of 3.4 and 4.6 μm and observed the entire sky, visiting each area in the sky about ten times every six months.

As the information of J1258, we referred to the single-exposure profile-fit magnitude within 3" from RA = 12:58:09.31 and DEC = +35:19:43.03. From these values, we selected those with no contamination and confusion flag ("cc_flags" = 0000). In the present analysis, we used the combined data with each bin accumulated for six months period, sufficient for the variation timescale of our interest.

4.2.3 Spectroscopy 1: Sloan Digital Sky Survey

J1258 has been spectroscopically observed twice by the SDSS, in April 2006 and April 2016. The SDSS (York et al. (2000)) is based on a photometric survey using a 2.5-m wide-field telescope (Gunn et al. (2006)) equipped with 30 2k $\times$ 2k CCDs and following spectroscopic observations. Between the two observations, the spectroscopic instrument was upgraded, the wavelength range was extended and the thickness of the fiber on the SDSS plate was changed from $3''$ to $2''$ with the upgrade of the spectrograph.

4.2.4 Spectroscopy 2: LAMOST

J1258 was observed on April 2017, by the Large Sky Area Multi-Object Fiber Spectroscopic Telescope (LAMOST; Cui et al. (2012); Zhao et al. (2012)), a Schmidt telescope with a primary mirror size of 6.67m $\times$ 6.05m. The wavelength ranges from 370 nm to 900 nm, and the wavelength resolution is about 1000. The data is reduced with LAMOST pipelines (Luo et al. 2015).

4.2.5 Spectroscopy 3: MALLS

We performed two spectroscopic observations in December 2018, and May 2019 with the slit spectrograph called "MALLS" (Medium And Low-dispersion Long-slit Spectrograph) installed in the 2-meter telescope in Nishi Harima Astronomical Observatory in Japan. The grating was 150 /mm, giving a spectral resolution of ~ 600, with the $1\farcs2$ slit width We executed five 1200-second exposures for two nights. The observed data were reduced with the standard processing of slit spectroscopy with IRAF (dark subtraction, flat correction, matching sky subtraction, wavelength correction, and flux correction using the spectrophotometric standard).

4.2.6 Spectroscopy 4: KOOLS-IFU

We performed spectroscopic monitoring observation in 2020 using the low-resolution spectroscopic data from KOOLS-IFU (Kyoto Okayama Optical Low-dispersion Spectrograph with optical-fiber Integral Field Unit; Matsubayashi et al. 2019) installed in the 3.8-m Seimei Telescope (Kurita et al. 2020) at Okayama Observatory

of Kyoto University. The data are reduced with KOOLS-IFU pipeline[1].

4.2.7 X-ray

The target was observed twice using the ROSAT (Truemper 1982) Position Sensitive Proportional Counter (PSPC) detector in 1991 December (ObsID = RP600164N00) and 1992 December (RP701178N00) with net exposures of 16.2 ks and 3.9 ks, respectively. The ROSAT data were processed with Standard Analysis Software System (SASS). The source spectra were extracted from a circular region with a radius of 150″ centered on the source by using XSELECT. The background spectra were selected from a partial annulus region with inner and outer radii of 225″ and 450″ by excluding the region of a nearby X-ray source (1RXS J125740.2+351334; Voges et al. 1999). We used the standard response matrix ('pspcb_gain2_256.rsp') and generated the ancillary response files using pcarf command in HEASOFT v6.25.

We also used the data of Swift/X-Ray Telescope (XRT; Burrows et al. 2005) in 2021 February (ObsID = 14079001) with a net exposure of 1.9 ks, covering the ∼0.3–10 keV band. The data reduction was performed with the XRTPIPELINE v0.13.4. The source spectrum was taken from a circular region of 45″ radius, while the background was from an annulus between 90″and 150″ radii.

4.3 Analysis and Result

In this section, we explain the analysis of optical spectra to investigate the variation of Hβ. Then, we measured the time-lag of Hβ, $W1$, and $W2$ to the continuum.

4.3.1 Variation of Hβ

To obtain accurate light curves, we calibrated the spectral flux assuming [OIII]5007 luminosity does not change during all observations. We fitted the spectra to determine their [OIII]5007 flux with PyQSOfit (Guo et al. 2018). The components applied in the fitting are a power-law continuum, three Gaussian components for the broad Hβ, and one Gaussian each for the narrow Hβ, [OIII]4959/5007. First, the continuum is fitted with power-law using the window of 4450-4500 Å and

[1]We used the pipeline here `http://www.kusastro.kyoto-u.ac.jp/~iwamuro/KOOLS/index.html`

5150-5250 Å in the rest frame, and then the continuum component is subtracted from the spectrum. We use these continuum-subtracted spectra to fit the emission lines. The velocity offsets and the line width for [OIII]4959/5007, and the narrow Hβ are set to be equal, and the flux ratio was fixed to 1:3:0.07 (The ratio of the narrow component of Hβ was obtained by fitting the first SDSS spectrum, MJD 53848, with free parameters. We fixed the ratio of the narrow emission lines to this value in the fitting of the other spectra). After the fitting, we normalize all flux density using the flux of [OIII]5007 calculated with the Gaussian fitting. The total Hβ flux is measured by simply integrating the subtracted spectra in 4611-5111 Å after the flux normalization. Each measurement error was estimated using the Monte Carlo method, which consists of 100 fitting calculations repeated with random noise based on the error of the spectrum. The value of the light curve of Hβ is summarized in Table 4.6 and Figure 4.12.

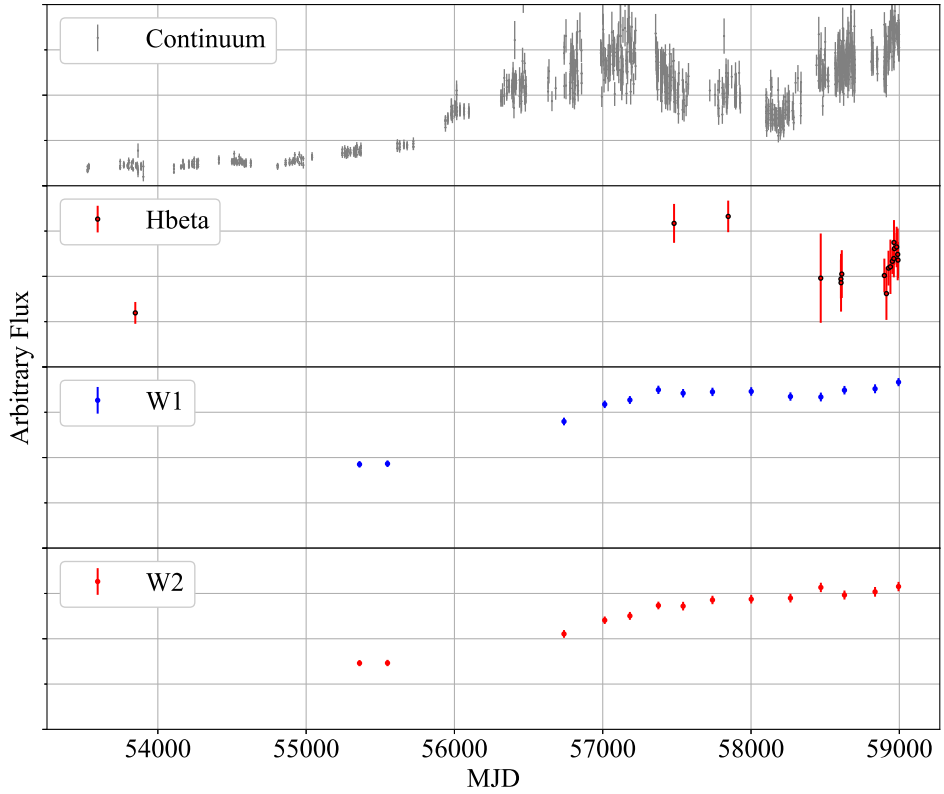

Figure 4.1: The light curves of continuum (top), Hβ (the second), WISE $W1$ (the third), and WISE $W2$ (bottom) of J1258.

We also calculated the mean spectrum and root mean square residual spectrum (RMS spectrum) to visualize the typical shape of the emission line and variable component (Peterson et al. 2004). Because of the non-uniform time periods between observations, the calculation is weighted by the length of the observation period as a percentage of the light curve. The definition formula is as follows (here, f represents each spectrum, t represents the date of each observation, and the numbers in the subscripts indicate the order of each spectrum by date of observation):

$$f_{\mathrm{mean}} = \frac{1}{2(t_N - t_1)}\Big(f_1(t_2 - t_1) + f_N(t_N - t_{N-1}) + \sum_{i=2}^{N-1} f_i(t_{i+1} - t_{i-1})\Big) \tag{4.1}$$

$$f_{\mathrm{RMS}} = \left(\frac{1}{2(t_N - t_1)}\Big((f_1 - f_{\mathrm{mean}})^2(t_2 - t_1) + (f_N - f_{\mathrm{mean}})^2(t_N - t_{N-1}) + \sum_{i=2}^{N-1}(f_i - f_{\mathrm{mean}})^2(t_{i+1} - t_{i-1})\Big)\right)^{\frac{1}{2}} \tag{4.2}$$

The mean and RMS spectra for J1258 are shown in Figure 4.2. The mean spectrum represents the typical shape of the Hβ and [OIII]4959/5007, while the RMS spectrum represents how variable each wavelength component in the lines is. One of the characteristics of the mean spectrum is asymmetry (the bluer side is stronger), but the RMS spectrum seems symmetric. The RMS spectrum shows that [OIII]4959/5007 profiles are little variable, which indicates that the flux normalization using [OIII]5007 is working well.

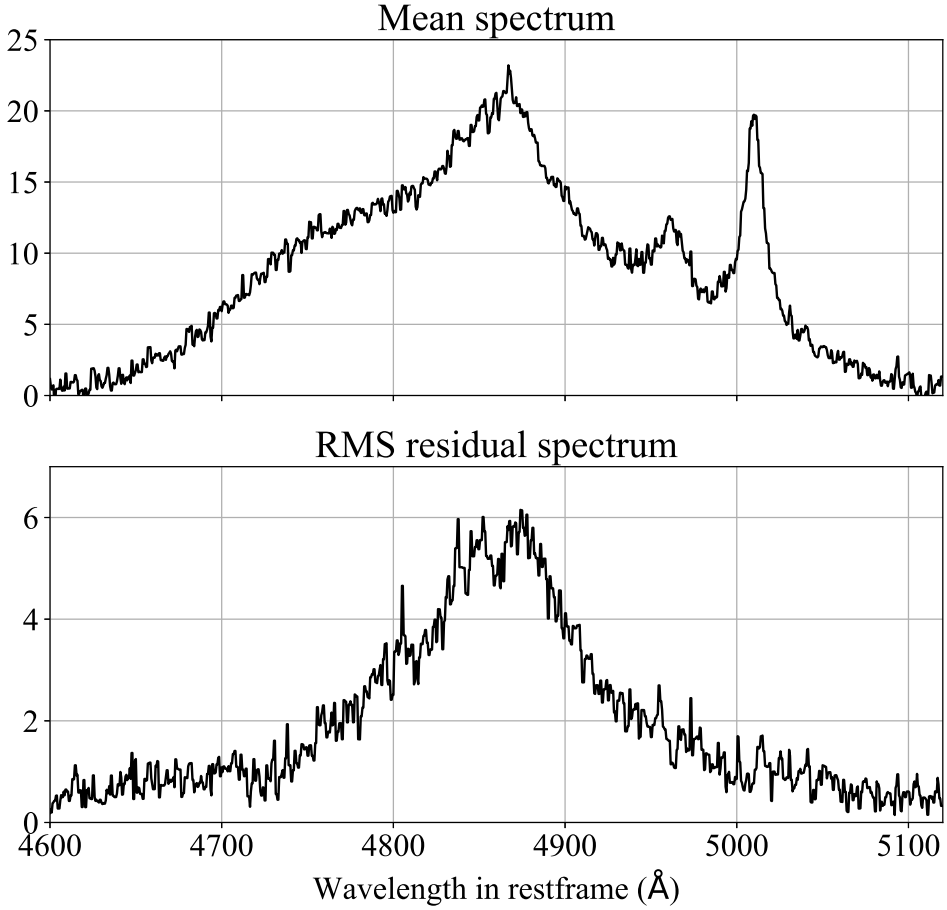

Figure 4.2: Mean (top) and RMS (bottom) spectra of J1258. The RMS spectrum shows clearly the broad and symmetric Hβ. The narrow [OIII]4959/5007 lines and asymmetric double peaked component of broad Hβ
appear only in the mean spectrum, except for weak residuals.

4.3.2 Time-lag measurement

We calculate the time-lag from the continuum light curve for Hβ, WISE $W1$, and WISE $W2$, respectively. To obtain time-lags, we compared the results using two different software algorithms: interpolated cross-correlation function (ICCF) (Sun et al. 2018; Peterson 1998), and JAVELIN (Zu et al. 2010, 2011; Zu & Weinberg 2013).

ICCF calculates the cross-correlation function with two linearly interpolated

light curves. The time-lag and its error are determined by the Monte Carlo method; it calculates the cross-correlation function 10,000 times with light curves of different values within error bars, resulting in the distribution of the correlation peak.

On the other hand, JAVELIN assumes a primary light curve to follow the dumped random walk (DRW) process (e.g., Kelly et al. 2009) and convolves it with a top-hat transfer function (TF) to make a responding light curve, searching with the Markov chain Monte Carlo method for the most likely values for the following five parameters: the amplitude and time-scale of the DRW process, height and width of the top-hat TF, and response time delay.

The results of time-lag measurements are summarized in Table 4.1, Figure **??**.

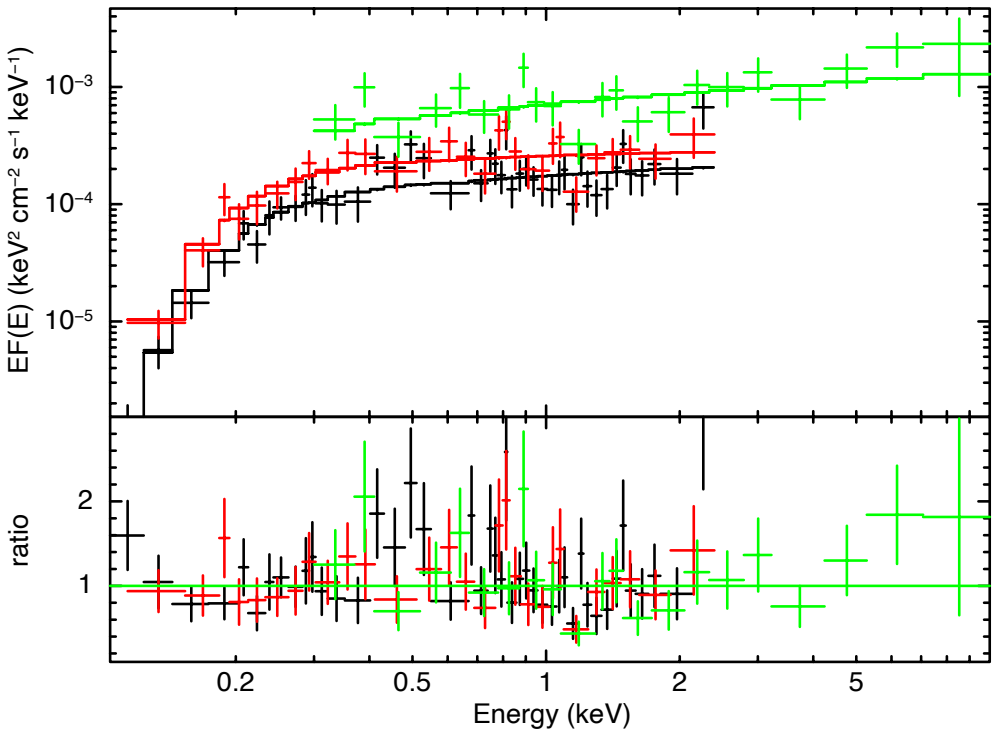

Figure 4.5: The unfolded X-ray spectra and best-fit models of the observations with ROSAT in 1991 (black), 1992 (red), and Swift/XRT in 2021 (green). The bottom panel shows the ratios between the data and models.

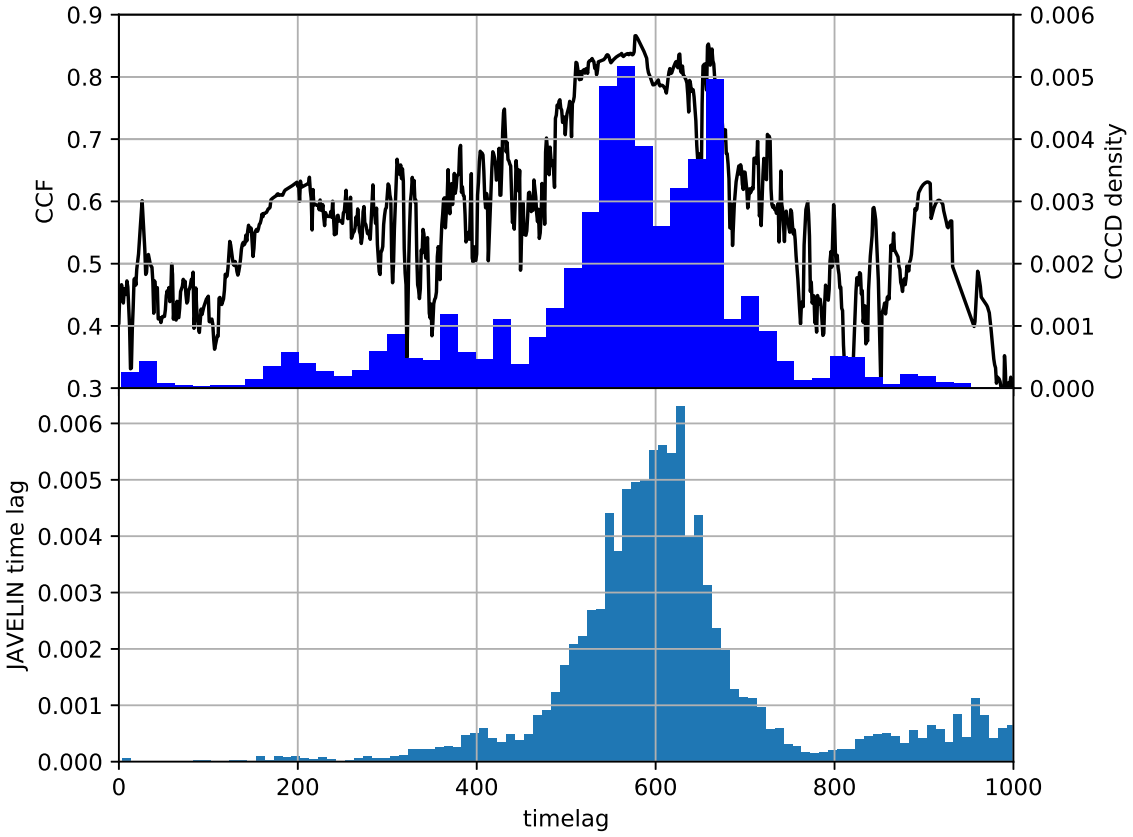

Figure 4.3: The Cross-Correlation Function and the centroid distribution to the continuum with Hβ of J1258.

Table 4.1:: Rest-frame reverberation lags based on ICCF and JAVELIN analysis

Time-lag target	$\tau_{\rm rest}$(ICCF)	$\tau_{\rm rest}$(JAVELIN)
Hβ	439^{+64}_{-75}	470^{+84}_{-51}
$W1$	805^{+144}_{-116}	735^{16}_{-291}
$W2$	1002^{+68}_{-77}	913^{36}_{-28}

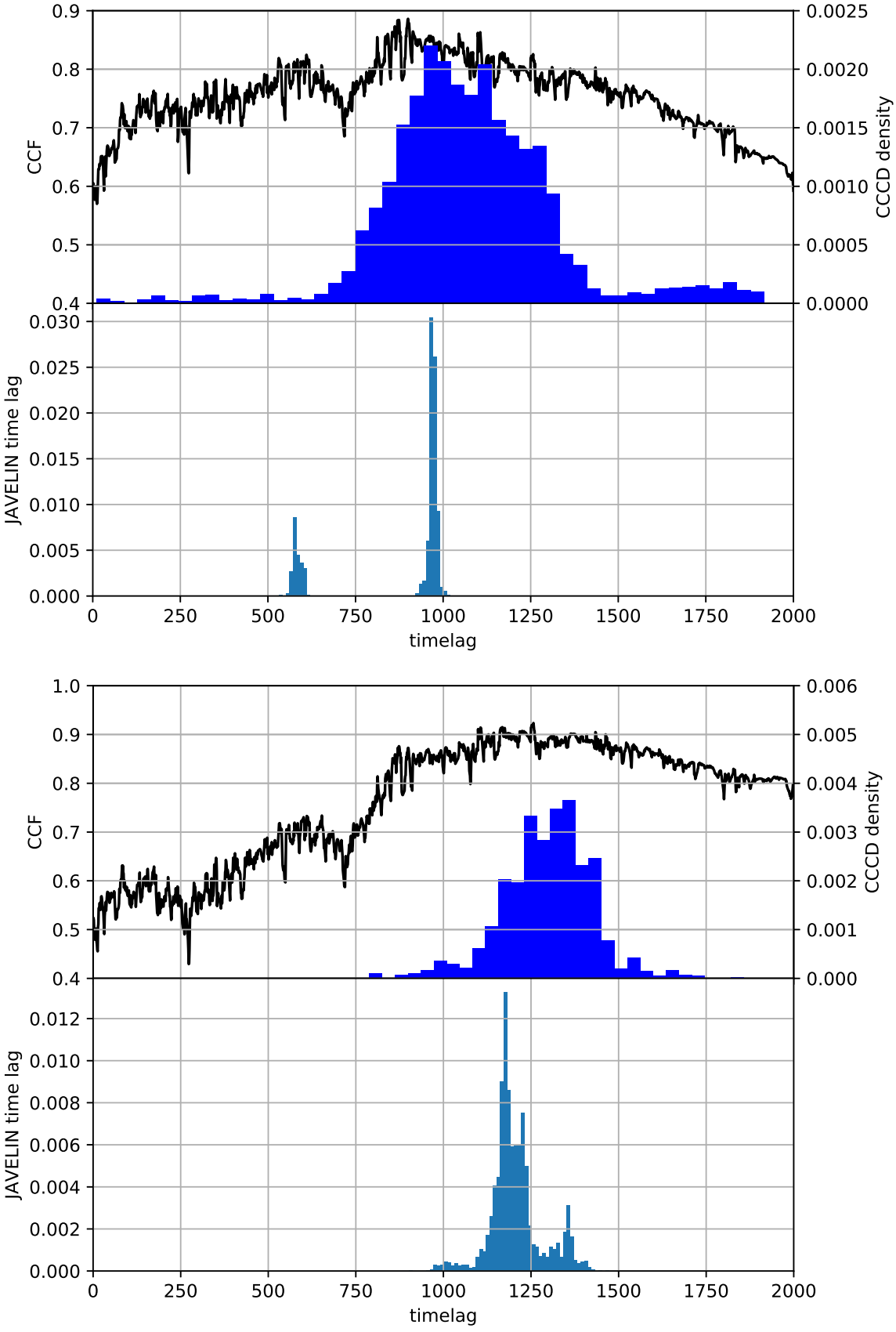

Figure 4.4: The Cross-Correlation Function and the centroid distribution to the continuum with WISE $W1$ (top) and WISE $W2$ (bottom) of J1258.

4.4 Discussion

In this section, we first estimate the black hole mass. Secondly, we discuss the mechanism of the extreme brightening event of J1258. Finally, based on a review of the information obtained in this study, we discuss the structure and the origin of the BLR as found by CSQ RM.

4.4.1 Black Hole Mass Estimation

We calculate the black hole mass using the line width ($\Delta V \equiv \sigma_{\rm line}$) and the time-lag ($\tau$) with Equation 1.1. The f factor depends on the structure and kinematics of the BLR. Here, we adopt the value of $f = 4.3$ calculated by Grier et al. (2013a), and the time-lag of ICCF. The line width of Hβ is calculated with the RMS spectrum because the time-lag represents the varied component. Here, the RMS spectrum contains a component due to observation noise independent of the actual emission line intensity variations. To estimate the effect of observation noise, we fitted the RMS spectra with a single Gaussian and a constant, assuming that the wavelength dependence of the noise is weak and constant. We then interpret the spectrum obtained by subtracting the constant as the variable component. The line width is $\sigma = 3192 \pm 372$ km/s. We adopt the ICCF values for the time-lag ($\tau_{\rm H\beta} = 439^{+64}_{-75}$ days; $c\tau \sim 0.37$pc). As a result, the measured $M_{\rm BH}$ is $10^{9.46^{+0.15}_{-0.19}}{\rm M}_\odot$.

4.4.2 Mechanism of the extreme variability

In general, the leading cause of the CSQ is considered to be intrinsic variability in the mass accretion rate of the disk for the following reasons. First, the variability timescale of broad emission lines and continuum light is short. Second, the reddening in optical (e.g., MacLeod et al. 2016) and the X-ray hydrogen column density (Husemann et al. 2016) did not change before and after the state transition. Third, the brightness in the mid-IR changed in response to continuum emission (Stern et al. 2018; Nagoshi et al. 2021). Finally, polarization was not detected in spectropolarimetry (Hutsemékers et al. 2017, 2019). All of the above results support that CSQs are not explained by any shielding theories, but consistent with the intrinsic variation of mass accretion rate.

In Nagoshi et al. (2021), we proposed that the J1258's brightening event was caused by a state transition in the accretion disk, based on the timescale argument. In order to confirm the hypothesis, we performed spectroscopic monitoring and

X-ray observations to estimate the optical-to-X-ray slope ($\alpha_{\rm ox}$).

$\alpha_{\rm ox}$ and Eddington ratio

We analyzed the X-ray spectra of the ROSAT and Swift/XRT data with XSPEC v12.10.1 (Arnaud 1996). We consider Galactic absorption by the phabs model and refer the hydrogen column density fixed at the value of Willingale et al. (2013). Abundances were assumed at solar values. Cash statistics (Cash 1979) were utilized to fit ROSAT (0.1–2.4 keV) and Swift (0.3–10 keV) spectra, and the spectra were binned to have one count per bin. The spectra were well reproduced by a single power law model (zpowerlw) with Galactic absorption, as shown in Figure 4.5. The best-fitting parameters with the 90% uncertainties, observed-frame 2 keV ($\nu{\rm F}_{\rm 2keV}$) and 2–10 keV ($\nu{\rm F}_{\rm 2-10keV}$) fluxes, and rest-frame 2 keV ($\nu{\rm L}_{\rm 2keV}$) and 2–10 keV ($\nu{\rm L}_{\rm 2-10keV}$) luminosities[2], all of which are corrected for Galactic absorption, are presented in Table 4.2. The photon indices are $\sim$1.7–1.9, consistent with a typical value in AGNs (e.g., Ueda et al. 2014; Ricci et al. 2017). We find that the rest-frame 2 keV luminosities increase from $\sim 1\times10^{44}$ erg/s in 1991 and 1992 to $\sim 4\times10^{44}$ erg/s in 2021.

We compare the Eddington ratio and $\alpha_{\rm ox}$ of before and after the state transition with the similar method of Jin et al. (2021). $\alpha_{\rm ox}$ is a spectral index between optical and X-ray characterizing the state of accretion disk. We use the following definition

[2]The uncertainties of $\nu{\rm F}_{\rm 2keV}$ and $\nu{\rm L}_{\rm 2keV}$ are obtained by the cflux and clumin models in XSPEC. The uncertainties of the 2–10 keV fluxes and luminosities are assumed to the log-scale uncertainties at the 2 keV band.

Table 4.2:: Best-fit X-ray spectral parameters, observed-frame absorption-corrected fluxes, rest-frame luminosities, and reduced C statistics

Parameters	ROSAT (1991)	ROSAT (1992)	Swift (2021)
Photon Index	$1.82^{+0.10}_{-0.09}$	$1.94^{+0.12}_{-0.13}$	$1.73^{+0.17}_{-0.16}$
Norm [10^{-4}]	$2.9^{+0.2}_{-0.2}$	$4.5^{+0.5}_{-0.5}$	$11.6^{+1.8}_{-1.6}$
$\nu{\rm F}_{\rm 2keV}$ [10^{-13} erg/s/cm^2]	$3.25^{+0.49}_{-0.44}$	$4.45^{+0.91}_{-0.79}$	$14.02^{+1.96}_{-1.83}$
$\nu{\rm F}_{\rm 2-10keV}$ [10^{-13} erg/s/cm^2]	$6.05^{+0.91}_{-0.83}$	$7.53^{+1.54}_{-1.33}$	$28.20^{+3.95}_{-3.67}$
$\nu{\rm L}_{\rm 2keV}$ [10^{44} erg/s]	$0.96^{+0.15}_{-0.13}$	$1.36^{+0.28}_{-0.24}$	$4.08^{+0.57}_{-0.53}$
$\nu{\rm L}_{\rm 2-10keV}$ [10^{44} erg/s]	$1.81^{+0.27}_{-0.25}$	$2.32^{+0.48}_{-0.41}$	$8.24^{+1.15}_{-1.08}$
C/C$_\nu$	166.8/174	147.2/140	147.8/192

to calculate α_{ox} (Tananbaum et al. 1979),

$$\alpha_{ox} = -\frac{\log(\lambda L_{2500Å}) - \log(\nu L_{2keV})}{\log\nu_{2500Å} - \log\nu_{2keV}} + 1 \tag{4.3}$$

in which the continuum luminosity at 2500 Å is estimated by extrapolation of the fitted power-law component. For spectral fitting, the power-law component, FeII template, and Balmer continuum component were applied to 4450-4500 and 5150-5250 Å avoiding narrow emission lines and Broad Lines. The errors were estimated by Monte Carlo simulation. The bolometric luminosity is estimated using the Lusso et al. (2010) correction formula.

$$\log(L_{bol}) = \log(\nu L_{2-10keV}) + 15.61 - 1.853\alpha_{ox} + 1.226\alpha_{ox}^2 \tag{4.4}$$

The α_{ox}, bolometric luminosity, and Eddington's ratio before and after the state transitions, obtained from the above results, are summarized in Table 4.3.

We used optical spectra and X-ray data taken during dim and bright states each. Since the optical light curve in Figure 4.6 shows that the state transition happened in 2003 (MJD around 54,000) to 2015 (MJD around 57,000), we consider the status before 2003 as a dim state, while the status after 2015 as a bright state.

Table 4.3:: This is an example table. Captions appear above each table. Remember to define the quantities, symbols and units used. Add errors to all parameters

Parameters	Dim State	Bright State
Bolometric Luminosity	45.3 ± 0.18	46.1 ± 0.21
Eddington Ratio	0.006 ± 0.013	0.037 ± 0.079
α_{ox}	1.02 ± 0.07	1.29 ± 0.05
PL slope	-0.894 ± 0.049	-1.643 ± 0.003
PL Norm	21.46 ± 0.68	208.72 ± 0.36
$\log(\lambda L_{2500Å})$	44.289 ± 0.010	45.337 ± 0.001

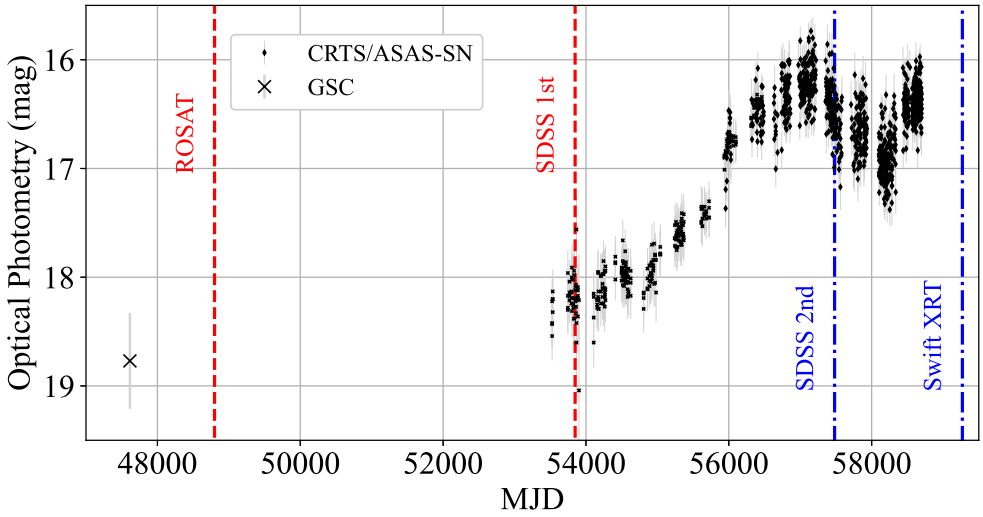

Figure 4.6: The optical light curve with periods of optical spectra and X-ray observation. The black dots represent the optical light curve, and the vertical lines drawn with dotted lines represent the time of spectral or X-ray observations. The data before MJD = 54,000 are considered as Dim State, and the data after MJD = 57,000 as Bright State.

Jin et al. (2021) compared the α_{ox} of the CLQs with the values of the simulation in X-ray binary extended to AGN, then confirmed that it is consistent with the prediction of the state transition model. Jin et al. (2021) confirmed the negative correlation between Eddington ratio and α_{ox} for the objects with low (¡ 0.01) Eddington ratio, while Lusso et al. (2010) confirmed the positive correlation for the objects with high (¿ 0.01) Eddington ratio.

Accretion rate variation

The measured Eddington ratio and α_{ox} of J1258 in the dim and bright state each are consistent with the state transition model suggested in the previous research (Noda & Done 2018). We show the comparison of the Eddington ratio and α_{ox} on Figure 4.7 together with the best fit result of Jin et al. (2021) and Lusso et al. (2010).

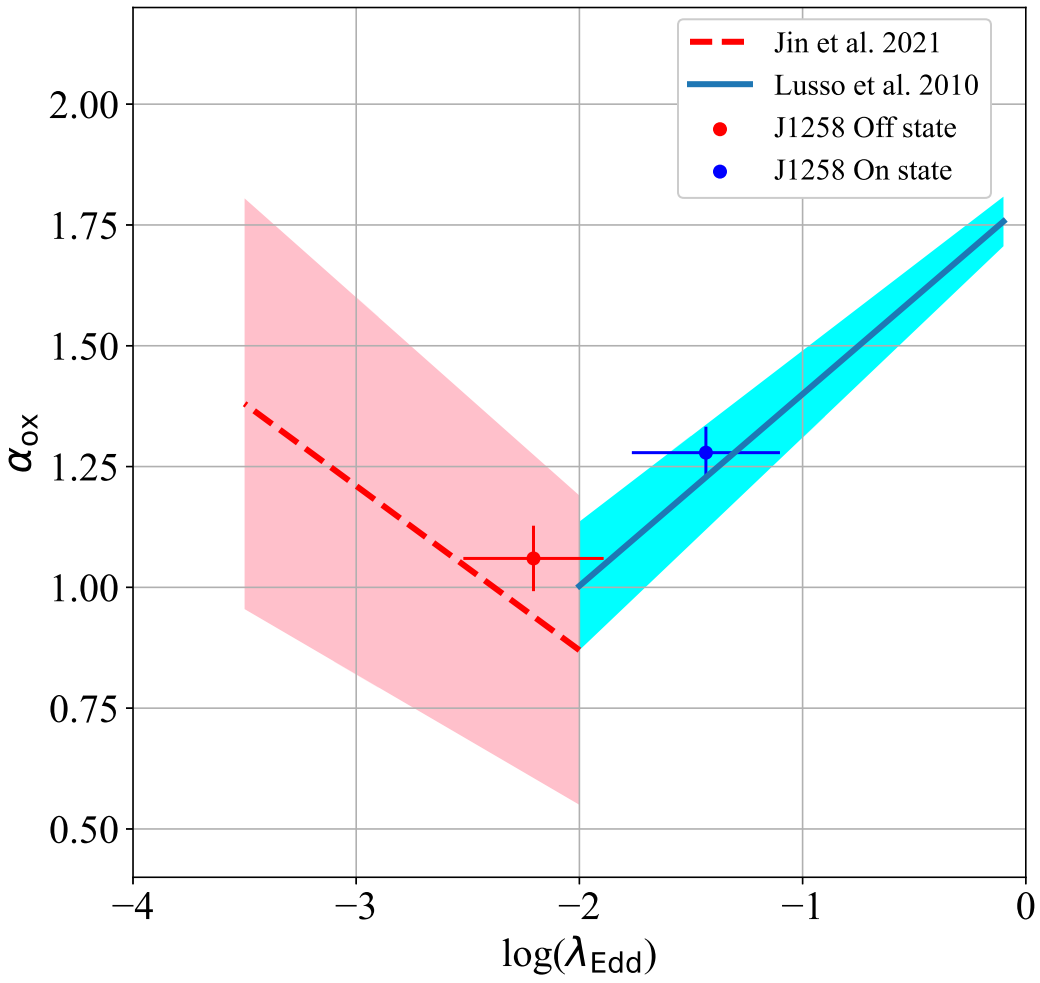

Figure 4.7: Measured α_{ox} and λ_{Edd} of J1258 when it is On and Off state. The red dashed line displays the fitting result of dim state of quasars and Changing-Look Quasars (Jin et al. 2021). The blue solid line represents the α_{ox} - λ_{Edd} relation of bright state derived from the XMM-COSMOS survey (Lusso et al. 2010)

A possible cause of the state transition is thermal disk instability. According to the disk instability model, the accretion disk forms a geometrically thin disk at high Eddington ratios (Shakura & Sunyaev 1973) characterized by soft excess in X-ray, whose accretion state is called the high/soft state. During the low Eddington ratio, the inner region of the thin disk is evaporating (Esin et al. 1997), resulting in a hot and radiatively inefficient accretion flow (Shapiro et al. 1976), possibly advection

dominated (Narayan & Yi 1994). In this state, the X-ray spectrum is dominated by Compton scattering of hard X-rays originating from the accretion flow, called the low/hard state. The spectral index from optical to soft X-ray component, α_{ox}, is used to characterize these spectral states. The correlation between α_{ox} and the Eddington ratio is predicted theoretically to change according to certain rules (negatively correlated to the Eddington ratio during low/hard state, while positively correlated during high/soft state) during the state transition, and has been confirmed observationally in X-ray binaries.

Another possibility is that the state transition was triggered by external factors such as the tidal disruption of a star (Merloni et al. 2015). The outburst caused by TDEs is expected to show a decline in flux with $t^{-5/3}$ (van Velzen et al. 2020). In the case of J1258, however, it shows brightening again from around MJD = 58,000 (Figure 4.12), which is inconsistent with the expected patterns of the light curve of TDEs.

One possibility that is quite different from the previous discussions is the theory that J1258 is a close SMBH binary. Asymmetric broad lines are often referred to as one of the characteristics of binary SMBHs (Eracleous et al. 2012; Runnoe et al. 2015). That is a situation where two SMBHs each form an AGN with their own the BLRs. Given this situation, if a state transition occurs in one of the AGNs and the brightness varies significantly, there is no need for occurring in the other AGN. Furthermore, if the interaction of the two SMBHs efficiently extracted angular momentum, it could be considered a trigger for the large-scale brightening event (Wang & Bon 2020). To confirm the hypothesis, testing whether the velocity shift in the asymmetric component of the broad lines is changing according to the orbital motion would be helpful. However, it is not easy to calculate the velocity shift of broad emission lines with independently varying intensities because the quality of the obtained spectra in this study is not high enough. If a velocity shift were to present, it would be valid to compare the spectra again after sufficient time has passed, which could be verified in future studies.

In short, based on the results, the main cause of the J1258 brightening event is a change of the intrinsic accretion power caused by the state transition of the accretion disk, as we mentioned in Nagoshi et al. (2021).

4.4.3 Structure of the BLR

We discuss the structure and origin of the BLR using the extreme variation of the broad line of J1258. The mean and RMS spectra in Figure 4.2 show the typical

emission line shape and the variable component, respectively (Peterson et al. 2004). Examining Figure 4.2, it can be noticed that the shapes of the mean and RMS spectra are very different, even if the narrow emission line component is subtracted. To visualize the difference between the two, how emission line shape changes if the variable component changes more is shown in Figure 4.8. Here, we interpret that the RMS spectrum is a variable component, and we assume that the component changes simultaneously in all velocities. The spectrum on the top of Figure 4.8 represents the mean spectrum. The second spectrum from the top is the mean spectrum subtracted from the narrow lines (the narrow components in Hβ and [OIII]4959/5007). The third and fourth spectra from the top represent how we can see the shape of Hβ if the variable component (the RMS) changes -1 or -3 times each. We can see that the spectral shape at the bottom of Figure 4.8 shows a double-peaked shape. On the other hand, the RMS spectrum has a generally symmetrical, single-peaked shape. These represent that the spectra typically have a double-peaked component, but the single-peaked component changes with continuum variation, indicating that there are two distinct regions in the BLR (Hu et al. 2020).

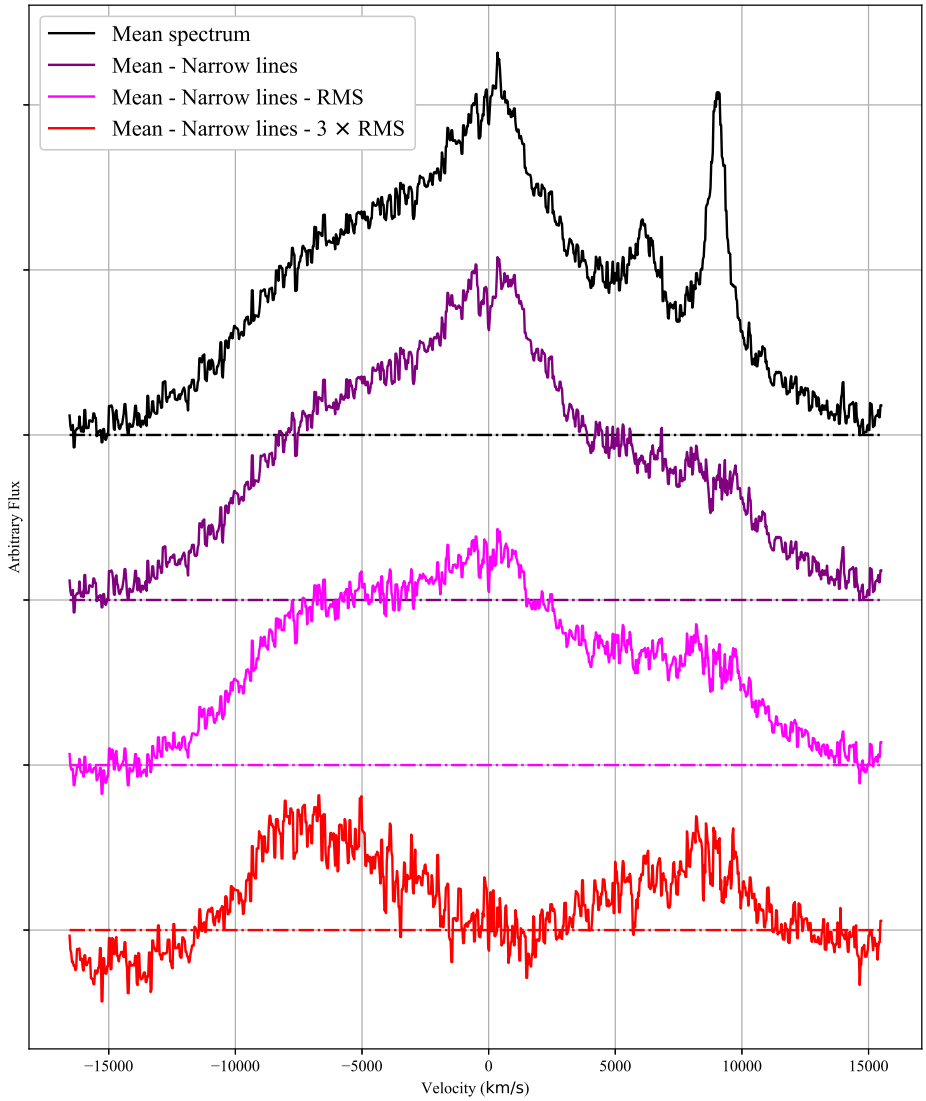

Figure 4.8: Diagram visualizing the double-peaked component on the broad line. The top spectrum is the mean spectrum, the second from the top is the mean spectrum minus the narrow emission line, and the third is the second spectrum minus the RMS spectrum. The bottom spectrum is the mean spectrum minus three times the RMS spectrum. The baseline of each spectrum has been added to a constant for clarity.

Based on the above spectral components, the BLR of J1258 is expected to consist of two different regions emitting a single-peaked component (RMS spectrum) and a double-peaked fast component (the bottom spectrum in Figure 7), respectively. Here we name these components Region X and Region Y, respectively:

Region X: Emitting a relatively slow, single-peaked line that responds to the state transition of the accretion disk.

Region Y: Emitting a fast, double-peaked line, which is not likely affected by the state transition of the accretion disk.

Region X has the same characteristics as the BLR seen in a typical quasar, whose size can be estimated from the measured time-lag of the reverberation observation. the BLR size of Region X was found to be 0.37 pc from the center (Section 4.3).

The kinematics to produce the double-peaked emission lines emitted from Region Y could be fast outflow, fast inflow, or rotating ring-like structures. Among these, the strong outflow and inflow are expected to be affected by the mass accretion rate (e.g., Elitzur et al. 2014), but the double-peaked component did not show any significant variation associated with the state transition (Figure 4.2). Therefore, the the double-peaked broad Hβ is likely to generated passively as a rotating disk (Eracleous & Halpern 1994, 2003).

With the above points taken into account, it is possible to combine them into a single figure without any geometrical inconsistency. The distance to Region X can be determined from the time-lag, which is about 0.37 pc. The distance to Region Y is about 0.25pc $\sim 1800 R_g (\equiv \frac{GM}{c^2})$, which can be explained by the rotation of the disk, given that the black hole mass is $10^{9.46} M_\odot$ and the typical speed is about 7,000 km/s (the peak velocity of the double-peaked component). If the asymmetric shape is caused by a bias in the distribution of ionized gas in Region Y, the period over which the gas makes one cycle is about 200 years. Therefore, detecting a velocity shift over a 20-year observation period would be difficult. The distance to the dust torus is estimated by the response time of $W1$ to be 0.7 pc. These locations are shown in Figure 4.9.

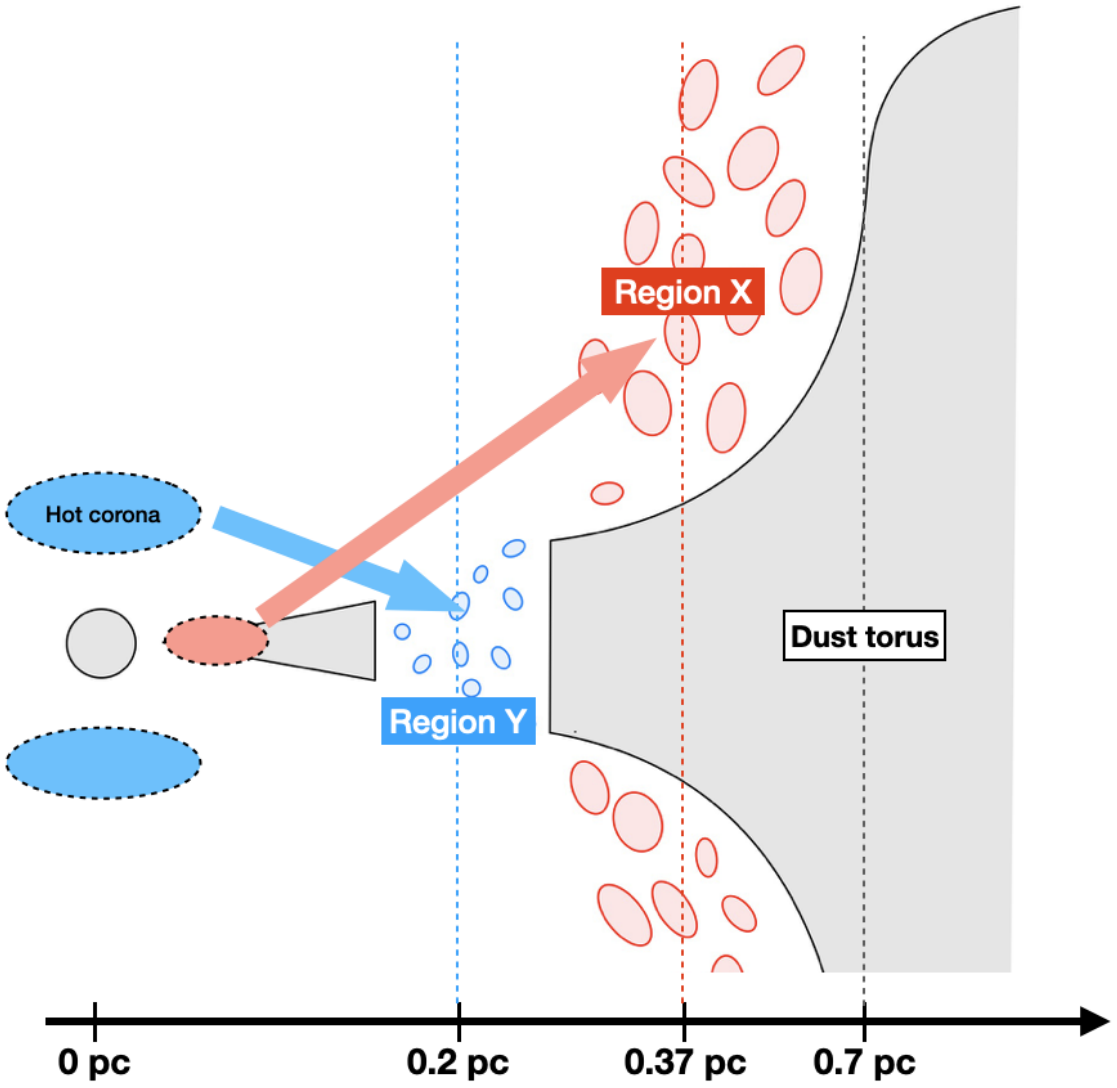

Figure 4.9: Conceptual view of the central core structure of J1258 inferred from the time-lag and wavelength shift. The distance to Region X and the black hole mass are estimated from the Hβ time-lag. The distance to Region Y is estimated from the determined black hole mass, and the distance to the dust torus is estimated from the WISE $W1$ time-lag.

Assuming the structure of Figure 4.9, it is also possible to explain why Region Y was not affected by the state transition of the accretion disk. The brightening phenomenon due to the state transition from the low/hard state to the high/soft state is caused by the variation of soft X-rays from the inner part of the accretion disk being larger than that of hard X-rays from the hot corona ($T \sim 10^9$K) region (Noda & Done 2018). That is, the intensity of the hard X-ray itself does not change

much before and after the state transition, which is also confirmed observationally (e.g., Mathur et al. 2018). If we assume that Region Y is located right next to the disk so that only the axially extended hot corona region can supply ionizing photons to Region Y, this is a possible explanation for why the intensity of the emission lines emitted from Region Y is less affected by the state transition.

4.4.4 Origin of the BLR

Based on the structure shown in Figure 4.9, we discuss the origins of the gas in the BLR from two major theories: one is that the gas is supplied from disk winds from accretion disks (e.g., Gaskell 1982; Nicastro 2000; Nicastro et al. 2003; Czerny & Hryniewicz 2011) and the other is that it is derived from accreted components from the dust torus (e.g., Gaskell 2009, 2010; Hopkins et al. 2012; Gaskell & Goosmann 2013; Wang et al. 2017). The disk-wind origin theory is based on a model in which outflow generated from the accretion disk according to an increase of the mass accretion rate winds up the gas, which is ionized by the emission from the inner accretion disk. This model suggests that no the BLR is produced below a certain threshold because the disk wind depends on the mass accretion rate (Elitzur et al. 2014). This dependency is sometimes used as the reason for the appearance/disappearance of the BLR with changes in luminosity in the CLQs (e.g., LaMassa et al. 2015). On the other hand, the dust torus origin model assumes that BLR is continuously connected with the dust torus, where the ionized component becomes the BLR during mass accretion to the accretion disk.

We believe that the results of this study can be used to validate the model of the origin of the BLR observationally. First, assuming that disk winds from the accretion disk are the origin of the BLR, strong outflow is expected. Features of outflow are detectable by velocity-resolved RM, which predicts that the red side of the broad line follows the blue side. In other words, the disk wind model is not dominant if the velocity-resolved RM does not detect outflow. The independent variation of the broad line from the continuum variation also excludes the disk wind model, because these two should be correlated in this model. We will now discuss the origin of the Region X/Y in terms of two aspects: velocity-resolved RM and response to continuum variation, respectively.

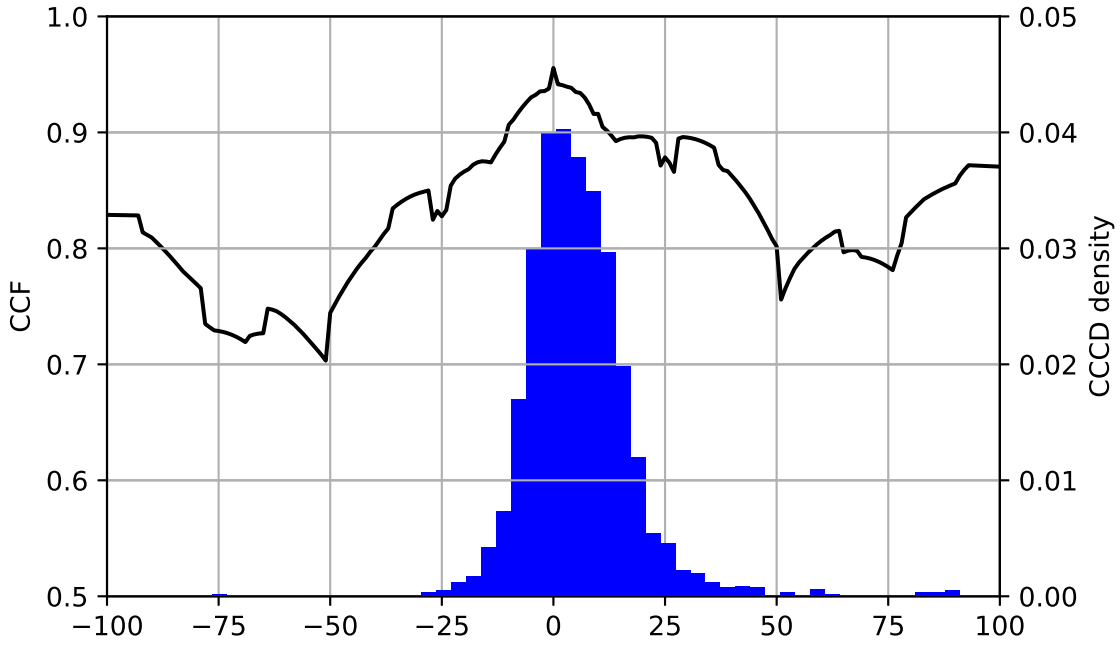

Figure 4.10: ICCF of blue wings relative to red wings of Hβ, and the distribution of ICCF center.

To confirm the origin of Region X, we conducted a simple velocity-resolved RM. We calculated the cross-correlation function for each of the light curves of the red wing (4701.3-4861.3 Å) and the blue wing (4861.3-5021.3 Å) components of Hβ. As a result, the measured time-lag is $-0.8^{+241.1}_{-213.6}$ days, which means any dominant time-lag was not detected (Figure 4.10). There are five CCF peaks in Figure 4.10, but they are symmetrically distributed, indicating that this is the effect of random errors being placed on each measurement point. If the gas in Region X was come from disk winds, the outflow reach ~ 0.4 pc in 20 years, which means the velocity is about 1% of the light speed. When there is strong outflow, the red wing should lag behind the blue wing, because the part far from the observer is moving away (Gaskell 2009). Here, it is unlikely that gas in Region X was supplied by outflow, as no significant time-lags could be measured for the red and blue wings. In addition, the evidence of strong inflow was not observed either, suggesting that gas in Region X doesn't have significant radial motion.

Because no significant radial motion was detected in Region X, we believe that the gas existed near the torus before being ionized by the increase in central luminosity. The radius of the ionizing region is thought to be proportional to the

central luminosity to the power of 1/2; the BLR's "breathing" phenomena have been reported for several objects (e.g.,). The dust sublimation radius measured by the time-lag of $W1$ is about twice the radius of Region X. The time-lag of $W1$ is mainly dominated by the time-lag when J1258 turns to dim, which may reflect the sublimation radius after it brightens. It is plausible to assume that the dust sublimation radius increased by a factor of 2 during the RM observation period since the continuum luminosity increased 4-5 times during the observation period. Therefore, we conclude that the origin of the gas in Region X can be said to be the torus, which appeared passively with the luminosity variation.

Region Y is unlikely to have been formed by outflow, as it is not affected by variation in central luminosity. The asymmetric double-peak component suggests that the gas distribution is biased, formed within a relatively short timescale (¡ gas circling timescale: 200 years). We believe that the dust clumps have been tidally disrupted to create an inhomogeneous gas distribution over a short period (Wang et al. 2017). In other words, Region Y was formed independent of the state of the accretion disk and thus is less affected by the state transitions.

In summary, the BLR gas in J1258 has two very different positional regions, both of which are likely sourced from the dust torus. Although both originate from the dust torus, we conclude that they have different mechanisms of origin. One is that a large variation due to state transition changes the radius of being ionized to extend the BLR (Region X). The other is the ionization of components that enter inside the sublimation radius due to mass accretion naturally from the dust torus (Region Y).

4.5 Conclusions

In this research, we conducted optical and mid-IR RM and X-ray follow-up observation of an extremely variable CSQ; J1258. This is the first result of RM of the most extremely variable quasar. Our conclusions are as follows.

- The brightening event can be explained by the state transition of the accretion disk, similar to X-ray binaries.
- Black hole mass of J1258 is $10^{9.46^{+0.15}_{-0.19}}\mathrm{M}_{\odot}$.
- The location of the BLR near the central core is inferred from the RM results (Figure 4.9). There are two components in the broad line region, each located at 0.25 pc and 0.37 pc from the center. The radius of the dust torus is 0.7 pc.

- The other one is likely to be accretion from dust torus. Another origin is likely to be the sublimation of dust torus.

4.6 Appendix for chapter 4

In Figure 4.11, we show all spectra used in this study. In Table 4.6, we summarize the information of each spectrum and the result of spectral fitting. In Figure 4.13, we show the estimated light curves produced by JAVELIN.

Observation Date MJD (MM-DD-YYYY)	Instrument	Exposure Time second × number	Standard Star	L5100 10^{17} erg/s/Å	Hβ 10^{17} erg/s
53848 (04-23-2006)	SDSS	3000 × 3	-	15.2 ± 0.1	36.0 ± 7.2
57481 (04-03-2016)	SDSS	3600 × 4	-	65.9 ± 0.1	96.2 ± 12.9
57846 (04-03-2017)	LAMOST	5400 × 3	-	55.3 ± 0.1	99.3 ± 10.5
58470 (12-18-2018)	MALLS	1200 × 5	HZ44	42.1 ± 0.5	54.4 ± 29.5
58606 (05-03-2019)	MALLS	1200 × 5	BD+33d2642	48.6 ± 0.2	59.5 ± 12.8
58607 (05-04-2019)	MALLS	1200 × 4	BD+33d2642	45.7 ± 0.4	57.3 ± 19.2
58612 (05-09-2019)	MALLS	1200 × 4	HZ44	47.3 ± 0.3	60.1 ± 15.9
58899 (02-20-2020)	KOOLS-IFU	600 × 10	HZ44	51.2 ± 0.2	62.1 ± 11.2
58913 (03-05-2020)	KOOLS-IFU	600 × 6	HZ44	48.8 ± 0.3	49.9 ± 17.5
58927 (03-19-2020)	KOOLS-IFU	600 × 8	HZ44	60.9 ± 0.2	64.7 ± 11.5
58940 (04-01-2020)	KOOLS-IFU	600 × 8	HZ44	62.6 ± 0.3	67.4 ± 18.0
58953 (04-14-2020)	KOOLS-IFU	600 × 8	HZ44	70.1 ± 0.1	70.1 ± 8.4
58963 (04-24-2020)	KOOLS-IFU	600 × 7	HZ44	71.7 ± 0.2	72.9 ± 12.5
58964 (04-25-2020)	KOOLS-IFU	600 × 6	HZ44	79.9 ± 0.2	81.5 ± 14.9
58967 (04-28-2020)	KOOLS-IFU	600 × 8	HZ44	71.6 ± 0.2	78.0 ± 10.5
58982 (05-13-2020)	KOOLS-IFU	600 × 8	HZ44	71.2 ± 0.2	80.3 ± 13.4
58989 (05-20-2020)	KOOLS-IFU	600 × 4	HZ44	74.8 ± 0.3	75.5 ± 17.2
58991 (05-22-2020)	KOOLS-IFU	600 × 7	HZ44	76.6 ± 0.2	71.0 ± 11.9

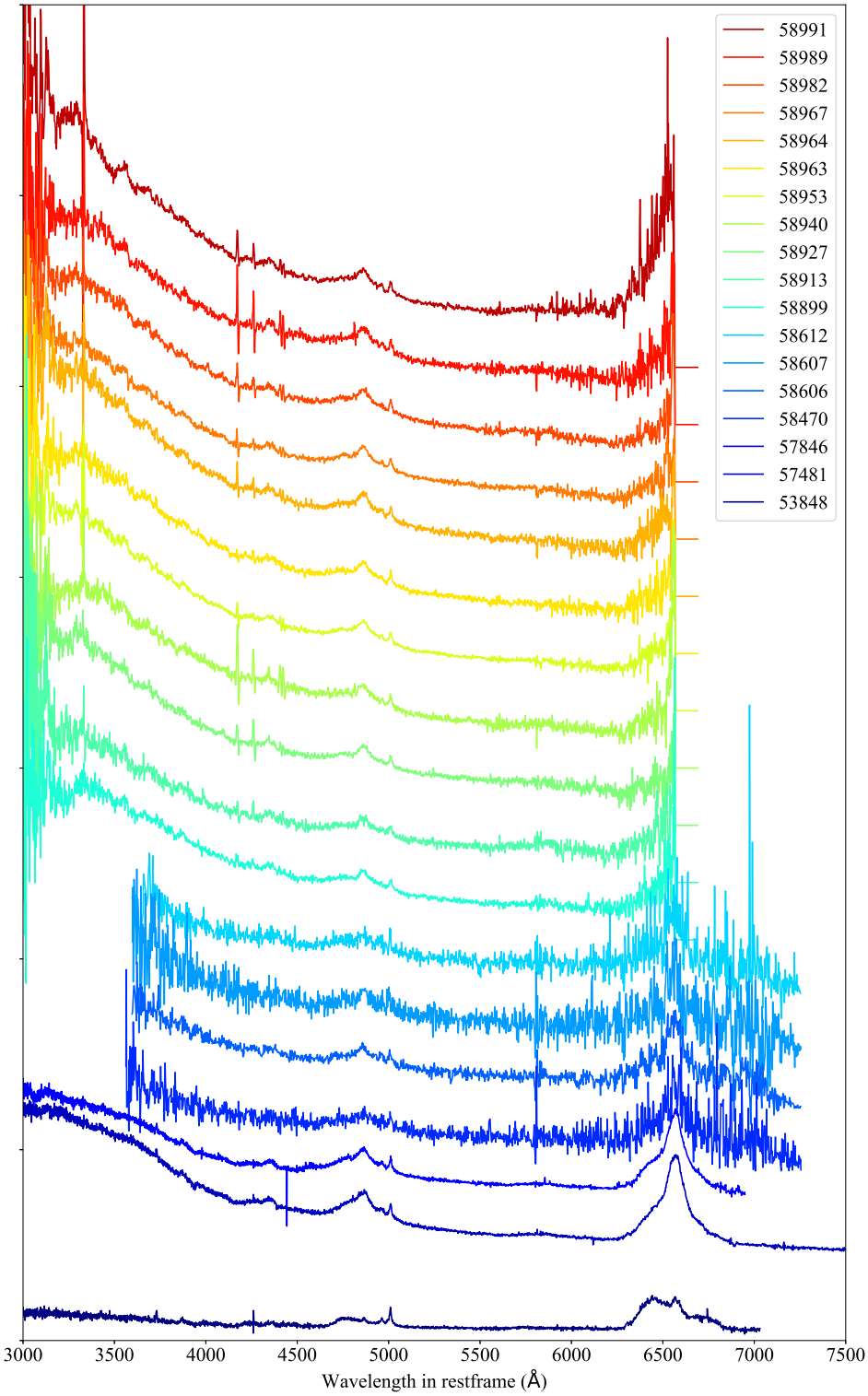

Figure 4.11: All spectra we used in this analysis. Color corresponds to the observation date in MJD. Each spectrum has been added offset for better visibility.

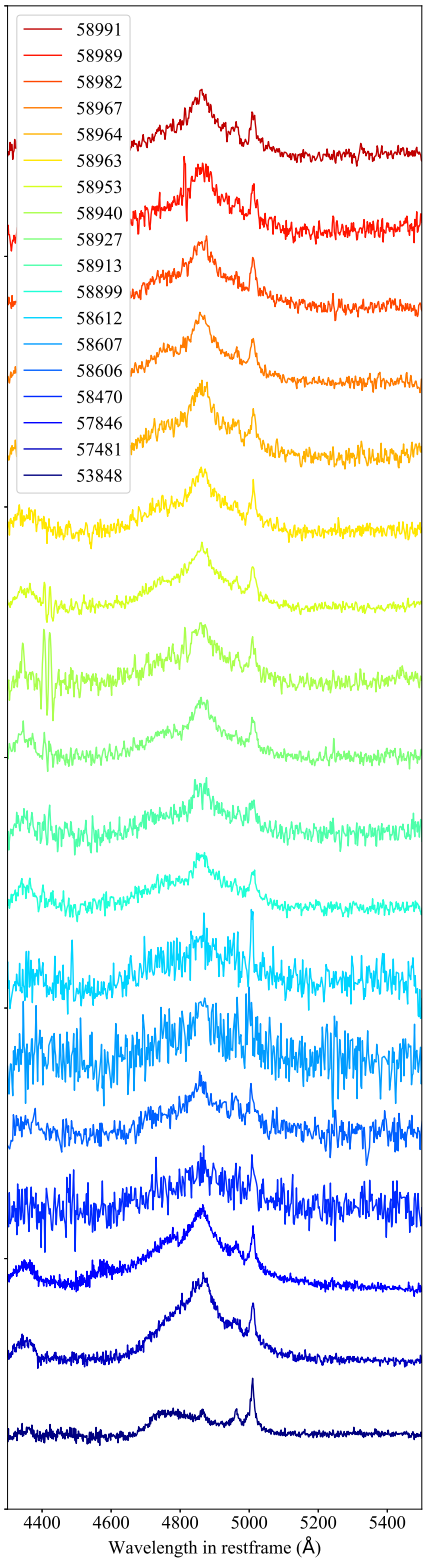

Figure 4.12: All spectra subtracted continuum. Color corresponds to the observation date in MJD. Each spectrum has been added offset for better visibility.

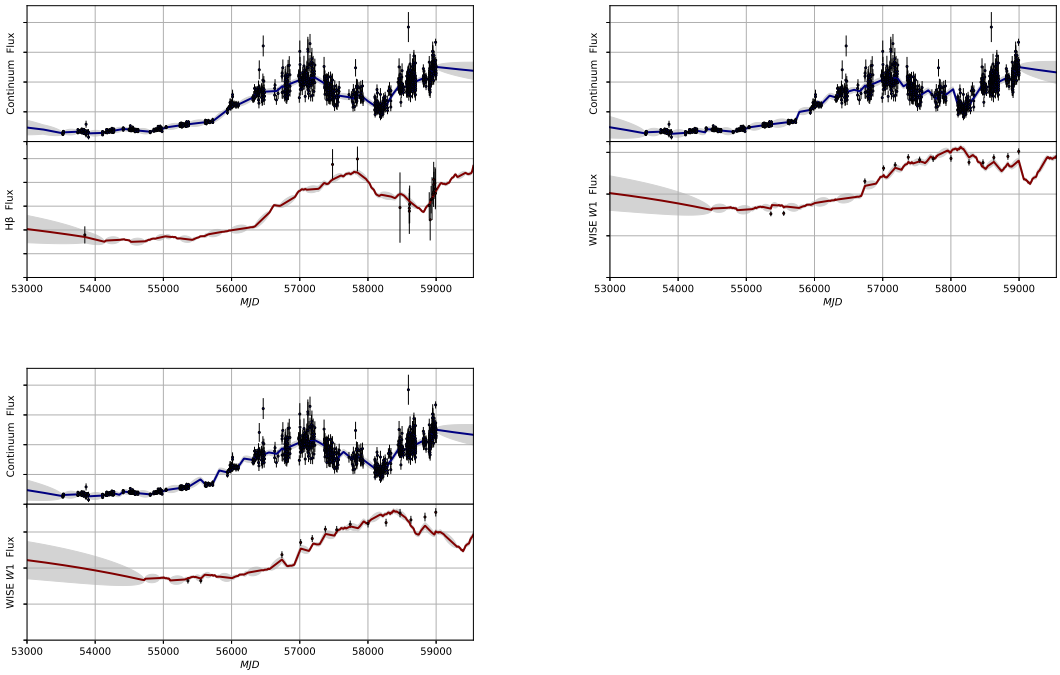

Figure 4.13: The light curves of continuum (top), Hβ (the second), WISE $W1$ (the third), and WISE $W2$ (bottom) of J1258.

Chapter 5

Conclusions

5.1 Summery

The author conducted research on the variability of quasars, resulting in three publications. This section describes the main points of the author's work.

Paper 1: Discovery of a new extreme changing-state quasar with 4 mag variation, SDSS J125809.31+351943.0

- We discovered an extreme variation in a quasar, SDSS J125809.31+351943.0 (J1258), which brightened in optical for 4 mag over approximately 30 years, which is one of the largest quasar brightening events so far.
- We argue that the variability of J1258, particularly its brightening event, can be explained by the propagation of a heating front and transitions in the accretion disk state based on variations in the timescale and Eddington ratio.

Paper 2: The relation between quasars' optical spectra and variability

- We visualized the relationship between the position on this Eigenvector 1 (EV1) plane and how they had changed their brightness after $\sim$ 10 years.
- We discovered that there is a correlation between quasars' optical variability and their distribution on the EV1 plane. Significantly dimming objects tend to transit across the distribution ridge from lower-left to upper-right, while brightening objects tend to do the opposite.

- We discovered that $R_{\rm FeII}$ is anti-correlated with the Eddington ratio when focusing on individual quasars.
- We suggest that reported CSQs are expected to repeat state transition.

Paper 3: Probing the origin of broad line region by reverberation mapping and multi-wavelength observations of an extremely variable quasar

- We performed reverberation mapping with optical spectroscopy to investigate the structure of the broad line region and to measure the black hole mass.
- The results of the reverberation mapping show that the Eddington ratio crossed the value of 0.01 before and after state transition for the constant black hole mass of $10^{9.46^{+0.15}_{-0.19}}{\rm M}_{\odot}$.
- The variations in $\alpha_{\rm ox}$ and the Eddington ratio were consistent with those predicted from the instability of the accretion disk caused by hydrogen ionization.
- From the viewpoint of the broad line region, we confirmed the existence of two distinct rotating/inflowing components located near the dust torus.
- We suggest that these components originate from rotating/inflowimg gases located near the dust torus generated by different processes.

5.2 Future Prospects

This study demonstrates that the variations of CSQs can provide insights into the origin of gas in the BLR. However, it is currently unclear to what extent the BLR components are distributed in typical quasars. It is also premature to generalize these findings to all quasars, as J1258 may be a unique object. To confirm whether the two BLR components observed in J1258 are typical of quasars, it will be important to construct a kinematic model of the BLR for each object.

List of Figures

List of Tables

References

Abazajian, K. N., Adelman-McCarthy, J. K., Agüeros, M. A., et al. 2009, ApJS, 182, 543

Agol, E., & Krolik, J. H. 2000, ApJ, 528, 161

Ahumada, R., Prieto, C. A., Almeida, A., et al. 2020, ApJS, 249, 3

Alam, S., Albareti, F. D., Allende Prieto, C., et al. 2015, ApJS, 219, 12

Antonucci, R. 1993, ARA&A, 31, 473

Arnaud, K. A. 1996, in Astronomical Society of the Pacific Conference Series, Vol. 101, Astronomical Data Analysis Software and Systems V, ed. G. H. Jacoby & J. Barnes, 17

Bao, D.-W., Brotherton, M. S., Du, P., et al. 2022, ApJS, 262, 14

Barth, A. J., Pancoast, A., Bennert, V. N., et al. 2013, ApJ, 769, 128

Becker, R. H., White, R. L., & Helfand, D. J. 1995, ApJ, 450, 559

Boroson, T. A., & Green, R. F. 1992, ApJS, 80, 109

Brotherton, M. S., Du, P., Xiao, M., et al. 2020, ApJ, 905, 77

Bruce, A., Lawrence, A., MacLeod, C., et al. 2017, MNRAS, 467, 1259

Burrows, D. N., Hill, J. E., Nousek, J. A., et al. 2005, Space Sci. Rev., 120, 165

Cackett, E. M., Bentz, M. C., & Kara, E. 2021, iScience, 24, 102557

Caplar, N., Pena, T., Johnson, S. D., & Greene, J. E. 2020, ApJ, 889, L29

Cash, W. 1979, ApJ, 228, 939

Chambers, K. C., Magnier, E. A., Metcalfe, N., et al. 2016, arXiv e-prints, arXiv:1612.05560

Clavel, J., Wamsteker, W., & Glass, I. S. 1989, ApJ, 337, 236

Cohen, R. D., Rudy, R. J., Puetter, R. C., Ake, T. B., & Foltz, C. B. 1986, ApJ, 311, 135

Cui, X.-Q., Zhao, Y.-H., Chu, Y.-Q., et al. 2012, Research in Astronomy and Astrophysics, 12, 1197

Czerny, B., & Hryniewicz, K. 2011, A&A, 525, L8

de Vries, W. H., Becker, R. H., White, R. L., & Loomis, C. 2005, AJ, 129, 615

Denney, K. D., Peterson, B. M., Pogge, R. W., et al. 2010, ApJ, 721, 715

Dexter, J., Xin, S., Shen, Y., et al. 2019, ApJ, 885, 44

Drake, A. J., Djorgovski, S. G., Graham, M. J., et al. 2019, MNRAS, 482, 98

Drake, A. J., Djorgovski, S. G., Mahabal, A., et al. 2009, ApJ, 696, 870

Du, P., Lu, K.-X., Hu, C., et al. 2016, ApJ, 820, 27

Du, P., Brotherton, M. S., Wang, K., et al. 2018a, ApJ, 869, 142

Du, P., Zhang, Z.-X., Wang, K., et al. 2018b, ApJ, 856, 6

Elitzur, M. 2012, ApJ, 747, L33

Elitzur, M., Ho, L. C., & Trump, J. R. 2014, MNRAS, 438, 3340

Eracleous, M., Boroson, T. A., Halpern, J. P., & Liu, J. 2012, ApJS, 201, 23

Eracleous, M., & Halpern, J. P. 1994, ApJS, 90, 1

—. 2003, ApJ, 599, 886

Esin, A. A., McClintock, J. E., & Narayan, R. 1997, ApJ, 489, 865

Gaskell, C. M. 1982, ApJ, 263, 79

—. 1988, ApJ, 325, 114

—. 2009, 53, 140

Gaskell, C. M. 2010, in Astronomical Society of the Pacific Conference Series, Vol. 427, Accretion and Ejection in AGN: a Global View, ed. L. Maraschi, G. Ghisellini, R. Della Ceca, & F. Tavecchio, 68

Gaskell, C. M., & Goosmann, R. W. 2013, ApJ, 769, 30

Gaskell, M., Thakur, N., Tian, B., & Saravanan, A. 2022, Astronomische Nachrichten, 343, e210112

Gezari, S., Hung, T., Cenko, S. B., et al. 2017, ApJ, 835, 144

Graham, M. J., Ross, N. P., Stern, D., et al. 2020, MNRAS, 491, 4925

Green, P. J., Pulgarin-Duque, L., Anderson, S. F., et al. 2022, ApJ, 933, 180

Grier, C. J., Martini, P., Watson, L. C., et al. 2013a, ApJ, 773, 90

Grier, C. J., Peterson, B. M., Horne, K., et al. 2013b, ApJ, 764, 47

Gunn, J. E., Siegmund, W. A., Mannery, E. J., et al. 2006, AJ, 131, 2332

Guo, H., Shen, Y., & Wang, S. 2018, PyQSOFit: Python code to fit the spectrum of quasars, Astrophysics Source Code Library, record ascl:1809.008, ascl:1809.008

Guo, H., Shen, Y., He, Z., et al. 2020, ApJ, 888, 58

He, Z., Jiang, N., Wang, T., et al. 2021, ApJ, 907, L29

Hopkins, P. F., Hayward, C. C., Narayanan, D., & Hernquist, L. 2012, MNRAS, 420, 320

Hu, C., Li, S.-S., Guo, W.-J., et al. 2020, ApJ, 905, 75

Husemann, B., Urrutia, T., Tremblay, G. R., et al. 2016, A&A, 593, L9

Hutsemékers, D., Agís González, B., Marin, F., et al. 2019, A&A, 625, A54

Hutsemékers, D., Agís González, B., Sluse, D., Ramos Almeida, C., & Acosta Pulido, J. A. 2017, A&A, 604, L3

Ichikawa, K., Ueda, J., Bae, H.-J., et al. 2019, ApJ, 870, 65

Jin, X., Ruan, J. J., Haggard, D., et al. 2021, ApJ, 912, 20

Kawaguchi, T., Mineshige, S., Umemura, M., & Turner, E. L. 1998, ApJ, 504, 671

Kellermann, K. I., Sramek, R., Schmidt, M., Shaffer, D. B., & Green, R. 1989, AJ, 98, 1195

Kelly, B. C., Bechtold, J., & Siemiginowska, A. 2009, ApJ, 698, 895

King, A. R., Pringle, J. E., & Livio, M. 2007, MNRAS, 376, 1740

Kochanek, C. S., Shappee, B. J., Stanek, K. Z., et al. 2017, PASP, 129, 104502

Koratkar, A. P., & Gaskell, C. M. 1989, ApJ, 345, 637

Kurita, M., Kino, M., Iwamuro, F., et al. 2020, PASJ, 72, 48

LaMassa, S. M., Cales, S., Moran, E. C., et al. 2015, ApJ, 800, 144

Li, S.-S., Yang, S., Yang, Z.-X., et al. 2021, ApJ, 920, 9

Li, S.-S., Feng, H.-C., Liu, H. T., et al. 2022, ApJ, 936, 75

Lin, D. N. C., & Shields, G. A. 1986, ApJ, 305, 28

Liu, X., Shen, Y., Bian, F., Loeb, A., & Tremaine, S. 2014, ApJ, 789, 140

LSST Science Collaboration, Abell, P. A., Allison, J., et al. 2009, arXiv e-prints, arXiv:0912.0201

Lu, K.-X., Bai, J.-M., Zhang, Z.-X., et al. 2019, ApJ, 887, 135

Lu, K.-X., Wang, J.-G., Zhang, Z.-X., et al. 2021, ApJ, 918, 50

Luo, A. L., Zhao, Y.-H., Zhao, G., et al. 2015, Research in Astronomy and Astrophysics, 15, 1095

Lusso, E., Comastri, A., Vignali, C., et al. 2010, A&A, 512, A34

MacLeod, C. L., Ivezić, Ž., Kochanek, C. S., et al. 2010, ApJ, 721, 1014

MacLeod, C. L., Ross, N. P., Lawrence, A., et al. 2016, MNRAS, 457, 389

MacLeod, C. L., Green, P. J., Anderson, S. F., et al. 2019, ApJ, 874, 8

Magorrian, J., Tremaine, S., Richstone, D., et al. 1998, AJ, 115, 2285

Mainzer, A., Bauer, J., Cutri, R. M., et al. 2014, ApJ, 792, 30

Marziani, P., Dultzin, D., Sulentic, J. W., et al. 2018, Frontiers in Astronomy and Space Sciences, 5, 6

Mathur, S., Denney, K. D., Gupta, A., et al. 2018, ApJ, 866, 123

Matsubayashi, K., Ohta, K., Iwamuro, F., et al. 2019, PASJ, 71, 102

Matthews, T. A., & Sandage, A. R. 1963, ApJ, 138, 30

Merloni, A., Dwelly, T., Salvato, M., et al. 2015, MNRAS, 452, 69

Mishra, H. D., Dai, X., Chen, P., et al. 2021, ApJ, 913, 146

Nagoshi, S., & Iwamuro, F. 2022, PASJ, 74, 1198

Nagoshi, S., Iwamuro, F., Wada, K., & Saito, T. 2021, PASJ, 73, 122

Namekata, D., & Umemura, M. 2016, MNRAS, 460, 980

Narayan, R., & Yi, I. 1994, ApJ, 428, L13

Netzer, H. 2019, MNRAS, 488, 5185

Nicastro, F. 2000, ApJ, 530, L65

Nicastro, F., Martocchia, A., & Matt, G. 2003, ApJ, 589, L13

Noda, H., & Done, C. 2018, MNRAS, 480, 3898

Nyland, K., Dong, D. Z., Patil, P., et al. 2020, ApJ, 905, 74

Osaki, Y. 1996, PASP, 108, 39

Pancoast, A., Brewer, B. J., Treu, T., et al. 2014, MNRAS, 445, 3073

Perivolaropoulos, L., & Skara, F. 2022, 95, 101659

Peterson, B. M. 1997, An Introduction to Active Galactic Nuclei

—. 1998, Advances in Space Research, 21, 57

Peterson, B. M., Ferrarese, L., Gilbert, K. M., et al. 2004, ApJ, 613, 682

Planck Collaboration, Aghanim, N., Akrami, Y., et al. 2020, A&A, 641, A6

Ricci, C., & Trakhtenbrot, B. 2022, arXiv e-prints, arXiv:2211.05132

Ricci, C., Trakhtenbrot, B., Koss, M. J., et al. 2017, ApJS, 233, 17

Riess, A. G., Yuan, W., Macri, L. M., et al. 2022, ApJ, 934, L7

Risaliti, G., Miniutti, G., Elvis, M., et al. 2009, ApJ, 696, 160

Ross, N. P., Graham, M. J., Calderone, G., et al. 2020, MNRAS, 498, 2339

Ross, N. P., Ford, K. E. S., Graham, M., et al. 2018, MNRAS, 480, 4468

Ruan, J. J., Anderson, S. F., Cales, S. L., et al. 2016, ApJ, 826, 188

Rumbaugh, N., Shen, Y., Morganson, E., et al. 2018, VizieR Online Data Catalog, J/ApJ/854/160

Runnoe, J. C., Eracleous, M., Mathes, G., et al. 2015, ApJS, 221, 7

Sarkar, A., Ferland, G. J., Chatzikos, M., et al. 2021, ApJ, 907, 12

Schneider, D. P., Richards, G. T., Hall, P. B., et al. 2010, AJ, 139, 2360

Shakura, N. I., & Sunyaev, R. A. 1973, A&A, 24, 337

Shapiro, S. L., Lightman, A. P., & Eardley, D. M. 1976, ApJ, 204, 187

Shappee, B. J., Prieto, J. L., Grupe, D., et al. 2014, ApJ, 788, 48

Shen, Y., & Ho, L. C. 2014, Nature, 513, 210

Shen, Y., Richards, G. T., Strauss, M. A., et al. 2011, ApJS, 194, 45

Sheng, Z., Wang, T., Jiang, N., et al. 2020, ApJ, 889, 46

Stern, D., McKernan, B., Graham, M. J., et al. 2018, ApJ, 864, 27

Stone, Z., Shen, Y., Burke, C. J., et al. 2022, MNRAS, 514, 164

Storchi-Bergmann, T., Eracleous, M., Livio, M., et al. 1995, ApJ, 443, 617

Sulentic, J. W., Zwitter, T., Marziani, P., & Dultzin-Hacyan, D. 2000, ApJ, 536, L5

Sun, M., Grier, C. J., & Peterson, B. M. 2018, PyCCF: Python Cross Correlation Function for reverberation mapping studies, Astrophysics Source Code Library, record ascl:1805.032, ascl:1805.032

Tachibana, Y., Graham, M. J., Kawai, N., et al. 2020, ApJ, 903, 54

Takeuchi, M., Mineshige, S., & Negoro, H. 1995, PASJ, 47, 617

Tananbaum, H., Avni, Y., Branduardi, G., et al. 1979, ApJ, 234, L9

Tohline, J. E., & Osterbrock, D. E. 1976, ApJ, 210, L117

Tonry, J. L., Stubbs, C. W., Lykke, K. R., et al. 2012, ApJ, 750, 99

Trakhtenbrot, B., Arcavi, I., MacLeod, C. L., et al. 2019, ApJ, 883, 94

Truemper, J. 1982, Advances in Space Research, 2, 241

Ueda, Y., Akiyama, M., Hasinger, G., Miyaji, T., & Watson, M. G. 2014, ApJ, 786, 104

Urry, C. M., & Padovani, P. 1995, PASP, 107, 803

van Velzen, S., Holoien, T. W. S., Onori, F., Hung, T., & Arcavi, I. 2020, Space Sci. Rev., 216, 124

Vestergaard, M., & Peterson, B. M. 2006, ApJ, 641, 689

Voges, W., Aschenbach, B., Boller, T., et al. 1999, A&A, 349, 389

Wada, K., Iwamuro, F., Nagoshi, S., & Saito, T. 2021, PASJ, 73, 596

Wang, J., Xu, D. W., & Wei, J. Y. 2018, ApJ, 858, 49

Wang, J.-M., & Bon, E. 2020, A&A, 643, L9

Wang, J.-M., Du, P., Brotherton, M. S., et al. 2017, Nature Astronomy, 1, 775

Wang, J.-M., Songsheng, Y.-Y., Li, Y.-R., Du, P., & Zhang, Z.-X. 2020, Nature Astronomy, 4, 517

Weedman, D. W. 1985, ApJS, 57, 523

Wilhite, B. C., Brunner, R. J., Grier, C. J., Schneider, D. P., & vanden Berk, D. E. 2008, MNRAS, 383, 1232

Willingale, R., Starling, R. L. C., Beardmore, A. P., Tanvir, N. R., & O'Brien, P. T. 2013, MNRAS, 431, 394

Wright, E. L., Eisenhardt, P. R. M., Mainzer, A. K., et al. 2010, AJ, 140, 1868

Yang, Q., Wu, X.-B., Fan, X., et al. 2018, ApJ, 862, 109

York, D. G., Adelman, J., Anderson, John E., J., et al. 2000, AJ, 120, 1579

Zhang, Z.-X., Du, P., Smith, P. S., et al. 2019, ApJ, 876, 49

Zhao, G., Zhao, Y.-H., Chu, Y.-Q., Jing, Y.-P., & Deng, L.-C. 2012, Research in Astronomy and Astrophysics, 12, 723

Zu, Y., Kochanek, C. S., & Peterson, B. M. 2010, JAVELIN: Just Another Vehicle for Estimating Lags In Nuclei, Astrophysics Source Code Library, record ascl:1010.007, ascl:1010.007

—. 2011, ApJ, 735, 80

Zu, Y., & Weinberg, D. H. 2013, MNRAS, 431, 3319